Reliable Indoor Optical Wireless Communication in the Presence of Fixed and Random Blockers

Nurul Aini Amran

Doctor of Philosophy

The University of Edinburgh

2023

Abstract

The advanced innovation of smartphones has led to the exponential growth of internet users which is expected to reach 71% of the global population by the end of 2027 [1]. This in turn has given rise to the demand for wireless data and internet devices that is capable of providing energy-efficient, reliable data transmission and high-speed wireless data services. Light-fidelity (LiFi), known as one of the optical wireless communication (OWC) technology is envisioned as a promising solution to accommodate these demands. However, the indoor LiFi channel is highly environment-dependent which can be influenced by several crucial factors (e.g., presence of people, furniture, random users' device orientation and the limited field of view (FOV) of optical receivers) which may contribute to the blockage of the line-of-sight (LOS) link.

In this thesis, it is investigated whether deep learning (DL) techniques can effectively learn the distinct features of the indoor LiFi environment in order to provide superior performance compared to the conventional channel estimation techniques (e.g., minimum mean square error (MMSE) and least squares (LS)). This performance can be seen particularly when access to real-time channel state information (CSI) is restricted and is achieved with the cost of collecting large and meaningful data to train the DL neural networks and the training time which was conducted offline. Two DL-based schemes are designed for signal detection and resource allocation where it is shown that the proposed methods were able to offer close performance to the optimal conventional schemes and demonstrate substantial gain in terms of bit-error ratio (BER) and throughput especially in a more realistic or complex indoor environment.

Performance analysis of LiFi networks under the influence of fixed and random blockers is essential and efficient solutions capable of diminishing the blockage effect is required. In this thesis, a CSI acquisition technique for a reconfigurable intelligent surface (RIS)-aided LiFi network is proposed to significantly reduce the dimension of the decision variables required for RIS beamforming. Furthermore, it is shown that several RIS attributes such as shape, size, height and distribution play important roles in increasing the network performance. Finally, the performance analysis for an RIS-aided realistic indoor LiFi network are presented. The proposed RIS configuration shows outstanding performances in reducing the network outage probability under the effect of blockages, random device orientation, limited receiver's FOV, furniture and user behavior.

Establishing a LOS link that achieves uninterrupted wireless connectivity in a realistic indoor environment can be challenging. In this thesis, an analysis of link blockage is presented for an indoor LiFi system considering fixed and random blockers. In particular, novel analytical framework of the LOS coverage probability for a single source and multi-source are derived. Using the proposed analytical framework, link blockages of the indoor LiFi network are carefully investigated and it is shown that the incorporation of multiple sources and RIS can significantly reduce the LOS coverage probability in indoor LiFi systems.

Lay summary

In order to address the rapid growth in demand for wireless data, many studies and research have been carried out. Among the rising technologies introduced over the years, light-fidelity (LiFi) has gained attention and is considered as a promising solution to accommodate these demands. This novel technology typically uses light emitting diodes (LEDs) for illumination as well as to transmit data by rapidly switching it on and off, which is undetectable by the human eye. LiFi offers a number of attractive benefits in comparison to the radio frequency networks which has made it favourable for recent and future research. The possible challenges of realizing the full potential of LiFi systems are random device orientation, link blockage, the complexity of the indoor environment and the behaviour of the user, which are studied in this thesis.

Having accurate knowledge of the LiFi channel is necessary in order to optimize the performance of LiFi systems. However in practice, it is difficult to obtain these information even by employing conventional channel estimation techniques due to the dynamic nature of the LiFi channel. Recently, machine learning schemes, particularly deep learning (DL), can be used as an alternative approach to model a realistic LiFi channel by learning the specific underlying geometry of the indoor environment. It can be envisioned that DL proposes a very promising solution to address the various channel characteristics and therefore can be applied in LiFi systems. Thus, two learning-based schemes are designed for signal detection and resource allocation for LiFi communication which provides superior performance even in the absence of full channel knowledge.

Recently, reconfigurable intelligent surfaces (RIS) have emerged as one of the most effective solutions for providing alternative line-of-sight (LOS) paths when there exists an obstacle between the transmitter and receiver by reconfiguring the wireless propagation channel. Due to the interesting properties of RIS, we incorporate RIS into the realistic indoor LiFi system and investigate the different designs of RIS that can best alleviate the joint blockage effect caused by the optical receiver's limited field of view (FOV), device random orientation, self-body blockage and blockage by other external blockers. Performance analysis of LiFi networks under the influence of fixed and random blockers is then provided and efficient solutions capable of diminishing the blockage effect is proposed in order to support seamless network connectivity.

Important factors that can affect the overall performance of LiFi networks are random device orientation and link blockage which need to be carefully analysed. Another important issue is the limited FOV of optical receivers. Thus, the impact of blockages in an RIS-assisted indoor LiFi communication system is investigated by taking into account the joint effect of optical receiver's limited FOV, user body blockage, and UE random orientation.

Declaration of originality

I hereby declare that the research recorded in this thesis and the thesis itself have been composed solely by myself and that it has not been submitted, either in whole or in part, in any previous application for a degree. Except where otherwise acknowledged, the work presented is entirely my own.

Nurul Aini Amran
Edinburgh, UK
2023

Acknowledgements

First and foremost, I would like to express my sincere gratitude to my supervisor, Professor Majid Safari for which my PhD research would not have been possible without his constant support and guidance. He has helped me above and beyond throughout my PhD journey and I have learnt a lot from him. I am truly lucky to have someone as kind and passionate as him as my supervisor. Thank you so much for believing in me. I would also like to give my special thanks to my colleague, Dr. Mohammad Dehghani Soltani for always being there to help me in my PhD journey no matter the time and day, and my second supervisor, Dr. Mehrdad Yaghoobi for his kind support and shared knowledge. My utmost appreciation also goes to my PhD viva examiners, Professor Fary Ghassemlooy and Professor Wasiu Popoola.

I would like to convey my deepest appreciation towards my parents, Dr. Amran Joned and Hamsiah Hamid, especially for their unconditional love and for their continued support, emotionally and financially throughout my study. They have inspired me to keep on furthering my education to the highest level and to strive for academic excellence since my school days. Thank you for always motivating me and for paving the way for me to reach where I am today. Words cannot describe how thankful I am to both of you. My sincere appreciation also goes to my siblings, Dr. Iskandar Mirza and Faridah Hanum, for their love and unwavering support, without limitations, throughout my PhD.

My sincere thanks also go to my best friend, Fitri Atika for her never-ending emotional support and for constantly filling my life with lots and lots of laughter. I would also like to thank my friends from the University of Edinburgh, especially my colleagues at the Institute for Imaging, Data and Communications, who have helped and encouraged me during my time here in Edinburgh. I truly appreciate your friendship and I will never forget our memorable times together.

Finally, I would like to express my deepest appreciation to the Public Service Department of Malaysia, for providing me with a full sponsorship to support my doctoral research. Without this sponsorship, I would not have been able to further my studies at the University of Edinburgh in the first place.

Contents

List of figures

List of tables

Acronyms and abbreviations

ACO-OFDM	asymmetrically clipped optical orthogonal frequency division multiplexing
ADAM	adaptive moment estimation
ADC	analog to digital converter
ADR	angle diversity receiver
ADT	angle diversity transmitter
ANN	artificial neural network
AP	access point
AWGN	additive white Gaussian noise
BER	bit-error rate
CE	channel estimation
CIR	channel impulse response
CMA	constant modulus algorithm
CNN	convolutional neural network
CP	cyclic prefix
CPU	central processing unit
CSI	channel state information
DAC	digital to analog converter
DC	direct current
DCO-OFDM	direct-current optical orthogonal frequency division multiplexing
DFNN	deep feedforward neural network
DL	deep learning
DNN	deep neural network
DSP	digital signal processor
E/O	electrical-to-optical
FEC	forward error correction
FFT	fast Fourier transform
FI	fairness index

FNN	feedforward neural network
FOV	field of view
FPGA	field programmable gate array
GRU	gated recurrent unit
HCPP	hard-core point process
IFFT	inverse fast Fourier transform
i.i.d.	independent and identically distributed
IM/DD	intensity modulation/direct detection
IR	infrared
ISI	inter-symbol interference
LD	laser diode
LED	light emitting diode
LiFi	light-fidelity
LOS	line-of-sight
LS	least squares
LSTM	long short-term memory
LTE	long-term evolution
MCM	multiple carrier modulation
ML	maximum likelihood
MLP	multi-layer perceptron
MMSE	minimum mean square error
mmWave	millimeter Wave
MSE	mean square error
NLOS	non-line-of-sight
NOMA	non-orthogonal multiple access
O/E	optical-to-electrical
OFDM	orthogonal frequency division multiplexing
OFDMA	orthogonal frequency division multiple access
O-OFDM	optical orthogonal frequency division multiplexing
OOK	on-off keying
OWC	optical wirelesss communication

PAM	pulse amplitude modulation
PD	photodiode
PDF	probability density function
PF	proportional fair
PPM	pulse position modulation
PPP	poisson point process
P/S	parallel-to-serial
PWM	pulse width modulation
QAM	quadrature amplitude modulation
QoS	quality of service
QPSK	quadrature phase shift keying
ReLU	rectified linear unit
RF	radio frequency
RGB	red-green-blue
RIS	reconfigurable intelligent surfaces
RL	reinforcement learning
RNN	recurrent neural network
RSF	reflected spot finding
SCM	single carrier modulation
SGD	stochastic gradient descent
SISO	single input-single output
SNR	signal-to-noise ratio
S/P	serial-to-parallel
THz	terahertz
TIA	transimpedance amplifier
UE	user equipment
UV	ultraviolet
VL	visible light
VLC	visible light communication
VR	virtual reality
WiFi	wireless fidelity

Nomenclature

$\otimes$	the convolution operator
$\mathrm{E}[\cdot]$	the expectation operator
$\|\cdot\|$	the Euclidean norm operator
$(.)^{\mathrm{T}}$	the transpose operator
$(\cdot)^{*}$	the complex conjugate operator
$\lfloor\cdot\rfloor$	the floor function
A	physical area of the detector
$\mathcal{A}$	set of all active sources
A_{r}	area of reflected beam spot
A_T	area of the currect target section
$b_i^{(l)}$	bias for DFNN training
B_{d}	the modulation bandwidth
c	light speed
d	the Euclidean distance between the transmitter and receiver
d_{a}	the horizontal distance between the transmitter and receiver
d_n	the total propagation distance of the nth NLOS channel
$\mathcal{E}$	event
f_0	fitted coefficient
$\tilde{f}_\theta$	probability density function of polar angle
$g(\psi)$	the optical concentrator
g_{d}	minimum receiver orientation angle
g_{u}	maximum receiver orientation angle
$\mathbf{G}_\rho$	the reflectivity matrix
h_{a}	the vertical distance between the receiver and the transmitter
h_{b}	the vertical distance between the receiver and the user height
$h(t)$	time-domain channel impulse response
$h_{\mathrm{fe}}(t)$	time-domain channel impulse response of the front-end elements

$h_{\text{ow}}(t)$	time-domain channel impulse response of the indoor OWC channel
$H(f)$	frequency-domain channel impulse response
$\mathbf{H}(f)$	the frequency-dependent transfer matrix
$H_{\text{fe}}(f)$	frequency-domain channel impulse response of the front-end elements
$H_{\text{ow}}(f)$	frequency-domain channel impulse response of the indoor OWC channel
$H_{\text{LOS}}(f)$	frequency-domain of LOS link
$\widehat{\mathbf{H}}_{\text{LS}}$	LS estimated channel gain
$\widehat{\mathbf{H}}_{\text{MMSE}}$	MMSE estimated channel gain
$H_{\text{NLOS}}(f)$	frequency-domain of NLOS link
$H^{\text{RIS}}(f)$	frequency-domain of RIS link
$\mathbf{I}$	the unity matrix
$\mathcal{K}$	total number of subcarriers
L_{a}	location of source
L_i	location of random blocker
$\hat{L}_j$	location of fixed blocker
L_{los}	LOS link vector
L_n	location of n-th RIS element
L_{u}	location of receiver
m	the Lambertian order
M	total number of RIS elements
N	division factor of the received plane
N_0	noise spectral density
N_{A}	number of active sources
$N(f)$	noise at the receiver in the frequency domain
N_{B}	number of random blockers
N_{F}	number of fixed blockers
N_{u}	number of users
$\mathbf{n}_{\text{u}}$	normal vector at the receiver
$\mathbf{n}'_{\text{u}}$	normal vector at the receiver after rotation
$\mathbf{n}_{\text{t}}$	normal vector at the transmitter
$n(t)$	noise at the receiver

$\mathrm{P}(.)$	probability
$\mathcal{P}_{\text{br}}$	blockage probability due to random blocker
$\mathcal{P}_{\text{c}}$	coverage probability
p_n	n-th pilot index
$\mathcal{P}_{\text{out}}$	outage probability
$\mathcal{P}_{\text{sit}}$	outage probability for sitting locations
$\mathcal{P}_{\text{stand}}$	outage probability for standing locations
P_{t}	transmitted optical power
$\mathbf{r}(f)$	receiver transfer vector
r_{b}	horizontal distance between receiver and user body
R	radius between user and center of the room
R_{PD}	optical to electrical responsivity
R_{d}	downlink data rate
R_{req}	requested data rate
R_{HH}	channel covariance matrix
$\bar{R}_j$	average data rate
s	resource allocation factor
$\mathbf{t}(f)$	transmitter transfer vector
$\mathcal{T}$	the current target section of the room
w_{b}	body width
w	weight coefficient
$x[n]$	output of IFFT module
$x(t)$	transmitted optical signal
$\tilde{x}(t)$	modulated signal
$x_{\text{DC}}(t)$	DC bias
$x_{\text{e}}(t)$	electrical domain signal
$\boldsymbol{X}$	an OFDM frame
X	modulated data symbols
$\mathrm{X}(p_n)$	transmitted pilot signal
$y(t)$	received electrical signal
$y_i^{(l)}$	output of lth DFNN layer after going through non-linear function

$\mathrm{y}^{(l-1)}$	output of the previous DFNN layer
$\mathrm{Y}(p_n)$	received pilot signal
z_b	radius of the blockage-free zone
$z_i^{(l)}$	output of lth DFNN layer
γ_d	signal-to-noise ratio
η	the conversion factor
θ	polar angle
θ_a	projection of angle between source and UE at the receiver plane
θ_u	angle between UE rotated normal vector and the link between AP and UE
Θ_b	azimuthal angle where the body is between the UE and AP
ρ_i	reflectance of ith reflector
ρ_n	reflectance of nth RIS reflector
$\sigma_\mathrm{ReLU}(x)$	rectified linear unit function
σ^2	noise power
ς	the refractive index
τ_0	propagation delay of LOS link
τ_n	propagation delay of nth NLOS channel
ϕ	the radiance angle with respect to the axis normal to the transmitter surface
ϕ_b	body shadowing angle
Φ_c	the receiver field of view
$\Phi_{1/2}$	the half-intensity angle
ψ	the incidence angle with respect to the axis normal to the receiver surface
ω	azimuth angle
Ω	angle of direction

Chapter 1
Introduction

1.1 Motivation

As of 2023, it was approximated that there were 5.3 billion internet users worldwide, that is two-thirds of the global population [2]. It is predicted that by 2028, this number is expected to reach 6.13 billion [5]. As demands for wireless connectivity continue to surge, one of the key challenges in radio frequency (RF) communication is the limited availability of frequency spectrum needed to support the growing number of consumer devices (as illustrated in Fig. 1.1) [6]. Thus, this has motivated both academia and industry to look for alternative solutions with energy-efficient, reliable data transmission and high-speed capabilities. These include millimeter Wave (mmWave) and optical wireless communication (OWC) which are capable of supporting the data traffic growth and next-generation high-speed wireless communication systems. OWC has emerged as a promising solution to overcome the RF spectrum crisis and has attracted growing research interest worldwide for indoor and outdoor applications.

Among the rising technologies introduced over the years to accommodate these demands, visible light communication (VLC) and light fidelity (LiFi) are considered as an important representation of the future indoor OWC systems. Note that, in this thesis, we use the terms OWC, VLC and LiFi interchangeably. LiFi is known as a novel bidirectional, high-speed and fully networked wireless communication technology [7] which typically uses light emitting diodes (LEDs) or laser diodes (LDs) combined with an optical diffuser as the optical source to provide communication and illumination at the same time, and photodiodes (PDs) as the receiver to detect the transmitted optical signal [8–10]. LiFi offers several benefits in comparison to RF technology (e.g., wireless fidelity (WiFi)), such as having an extremely large and an unregulated bandwidth, high potential data rates, high energy efficiency and enhanced security due to the nature of light that does not penetrate through opaque objects [11]. Moreover, the concept of hybrid LiFi and WiFi network was first introduced in [12] which integrates the two different technologies into a

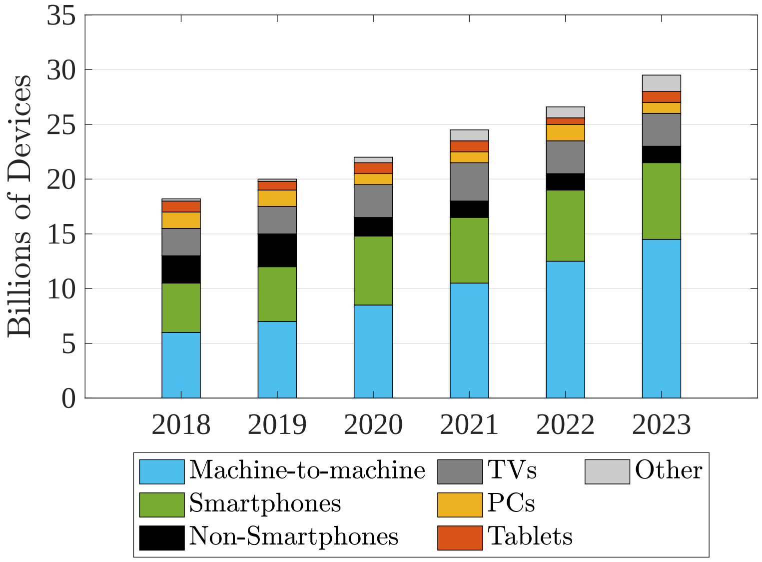

Figure 1.1: *Global device and connection growth [2].*

hybrid network and capable of providing the advantages of both LiFi and WiFi (e.g., combining the high-speed data transmission of LiFi and the ubiquitous coverage of WiFi) [13]. Some of the important differences between LiFi and WiFi can be seen in Table 1.1. To provide an example in terms of energy efficiency between LiFi and WiFi, a typical WiFi router uses $2-20$ W and consumes 1.8 kilowatt-hours (kWh) of electricity per week [14]. Meanwhile, a desk lamp with 5 W LED bulb turned on for one hour per day results in 0.07 kWh of electricity per week [15].

Although these attractive advantages of LiFi have made it very favorable for recent and future research, LiFi systems does have some limitations [4, 16] such as sensitivity to blocking by obstacles and limited transmitted power. Furthermore, LiFi are not very effective for outdoor applications and cannot provide long-distance communication. Using LiFi for the uplink also pose some issues as most modern devices do not have the transmitter for LiFi and providing new ones will increase the cost and also the device size. Using LiFi for the uplink would also results in unusual lighting conditions from a user perspective which are aesthetically not pleasing.

In order to realize the full potential of LiFi networks, many aspects of LiFi still need to be carefully studied. In fact, the LiFi channel is relatively deterministic, which allows potential improvements of the communication metrics such as the signal-to-noise ratio (SNR), bit-error

Characteristics	**WiFi**	**LiFi**
Coverage	100 m	10 m
Bandwidth	$450-600$ Mbps for 2.4 GHz, 1300 Mbps for 5 GHz	200, 000 GHz
Speed	7 Gbps	224 Gbps
Interference level	High	Low
Energy efficiency	Low	Comparatively high

Table 1.1: *Comparison between WiFi and LiFi [3, 4]*

rate (BER), user throughput, outage probability, etc. [17]. These can be done by acquiring and exploiting the channel state information (CSI) of the LiFi channel which highly depends on the nature of light and its behavior (e.g., line of sight (LOS), non-line of sight (NLOS)), link blockage, the geometry of the indoor environment (e.g., due to the positions of furniture) and the behavior of the user (e.g., random orientation of the user device and hotspots). In a practical scenario, it is important to consider these factors and conduct a more detailed analysis in order to develop effective solutions for supporting seamless connectivity of LiFi communication and networking schemes. In the following, these aspects are explained in more detail.

LiFi can only be realized as an intensity modulation/direct detection (IM/DD) system, requiring the signal to be both real-valued and non-negative [18]. This constraint restricts the application of modulation schemes developed in RF communications. Modulation techniques such as on-off keying (OOK), pulse-position modulation (PPM), pulse-width modulation (PWM), etc. can be applied straightforwardly [19, 20]. However, at higher modulation speeds, these schemes encounter inter-symbol interference (ISI) due to the non-flat frequency response of the LiFi channel [11]. Hence, more resilient techniques such as orthogonal frequency division multiplexing (OFDM) is required. OFDM enables adaptive bit and energy loading of different frequency sub-bands which leads to optimal utilization of the available resources. Furthermore, OFDM is capable of achieving throughput capacity in a non-flat communication channel even in the presence of nonlinear distortion introduced by the LED's transfer characteristics (e.g., off-the-shelf LED has a maximum 3 dB modulation bandwidth) [11]. Conventional OFDM signals are complex-valued and bipolar in nature. Thus, the standard OFDM technique used in RF has to be modified in order to become suitable for IM/DD systems. This can be done by applying Hermitian symmetry on the subcarriers in the frequency-domain to obtain a real-valued OFDM signal, and introducing a positive direct current (DC) bias to the OFDM signal to make the signal non-negative [21]. The resulting modulation scheme is known as DC-biased optical OFDM (DCO-OFDM). Another well-known solutions include asymmetrically clipped optical OFDM (ACO-OFDM), however, the disadvantage of this technique is a 50% loss in spectral efficiency [22].

For a high-speed LiFi system, having a realistic LiFi channel models is crucial for the system design. Besides the LOS component that is usually considered in most indoor environments, it is also important to consider the large number of reflections (e.g., NLOS) which results in multipath signals leading to ISI [23]. In addition, the assumption of having a perfect alignment between the user device orientation and the access point is not valid in real-life scenarios. Such an assumption is only accurate for a limited number of devices (e.g., laptops with a LiFi dongle) meanwhile the majority of users use devices such as smartphones. The device orientation affects the channel gain significantly which therefore affects the users' BER and throughput remarkably [24]. In addition, presence of the human body and furniture also introduces link blockage as well as affecting the user's location in the room (e.g., hotspots) [25]. IEEE 802.11bb [25] has endorsed reference channel models for indoor environments using ray tracing methods, for various indoor environments by considering an empty room, conference room, living room, and office space setups which has been used in several studies [26, 27]. The aforementioned factors can provide a more realistic indoor LiFi environment, however considering them would increase the complexity of the channel model.

To improve the performance of a LiFi system (e.g., signal detection and resource allocation) considering a realistic indoor environment, it is crucial to obtain an accurate knowledge of the channel by means of channel estimation. The information based on the LOS, NLOS, user behavior and furniture would provide better estimation of the quality of the wireless links. Due to the increased complexity in channel modelling for a realistic LiFi system, the majority of solutions for channel estimation in the literature for LiFi usually assume ideal or general system settings [28–31], and accurate channel estimation without the perfect channel knowledge is highly desirable. Channel estimation has been performed based on pilot assisted (e.g., least squares (LS), minimum mean square error (MMSE)) and blind estimation techniques (e.g., constant modulus algorithm (CMA)), but with certain estimation errors and suffer from the problem of convergence to local minima [32–36]. Thus, this motivates the need for deep learning (DL) as it can be used to identify patterns, distribution and trends in the data samples, and therefore can be used as an alternative approach to model a realistic channel. In contrast to the traditional approaches, DL offers a simple estimation process that can be performed indirectly in real time by viewing the channel as a black box [37]. For example, in the case of signal detection, DL neural networks can accurately identify the complex mapping relationship between the input and output signals, hence addressing the overall channel impairments efficiently in order to recover the original symbols with better BER performance [38]. Moreover, it can effectively reduce the overhead induced by pilot carriers for joint channel estimation and symbol detection/resource allocation and shows better performance compared to conventional algorithms [38]. Thus, DL is proven to be a promising tool in solving the complex communication problems with complex channel models. Over the years, DL has achieved great success in aiding different aspects of wireless communication systems, such as modulation recognition [39], indoor positioning [40], signal detection [38] and resource allocation [41]. Thus, it can be envisioned that DL proposes a very promising solution to address the various channel characteristics and therefore can be applied in LiFi systems.

Furthermore, when considering a multi-user LiFi system, resource allocation can become a vital issue as appropriate scheduling schemes are needed to ensure all of the available resource are allocated fairly to the users. It is important that these resources are allocated by considering users' behavior and the specific geometry of a room. Proportional fair (PF) scheduling has been considered as an attractive bandwidth allocation criterion in wireless networks, capable of supporting high resource utilization while maintaining a good fairness among network flows [42]. Typically, it requires full channel knowledge which is practically difficult to obtain. As the frequency response of the LiFi channel can be highly environment-dependent, it is important to seek other solutions that are capable of considering these effects to ensure priority is given to the user with poor channel condition. Note that DL has found success in solving resource allocation problems [41, 43, 44]. This gives the motivation to investigate the hypothesis that, DL-based LiFi communication techniques can effectively learn the distinct features of the indoor environment and user behavior to provide superior performance compared to the conventional channel estimation techniques particularly when access to real-time CSI is restricted.

As previously mentioned, important factors that can affect the received signal strength and the overall performance of LiFi networks such as the random device orientation and link blockage need to be carefully analysed. It is known that the LiFi channel is highly sensitive to the random orientation of user equipment (UE) which affects the overall system performance [45]. Another important issue is the limited field of view (FOV) of LiFi receivers; that is, in order to establish a connection between the transmitter and the receiver, the LOS link must fall within the FOV of the PD. However, when the UE is randomly oriented, the angle of the arrival beam may be occasionally beyond the limited FOV of the optical receiver and the UE is then blocked. Hence, the system performance can be severely disrupted. The link blockage analysis in the literature usually consider only the LOS obstruction by the human body rather than also considering the joint impact of the limited FOV of the optical receivers and it's random orientation [46–48]. To address the issue of blockages in an indoor LiFi communication system, a strategy that is able to establish alternative LOS paths is required. Recently, reconfigurable intelligent surfaces (RIS) have emerged as one of the most effective solutions for providing alternative LOS paths when there exists an obstacle between the transmitter and the receiver [49]. RIS comprises of a number of reflecting elements that work together to reconfigure the wireless propagation channel in order to enhance the communication performance. It has been shown that RIS can be successful in many different applications of the wireless communication networks [50–54]. With this in mind, it is worth to investigate the impact of blockages in an RIS-assisted indoor LiFi communication system taking into account the optical receiver's limited FOV, user body blockage, and UE random orientation.

In this research thesis and in order to fully utilize the potential of LiFi cellular networks, the aforementioned aspects and challenges are discussed and effective solutions are provided. The detailed contributions of this research thesis are presented in the next section.

1.2 Contributions

In this thesis, the performance analysis of a realistic indoor LiFi network is studied considering effects such as reflections/blockages by furniture and users, the user behaviour (e.g., the locations in the room where the users are likely to be at, and how they hold the user device). We develop deep learning based schemes for signal detection and resource allocation for OFDM

LiFi networks for such realistic indoor environments. Then, the effects of LOS optical link blockage on the outage performance of a LiFi network is studied considering different indoor scenarios and efficient RIS-based solutions, capable of diminishing the blockage effect is proposed. Finally, the analysis of link blockage are presented where an analytical framework to calculate the blockage probability of indoor LiFi systems in the presence of limited FOV of the receiver, random orientation of the user device and blockage by the user body and by other external blockers is proposed.

Following the first research objective, DL techniques are implemented to incorporate the distinct features of a realistic indoor environment in the design of LiFi systems. It is shown that DL can be very effective in learning specific characterizations of the indoor LiFi channels as well as the corresponding non-random user behavior imposed by the specific indoor environment (e.g., based on the furniture configuration, etc.), outperforming the traditional channel estimation techniques. To the best of our knowledge, this is the first time that DL-based communication schemes are investigated in the presence of a realistic LiFi channel in a typical room with furniture and different user behaviour while considering important effects such as the random orientation of the user device, blockage of LiFi links due to the existence of furniture and self-blockage by the users, and an infinity order of the NLOS channel components. Two deep learning-based schemes for signal detection and resource allocation for LiFi communication in a realistic indoor environment based on long short-term memory (LSTM) and feed forward neural networks are proposed, respectively. The neural networks are trained considering specific geometrical configurations of the indoor environment and conditional hotspot models based on varying user distributions to show the effectiveness of the learning schemes in adapting to a particular scenario compared to the benchmark conventional methods. It is noted that when partial CSI is available, these schemes are able to indirectly estimate the underlying channel characteristics and improve the performance of signal detection and user scheduling. In practical scenarios with limited instantaneous CSI, the proposed methods can perform close to the optimal performance which usually requires the presence of full channel knowledge. The contributions of this work are published in a conference paper, *2020 IEEE ICC Workshops [55]* and one journal paper in *IEEE Access [56]*.

With respect to the second research objective, the effects of LOS optical link blockage on the outage performance of a LiFi network are studied considering different indoor scenarios and efficient RIS-based solutions, capable of diminishing the blockage effect are proposed. The performance analysis take into account the crucial blocking factors such as the limited FOV of the user device, random device orientation, user's self blockage, and blockage by other blockers as well as the user's distribution. The main contributions of this work include proposing an efficient channel acquisition method for the RIS-assisted indoor OWC system which relies on the geometry of the RIS elements and the structural information of the optical channels. More specifically, the user's location is estimated based on the received signal strength in a number of steps which only logarithmically increases with the size of the room. Consequently, different subsets of RIS elements are then selected to provide beamforming towards a specific user's location. This method offers a much lower computational complexity as it significantly reduces the dimension of the decision variables required for RIS-based channel acquisition. Furthermore, several RIS attributes such as shape, size, height and distribution on the performance of a single source OWC system are investigated under the influence of blockage by the receiver's limited FOV, UE random orientation and user's self blockage. It is shown that these attributes play important roles in increasing the network performance in terms of outage probability. Numerical-based performance analysis for an RIS-aided realistic indoor LiFi network is provided for multiple source scenario and the analysis is extended by also considering blockage by other fixed and random blockers (e.g., blockage by other users and furniture). It is noted that the incorporation of furniture into the geometry of the room will also influence the user distribution (e.g., hotspot) as it increases the complexity of the system.

Finally, regarding the third research objective, the effects of LOS optical link blockage between the source and the user device considering different indoor scenarios are studied. For this purpose, analytical expressions of blockage probability which take into account, the limited FOV of the user device, random device orientation, user's self blockage, and blockage by other blockers are developed. The main contributions include proposing a novel analytical framework to calculate the blockage probability for the single source scenario considering all blockage effects induced by the limited FOV of the receiver, random orientation of the UE, user's self blockage, and other random and fixed blockers. The analytical derivations of the blockage probability is then extended to multiple source scenarios considering different source configurations. This multi-source analysis also applies to RIS-assisted LiFi systems where the RIS elements are considered as additional sources. Using the analytical model, an in-depth investigation of link blockage is provided by changing the crucial parameters such as FOV, the azimuth orientation of the user, the locations of the sources, and the positions of the UE. The accuracy of the analytical models are verified by comparing with simulation-based results and are shown to be perfectly matched. The results demonstrate the effectiveness of RIS to reduce link blockage by considering the distribution of the RIS elements with different height positions. The contributions of this work is published in one conference paper, *IEEE Global Communications Conference [57].*

The key research objectives in this thesis are outlined as follow:

- To incorporate the distinct features of a realistic indoor environment in the design of LiFi systems using DL techniques.

- To support seamless connectivity in LiFi networks by designing effective RIS-assisted indoor OWC systems and performance analysis of LiFi in the presence of fixed and random blockers.

- To derive a novel analytical framework for calculating the blockage probability considering all blockage effects induced by the limited FOV of the receiver, random orientation of the UE, user's self blockage, and other random and fixed blockers.

1.3 Thesis Layout

The rest of this thesis is organized as follows. In Chapter 2, the concept of LiFi networks and the channel model are presented. The user behavior models such as random device orientation, blockage and hotspot model are also introduced in this chapter as well as the backgrounds on deep learning and reconfigurable intelligent surface.

In Chapter 3, DL-based methods are introduced in two different problems for OFDM LiFi systems, namely, signal detection and resource allocation. The impact of a realistic LiFi channel impaired by random device orientation and blockage is simulated considering different geometrical configurations and user behavior in an indoor environment, e.g. presence or lack of furniture and varying user distribution defined by a conditional hotspot model. The performance of DL-based LiFi systems with partial CSI are compared to the optimal signal detection and resource allocation with perfect CSI and the gain is investigated in a more realistic or complex indoor environment, e.g. room with furniture or a hotspot scenario.

In Chapter 4, an efficient channel acquisition method for the RIS-assisted indoor OWC is proposed which offers a much lower computational complexity. Several RIS attributes are investigated such as shape, size, height and distribution on the performance of a single source OWC system under the influence of blockage by the receiver's limited FOV, UE random orientation and user's self blockage. A numerical-based performance analysis for an RIS-aided realistic indoor LiFi network with multiple source are provided and the analysis is extended by considering blockage by other fixed and random blockers.

A novel analytical framework to calculate the blockage probability for a single source and multi-source scenario are proposed in Chapter 5, considering all blockage effects induced by the limited FOV of the receiver, random orientation of the UE, user's self blockage, and other random and fixed blockers. Different source configurations are considered and an in-depth investigation of link blockage are investigated by changing the crucial parameters such as FOV, the azimuth orientation of the user, the locations of the sources, and the horizontal distance between the UE and the center of the room. Moreover, the effectiveness of RIS to reduce link blockage is shown by considering the distribution of the RIS elements with different height positions.

Chapter 6 summarises the key findings of this research thesis where conclusions are presented. Additionally, limitations and future work of this research topic are also discussed.

1.4 Summary

In this chapter, a brief overview of OWC and LiFi was presented and followed by the motivation based on a literature review of relevant studies related to this thesis. The contributions of this thesis are then summarised and the publications produced were mentioned. Finally, the layout of this thesis was outlined in their respective chapters.

Chapter 2
Background

2.1 Introduction

The initial historical forms of using OWC as source of communication includes signalling through smoke, beacon fires, torches and sunlight. Later, a device made with a pair of mirrors known as heliographs were used to direct beam of light which was commonly used for military communication in the late 19th century until early 20th century [58]. A historical milestone was made in the area of OWC when Alexander Graham Bell invented the photophone in 1880 that could transmit voice signals at a distance of approximately 200 meters [59]. The photophone simply relied on the vibrations on the mirror caused by the original voice at the transmitter and then reflected by sunlight and transformed back into voice at the receiver. These are some of the early means of communications through OWC. Afterwards, in modern sense, lasers and LEDs are more commonly used as light sources in the OWC systems. Early experiments involving working lasers was in 1960 where signals could be transmitted from 40 km away. However, with the development of fiber optics in the 1970's, they had become the obvious choice for long distance optical transmission and therefore has shifted the focus away from OWC systems.

In the recent years, with the ever-increasing demand for wireless applications and services, the demand for RF spectrum is overtaking the available supply and has led to the spectrum congestion. In light of the spectrum bottleneck, the focus of moving into the optical band (e.g., infrared (IR), visible light (VL) and ultraviolet (UV)) is increasing. OWC systems that operate in the visible band (390-750 nm) are commonly known as VLC. The VL spectrum is widely used in VLC and LiFi, however the main difference between LiFi and VLC is that VLC uses only the VL portion of the light spectrum, whereas LiFi uses VL in the downlink path but it is possible to use either IR, VL, or UV in the uplink path [4]. Thus, LiFi system can be treated as VLC only if VL is used as the transmission media. The application scenarios of VLC and LiFi are similar where in the indoor environment, communication and illumination are performed simultaneously.

Due to recent advancements in solid-state lighting, there has been a noticeable trend over the past decade towards replacing incandescent and fluorescent lamps with high-intensity solid-state white LEDs. These LEDs offer various advantages, including extremely high energy efficiency, longer lifespan, a compact form factor, and lower heat generation [60]. Due to these advantages, the adoption of LEDs has been steadily increasing and it is anticipated that LEDs will contribute to nearly 84% of all illumination by the year 2035 [61]. Another crucial benefit of LEDs is their capability to swiftly switch between different light intensities. This unique feature of a high switching rate presents the opportunity to employ LEDs as OWC transmitters for both high-speed communication and highly efficient lighting source simultaneously. Consequently, LEDs can serve a dual purpose by providing highly efficient illumination and facilitating very high-speed communication [4].

With the emergence of VLC and LiFi, OWC begins to show a promising market in the future. The term LiFi was first introduced in 2011 by Harald Haas during a TED Global Talk. While VLC has been considered as a point-to-point communication technique, LiFi offers a complete wireless networking system which includes bidirectional multiuser communication (i.e., point-to-multipoint and multipoint-to-point communication) and can be employed as a complementary structure along with RF networks [9]. In contrast to RF, LiFi offers a number of attractive features which have put LiFi in the scope of recent and future research, and therefore many research and development groups in both academia and industry are currently active working on the standardization and commercialization of VLC and LiFi [62–66].

2.2 LiFi System

A typical LiFi downlink transmission is shown in Fig. 2.1 where the transmitted optical signal, $x(t)$ passes through the channel with the channel impulse response (CIR), $h(t)$, and is received at the PD with the output current denoted as $y(t)$. Hence, the received signal is described as:

$$y(t) = R_{\text{PD}} h(t) \otimes x(t) + n(t), \tag{2.1}$$

where R_{PD} is the optical to electrical responsivity of the PD in A/W, $n(t)$ denotes the thermal noise at the receiver modelled as additive white Gaussian noise (AWGN), and "$\otimes$" is the con-

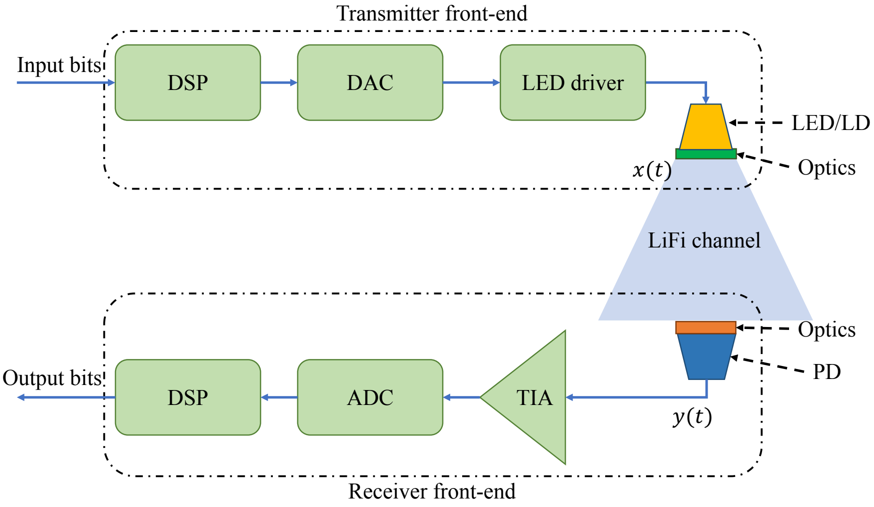

Figure 2.1: *A typical LiFi downlink transmission with commonly used front-end elements at the transmitter and receiver. Note that front-end elements encompass components such as digital signal processor (DSP), an analog to digital converter (ADC), an LED driver, a digital to analog converter (DAC) and a transimpedance amplifier (TIA).*

volution operator. $h(t)$ includes the effect of both front-end elements and the channel. The front-end elements encompass both transmitter and receiver components such as a digital signal processor (DSP), an analog to digital converter (ADC), a digital to analog converter (DAC) and a transimpedance amplifier (TIA). The channel gain can be characterized as [67]:

$$h(t) = h_{\mathrm{fe}}(t) \otimes h_{\mathrm{ow}}(t), \tag{2.2}$$

where $h_{\mathrm{fe}}(t)$ and $h_{\mathrm{ow}}(t)$ are the CIR of the front-end elements and indoor LiFi, respectively. Hence, the channel gain in the frequency domain is given as [67]:

$$H(f) = H_{\mathrm{fe}}(f)H_{\mathrm{ow}}(f), \tag{2.3}$$

where $H_{\mathrm{fe}}(f)$ and $H_{\mathrm{ow}}(f)$ are Fourier transform of $h_{\mathrm{fe}}(t)$ and $h_{\mathrm{ow}}(t)$, respectively. The CIR of the front-end elements and indoor LiFi are described in detail in the next subsections.

2.2.1 Front-end Elements

In the following, the front-end elements as shown in Fig. 2.1, can be classified as transmitter/receiver front-end elements and are discussed in more detail.

2.2.1.1 Transmitter Front-end Elements

The DSP, DAC, LED driver and LED are specifically used at the transmitter where the function of the DSP component is to convert the input information bits to digital signals. Afterwards, the DAC converts the digital signals to analogue current signals which goes into the LED driver. The LED driver operates to drive the current of the LED in which the AC signal is added onto the DC current [68]. The total current is then fed to the LED where the desired waveform is modulated onto the instantaneous power of the carrier. This process which is known as intensity modulation is considered as the most favorable and viable modulation for LiFi [18]. LEDs are commonly used as optical source in LiFi systems since white LEDs can be used to provide both illumination and communication. There are two types of commercially used white LEDs. The first type is red-green-blue (RGB) LED where it emits white optical light based on the combination of three color components generated by different set of devices [69]. The second type is a blue LED chip with a yellow-phosphor coating. The emission of narrow blue spectrum can be absorbed and efficiently re-emitted by phosphor coating. However, utilizing the second LED type has some limitations due to the fact that the absorption and re-emission time of phosphor is slow. Therefore, the 3-dB bandwidth of these LEDs is in the order of $2 - 10$ MHz [70]. Micro-LEDs have been shown to exhibit relatively large modulation bandwidths (e.g., > 100 MHz) where the improved bandwidth characteristics over conventional LEDs is due to the reduction in device self-heating and current crowding owing to their small area [71]. However, micro-LEDs have an exceptionally high manufacturing cost [72].

2.2.1.2 Receiver Front-end Elements

The receiver includes the PD, TIA, ADC and DSP. At the receiver side, the optical power is converted into electrical signals using PDs [7]. PDs are more preferable compared to other methods (e.g., imaging sensors [73, 74], solar cell panels [75] and LEDs [76]). This is due to their shorter response time which leads to a wider bandwidth and consequently providing high-speed data communication. The most practical down-conversion method in LiFi is referred to as direct detection in which a photodetector produces a current proportional to the received instantaneous power [18]. The photo-current is then converted into a voltage signal using TIA. The ADC then converts the analogue voltage signal to digital signals and it is then fed into the DSP unit for the recreation of the information bits.

2.2.1.3 Impulse Response of Front-end Elements

The combined effect of both transmitter and receiver front-end elements can be modeled as a low-pass filter as it has been shown that the front-end elements follow low-pass filter characteristics in a number of studies [70, 77, 78]. Thus, the frequency response of the front-end channel can be modeled using a first order low pass filter as [77]:

$$|H_{\mathrm{fe}}(f)|^2 = e^{-f/f_0}, \tag{2.4}$$

where f_0 denotes the LED cut-off frequency.

2.2.2 Channel of Indoor LiFi System

The LiFi channel relies upon the existence of the LOS link and the NLOS channel components. LOS is a phenomena when the link established between the access point (AP) and UE is direct and uninterrupted. Meanwhile, NLOS link relies upon the reflection of light from reflecting surfaces (e.g., walls and furniture) in the environment. The LOS link between the transmitter and the receiver is shown in Fig. 2.2-(a). The NLOS channel comprises of an infinite number of links. Fig. 2.2-(b) denotes one of the NLOS links between the transmitter and receiver. In the frequency domain, the optical channel in an indoor LiFi system can be described as [18]:

$$\begin{aligned} H_{\mathrm{ow}}(f) &= H_{\mathrm{LOS}}(f) + H_{\mathrm{NLOS}}(f) \\ &= H_{\mathrm{LOS}}(0)e^{-j2\pi f\tau_0} + \sum_{n=1}^{\infty} H_{\mathrm{NLOS},n}(0)e^{-j2\pi f\tau_n}, \end{aligned} \tag{2.5}$$

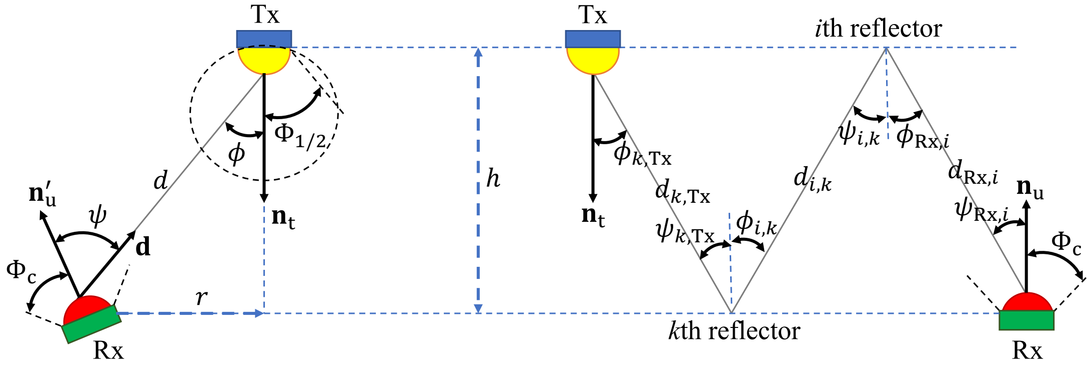

(a) LOS link (b) The nth NLOS link

Figure 2.2: *The downlink geometry of indoor LiFi channels for: (a) LOS link, and (b) NLOS links.*

where $H_{\mathrm{LOS}}(f)$ and $H_{\mathrm{NLOS}}(f)$ are the channel frequency response of the LOS and NLOS components, respectively. The DC gain of the LOS link and the nth NLOS link are denoted as $H_{\mathrm{LOS}}(0)$ and $H_{\mathrm{NLOS},n}(0)$, respectively [79]. The propagation times between the transmitter and the receiver are given as $\tau_0 = d/c$ and $\tau_n = d_n/c$ with c denoted the speed of light, d as the Euclidean distance between the transmitter and receiver, and d_n as the total propagation distance of the nth NLOS link.

The channel gain for the LOS link is expressed as [18]:

$$H_{\mathrm{LOS}}(0) = \frac{(m+1)A}{2\pi d^2} \cos^m\phi \; g_\mathrm{f} g(\psi) \cos\psi \; \mathrm{rect}\left(\frac{\psi}{\Phi_\mathrm{c}}\right), \tag{2.6}$$

where A, ϕ, ψ are the physical area of the detector, transmitter radiance angle with respect to the axis normal to the transmitter surface and receiver incidence angle with respect to the axis normal to the receiver surface, respectively. Furthermore, $\mathrm{rect}(\frac{\psi}{\Phi_\mathrm{c}}) = 1$ for $0 \le \psi \le \Phi_\mathrm{c}$ and 0 otherwise where Φ_c is the receiver FOV. The optical concentrator is given as [18]:

$$g(\psi) = \begin{cases} \dfrac{\varsigma^2}{\sin^2\Phi_\mathrm{c}}, & 0 \le \psi \le \Phi_\mathrm{c} \\ 0, & \text{otherwise} \end{cases}, \tag{2.7}$$

where ς is the refractive index. Lambertian emission order is expressed as:

$$m = -\frac{1}{\log_2(\cos\Phi_{1/2})}, \tag{2.8}$$

where $\Phi_{1/2}$ is the half-intensity angle [80]. The radiance angle ϕ and the incidence angle ψ of the transmitter and the receiver can be calculated based on the rules from analytical geometry as:

$$\begin{aligned} \cos\phi &= \frac{-\mathbf{d}\cdot\mathbf{n}_\mathrm{t}}{\|\mathbf{d}\|}, \\ \cos\psi &= \frac{\mathbf{d}\cdot\mathbf{n}'_\mathrm{u}}{\|\mathbf{d}\|} \end{aligned} \tag{2.9}$$

where $\mathbf{n}_\mathrm{t} = [0, 0, -1]^\mathrm{T}$ and $\mathbf{n}'_\mathrm{u}$ describe the normal vectors at the transmitter and the receiver planes, respectively and $\mathbf{d}$ denotes the distance vector from the receiver to the transmitter. The symbols ‘ $\cdot$ ‘ and $\|\cdot\|$ denote the inner product and the Euclidean norm operators, respectively while $(.)^\mathrm{T}$ denotes the transpose operator.

For the NLOS links, a high reflection order ensures accurate values of the diffuse channel components. The method described in [79] can be used to consider an infinite order of reflections by calculating the channel gain in the frequency domain instead of the time domain. To approach this, the environment is segmented into multiple small surface elements which act as reflectors where these surface elements are modeled as Lambertian radiators described by (2.8) with $m = 1$. Thus, the NLOS channel gain which include an infinite order of reflections can be expressed as [79]:

$$H_\mathrm{NLOS}(f) = \mathbf{r}^\mathrm{T}(f)\mathbf{G}_\rho(\mathbf{I} - \mathbf{H}(f)\mathbf{G}_\rho)^{-1}\mathbf{t}(f), \tag{2.10}$$

where $\mathbf{G}_\rho = \mathrm{diag}(\rho_1, ..., \rho_N)$ is the reflectivity matrix of all N reflectors with ρ_i as the reflection coefficient of the ith reflector; and $\mathbf{I}$ is the unity matrix of size $N \times N$, and the transmitter transfer function vector is denoted as:

$$\mathbf{t} = [H_{1,\mathrm{Tx}}(f), H_{2,\mathrm{Tx}}(f), \ldots, H_{N,\mathrm{Tx}}(f)]^\mathrm{T}. \tag{2.11}$$

In (2.11), $H_{k,\mathrm{Tx}}(f)$ is the channel gain from the transmitter to the kth reflector while N denotes the total number of reflecting elements in the room. The entities in (2.11) are given as:

$$H_{k,\mathrm{Tx}}(f) = \frac{(m+1)A_k}{2\pi d_{k,\mathrm{Tx}}^2}\cos^m\phi_{k,\mathrm{Tx}}\cos\psi_{k,\mathrm{Tx}}\, e^{-\jmath 2\pi f\frac{d_{k,\mathrm{Tx}}}{c}}, \quad k = 1, \ldots, N, \tag{2.12}$$

where A_k is the area of the kth reflector element; $\phi_{k,\mathrm{Tx}}$ is the radiance angle to the kth reflector and $\psi_{k,\mathrm{Tx}}$ is the incidence angle with respect to the normal vector of the kth reflector. The Euclidean distance between the kth reflector and the transmitter is denoted by $d_{k,\mathrm{Tx}}$. In (2.10), the frequency-dependent transfer matrix, $\mathbf{H}(f)$ of size $N \times N$ describes the LOS transfer function between all surface elements, specifically between the kth and the ith reflectors which acts as the transmitter and receiver surface elements, respectively. $\mathbf{H}(f)$ can be described as:

$$\mathbf{H}(f) = \begin{pmatrix} H_{1,1}(f) & \cdots & H_{1,N}(f) \\ \vdots & \ddots & \vdots \\ H_{N,1}(f) & \cdots & H_{N,N}(f) \end{pmatrix}, \tag{2.13}$$

where the entities $H_{k,i}(f)$ are the LOS transfer function between the ith reflector [1] and the kth reflector. These entities can be expressed as:

$$H_{k,i}(f) = \frac{A_k}{\pi d_{k,i}^2} \cos\phi_{k,i} \cos\psi_{k,i} \, e^{-\jmath 2\pi f \frac{d_{k,i}}{c}}, \tag{2.14}$$

for $i, k \in \{1, \cdots, N\}$. Here, $\phi_{k,i}$ and $\psi_{k,i}$ are the radiance and incidence angles between pairs of reflectors i and k with respect to their normal vectors; $d_{k,i}$ is the Euclidean distance between the kth and ith reflectors. Finally, the receiver transfer function vector given as $\mathbf{r} = [H_{\mathrm{Rx},1}(f), H_{\mathrm{Rx},2}(f), \ldots, H_{\mathrm{Rx},N}(f)]^{\mathrm{T}}$ with the entities described as:

$$H_{\mathrm{Rx},i}(f) = \frac{A}{\pi d_{\mathrm{Rx},i}^2} \cos\phi_{\mathrm{Rx},i} \cos\psi_{\mathrm{Rx},i} \operatorname{rect}\left(\frac{\psi_{\mathrm{Rx},i}}{\Phi_{\mathrm{c}}}\right) e^{-\jmath 2\pi f \frac{d_{\mathrm{Rx},i}}{c}}, \tag{2.15}$$

where A is the PD area; $\phi_{\mathrm{Rx},i}$ and $\psi_{\mathrm{Rx},i}$ are the radiance and incidence angles between the ith reflector and the receiver. The Euclidean distance between the ith reflector and the receiver is denoted as $d_{\mathrm{Rx},i}$.

---

[1] It is assumed the reflectors are modeled as proper Lambertian radiators with $m = 1$.

2.3 Optical-Orthogonal Frequency Division Multiplexing (O-OFDM) Based Transmission

Realization of LiFi as an IM/DD system means that only positive and real signals can be successfully transmitted [18]. This limits the modulation schemes that can be employed. Typical modulation techniques that are used in LiFi systems can be categorized into: single carrier modulation (SCM) techniques and multiple carrier modulation (MCM) schemes. PPM, unipolar pulse amplitude modulation (PAM), PWM and OOK are common single carrier modulation techniques [9]. The disadvantages of using single carrier system is the lower spectral efficiency and as the communication speeds increase, the limited communication bandwidth leads to unwanted effects such as ISI [9, 65]. In comparison to SCM schemes, MCM techniques are more bandwidth-efficient and can offer higher data rates [81]. MCM is a method of transmitting data with different carrier frequencies. The main advantage of this technique is to cope with severe channel distortions and the capability of combating against ISI. In addition, MCM is more capable than SCM to cope with attenuation in high-frequency communications, such that in the visible light band [81]. Moreover, MCM has higher spectral efficiency and thus it is preferable for high-speed OWC.

OFDM is one of the most common and widely used MCM methods which is used in the first research objective of this study. OFDM is one effective solution to combat the effect of ISI which are introduced as a result of passing the signal through a dispersive optical channel at high-data-rate transmission and also using off-the-shelf limited-bandwidth LEDs [70, 78]. Benefits of using OFDM include: 1) efficient use of spectrum, 2) robustness against frequency selectivity of channel by splitting the channel into narrowband flat fading subcarriers, 3) simple channel equalization by using single-tap equalizer (while adaptive equalization techniques are being used in single carrier modulation schemes), 4) computationally efficient by using fast Fourier transform (FFT) and inverse FFT (IFFT) techniques [82]. Because of the bipolar and complex signals generated by the OFDM modulator, the conventional OFDM modulator cannot fit the IM/DD requirements where the signals should be positive and real-valued in LiFi systems [83]. Optical-OFDM (O-OFDM) is a unipolar solution that can be adopted in IM/DD-based transmission. There are several types of O-OFDM that can generate real and non-negative signals. Two of the most well-known and common types of O-OFDM are: DCO-OFDM and ACO-OFDM [84]. In the following, these two types of O-OFDM are introduced.

2.3.1 DCO-OFDM

Fig. 2.3 shows the block diagram of a DCO-OFDM system and its key elements. In a DCO-OFDM system, first the information bits are mapped to quadrature amplitude modulation (QAM) symbols. Then, each $\mathcal{K}$ consecutive modulated symbols are grouped and converted to parallel frames of OFDM to be used as the input of the IFFT module. An OFDM frame can be expressed as [21]:

$$\boldsymbol{X} = [0, X_1, ..., X_{\mathcal{K}/2-1}, 0, X^*_{\mathcal{K}/2-1}, ..., X^*_1], \tag{2.16}$$

where X_k for $k = 1, \cdots, \mathcal{K}$ are modulated data symbols transmitted on kth OFDM subcarrier. To generate real valued signals in time domain, Hermitian symmetry is applied to the OFDM frame, which specifies the following conditions:

$$\boldsymbol{X}(k) = \boldsymbol{X}^*(\mathcal{K} - k), \tag{2.17a}$$

$$\boldsymbol{X}(0) = \boldsymbol{X}(\mathcal{K}/2) = 0, \tag{2.17b}$$

where $(\cdot)^*$ denotes the complex conjugate operator. After the IFFT operation, time-domain samples are given as:

$$x[n] = \frac{1}{\sqrt{\mathcal{K}}} \sum_{k=0}^{\mathcal{K}-1} X(k) \exp\left(\frac{\jmath 2\pi k n}{\mathcal{K}}\right), \qquad 0 \le n \le \mathcal{K} - 1. \tag{2.18}$$

After passing through the IFFT module, a cyclic prefix (CP) will be added to the samples in order to combat the ISI due to the dispersive wireless channel. After adding the CP, the samples will be fed into a DAC module. A DC bias will be added to the analog waveform to ensure the modulated signal, $\tilde{x}(t)$, must be positive. The positive constraint is required for optical systems that perform intensity modulation. Therefore,

$$x_{\mathrm{e}}(t) = x_{\mathrm{DC}} + \tilde{x}(t), \tag{2.19}$$

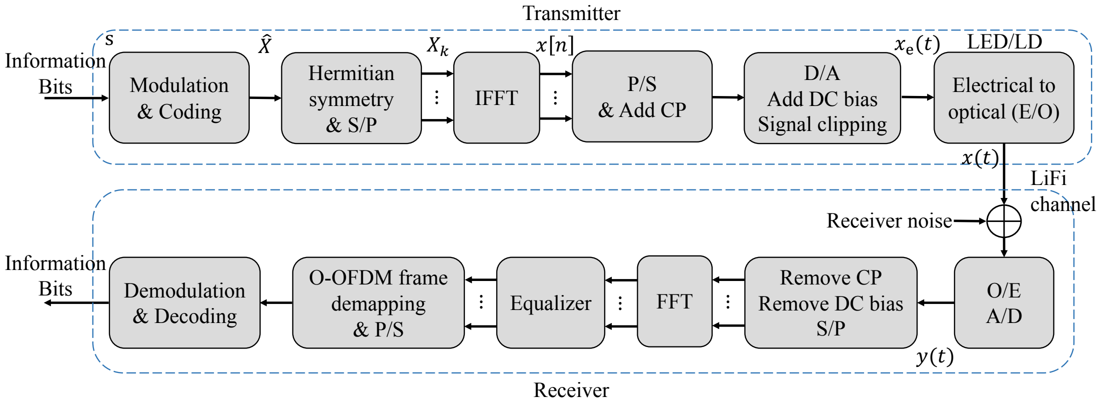

Figure 2.3: *Illustration of DCO-OFDM system.*

where

$$x_{\mathrm{DC}} = \eta\sqrt{\mathbb{E}[\tilde{x}^2(t)]}, \tag{2.20}$$

and η is the conversion factor. In general, the condition $\eta = 3$ guarantees that less than 1% of the signal is clipped. In this case, the clipping noise is negligible [83]. The current signal $x_{\mathrm{e}}(t)$ drives the LED to generate the optical signal $x(t)$. At the receiver, the received signal is first converted from an optical signal to an electrical signal using a PD. The processing after this point is the same as a conventional OFDM receiver.

2.3.2 ACO-OFDM

DC bias used in DCO-OFDM is inefficient in terms of optical power, thus, ACO-OFDM is another type of energy-efficient O-OFDM that can prevent adding the DC bias to the signal. In ACO-OFDM, only odd subcarriers are used to bear information in which the even subcarriers are discarded and only the odd subcarriers are demodulated [21]. Thus, the even subcarriers form a bias signal which ensures that the transmitted OFDM signal meets the non-negativity requirement [85]. Compared to DCO-OFDM, half of the spectrum is sacrificed by ACO-OFDM to make the time-domain signal unipolar. The use of only half of the subcarriers to carry data in ACO-OFDM results in a loss of spectral efficiency. Therefore, the signal generated after IFFT is an anti-symmetric real value given as [21]:

$$x[n] = -x[n + \mathcal{K}/2], \qquad 0 \leq n \leq \mathcal{K}/2. \tag{2.21}$$

The anti-symmetry property of $x[n]$ guarantees that no information data is lost due to signal clipping at the zero level.

2.4 LiFi Attocell Networks

The coverage area of a typical point-to-point VLC link is in the order of a few square meters [86]. However, to support mobility and seamless connectivity, one possible solution is to utilize several LED transmitters or access points and connect them as a networked system. This is known as a LiFi attocell network. A LiFi cellular network consists of several LiFi attocells, which are smaller than RF femtocells. In a LiFi network, depending on the illumination feature of the indoor environment, AP deployment can be: i) square deployment, ii) hexagonal deployment, iii) Poisson point process (PPP), or iv) hard-core point process (HCPP) [80]. In this research study, we only consider the square network as it is the typical deployment in offices and rooms. The geometric configuration of an indoor LiFi attocell network is shown in Fig. 2.4.

As shown in Fig. 2.4, a LiFi network comprises multiple LED transmitters (i.e., APs) arranged on the vertexes of a square lattice over the ceiling of an indoor network. At the UE, a PD tuned on the visible light band is employed for receiving downlink data. The LEDs are assumed to be point sources with Lambertian emission patterns. To avoid nonlinear distortion effects, the LEDs operate within the linear dynamic range of the current-to-power characteristic curve. In addition, the LEDs are assumed to be oriented vertically downwards, and the UE are randomly oriented. Only one AP is selected to serve the UE based on the received signal intensity. Thus, an optical attocell is defined as the confined area on the UE plane in which an AP serves the UE.

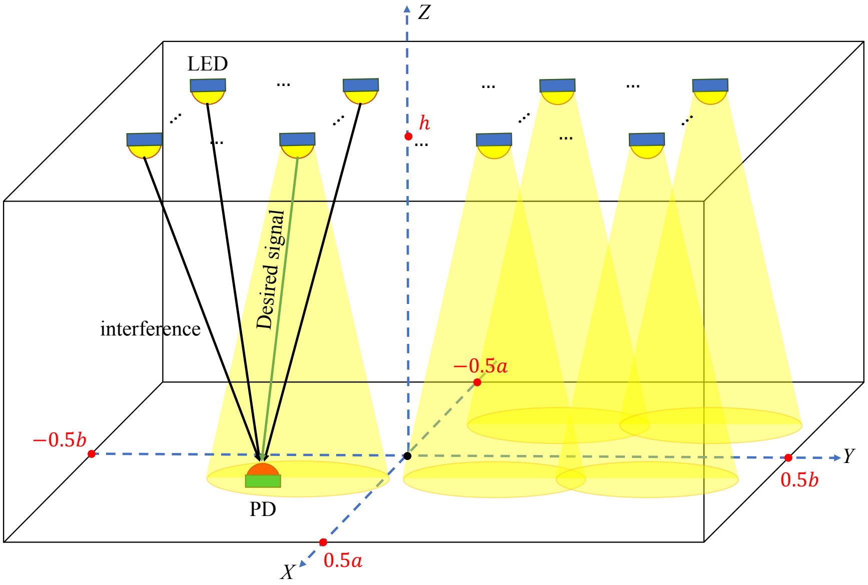

Figure 2.4: *LiFi attocell downlink system configurations.*

2.5 Multiuser Access Techniques

Like in RF networks, LiFi attocell networks should also be capable of supporting multiuser data communications by means of multiple access techniques. In this section, we study a common and widely used multiple access schemes in LiFi cellular networks that we also considered throughout this research study named orthogonal frequency division multiple access (OFDMA). OFDMA enables users to use frequency resources at different subcarriers and it has been widely considered and implemented in the downlink of long-term evolution (LTE) systems [87]. Fig. 2.5 illustrates the concept of subcarrier utilization by the OFDMA technique. Multiple access can be achieved in OFDMA by allocating subsets of subcarriers to individual users. Note that based on the required quality of service (QoS), the achievable data rate can be controlled individually for each user. This can be realized through assigning various numbers of subcarriers to different users. Therefore, OFDMA has been recently considered as a promising and practical option for downlink transmission [13].

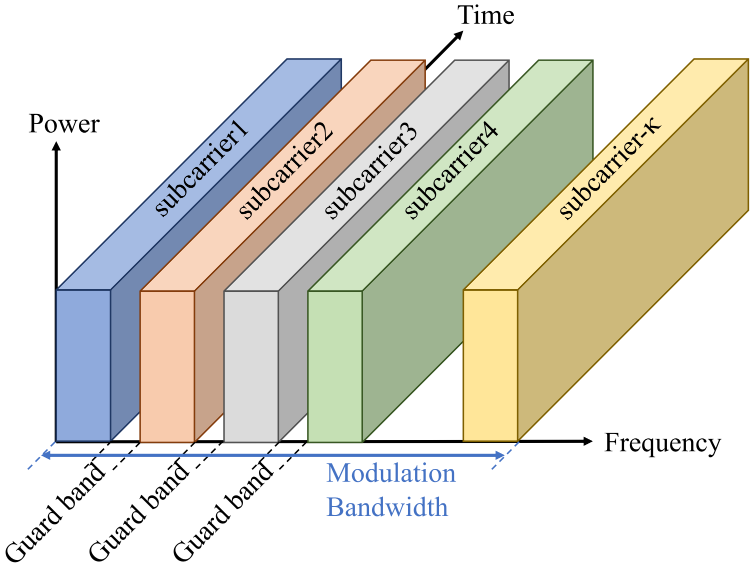

Figure 2.5: *Illustration of OFDMA*

2.6 User Behavior Models

In a LiFi cellular network, the channel gain depends on several factors including device random orientation of the UE, link blockage and user distribution. Device orientation and link blockage are the two significant factors that can affect the signal strength in LiFi networks. In the following, these factors are discussed.

2.6.1 Device Orientation

Device orientation can significantly affect the seamless connectivity of a user. The modelling and impact of device orientation in LiFi networks has been studied in [45, 88–91]. To incorporate the random orientation of a UE, an experimentally validated model proposed in [45] is used in this thesis which describes the random orientation of mobile devices. Fig. 2.6 shows the geometrical representation of the LiFi network considering an arbitrary orientation. In this figure, $\mathbf{n}'_{\mathrm{u}}$ is the rotated normal vector of the UE, θ_{u} is the angle between $\mathbf{n}'_{\mathrm{u}}$ and the link connecting the source and the UE, and Φ_{c} is the semi-angle FOV. Moreover, θ is the polar angle between the positive direction of the Z-axis and the UE normal vector, while ω is the azimuth angle of the UE. For a better physical interpretation, Ω is defined as the movement direction angle of the user expressed

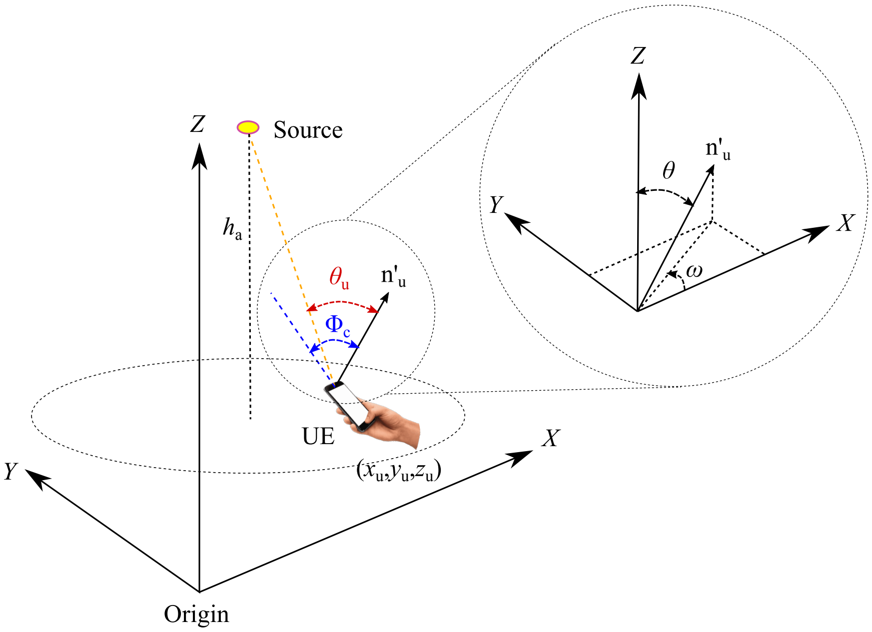

Figure 2.6: *Geometry of a randomly oriented user device.*

as $\Omega = \omega + \pi$ if $\omega \leq \pi$, and $\Omega = \omega - \pi$ if $\omega > \pi$. The UE rotated normal vector can be defined as:

$$\mathbf{n}'_{\mathrm{u}} = [\sin(\theta)\cos(\omega), \sin(\theta)\sin(\omega), \cos(\theta)]^{\mathrm{T}}. \tag{2.22}$$

Based on the experimental measurements reported in [45], it should be noted that the probability density function (PDF) of the polar angle, θ follows a Laplace distribution for sitting or static users and a Gaussian distribution for mobile users. Furthermore, it is also shown that the azimuth angle follows a uniform distribution.

2.6.2 Blockage

Due to the nature of LiFi, the link between a transmitter and a receiver can be blocked by an opaque object. More specifically, blockage of the LOS link could be due to the user body itself (i.e., self-blockage), or due to any other external blockage (e.g., blockage by furniture or other users). Consider a 3D indoor environment as depicted in Fig. 2.7, this figure demonstrate a typical example of the geometry of the room where one UE has a direct LOS to the source while the other UE is blocked by the user body. The body blockage can be modeled based on [92]

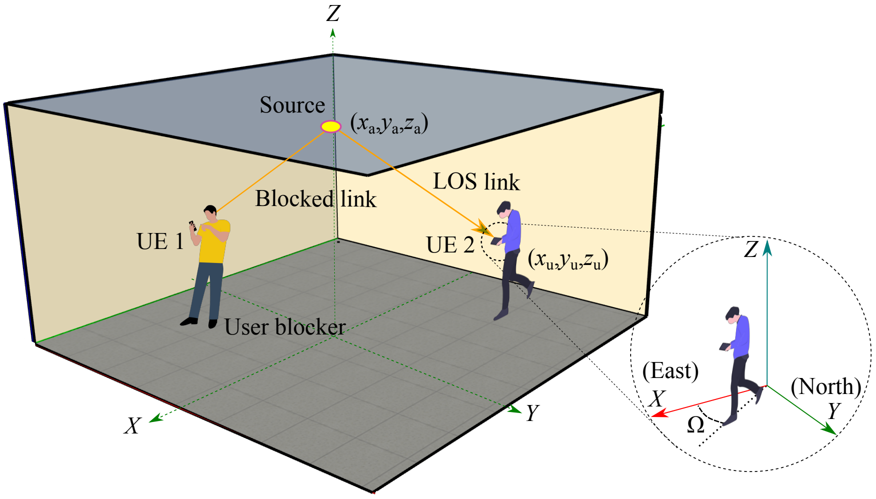

Figure 2.7: *Geometry of an indoor LiFi system showing the LOS link, blocked link and direction of the user.*

where the following conditions need to be checked: i) whether the position of the user body (or any other blockers) on the X-Y plane is in between the source and the UE, and ii) whether the height of the user body (or any other blockers) obstructs the LOS link between the source and the UE. For the first condition, referring to Fig. 2.8a where it is assumed that on the X-Y plane, a body with width w_b facing the UE shadows an area defined by the shadowing angle ϕ_b expressed as [92]:

$$\phi_\text{b} = 2\tan^{-1}(w_\text{b}/2r_\text{b}), \tag{2.23}$$

where r_b is the distance between the UE and the user body. The angle between the source and the UE on the X-Y plane, measured from the positive direction of the X-axis of the UE is defined as θ_a. We define Θ_b as the range of azimuthal angles where the body is in between the source and the UE which can be expressed as $\theta_\text{a} - \frac{\phi_\text{b}}{2} \leq \Theta_\text{b} \leq \theta_\text{a} + \frac{\phi_\text{b}}{2}$. It is assumed that if the UE azimuth angle, ω falls within this range, then the user body is definitely in between the source and the UE. Fig. 2.8a shows the scenario where the direction of the user body is outside of the range Θ_b and therefore does not block the UE. Note that the blockage by other external blockers is not a function of the direction of the main user and only depends on whether those blockers are between the source and UE. If the user body (or any other external blocker) is in between the source and the UE, the second condition determines whether or not the UE is blocked by the

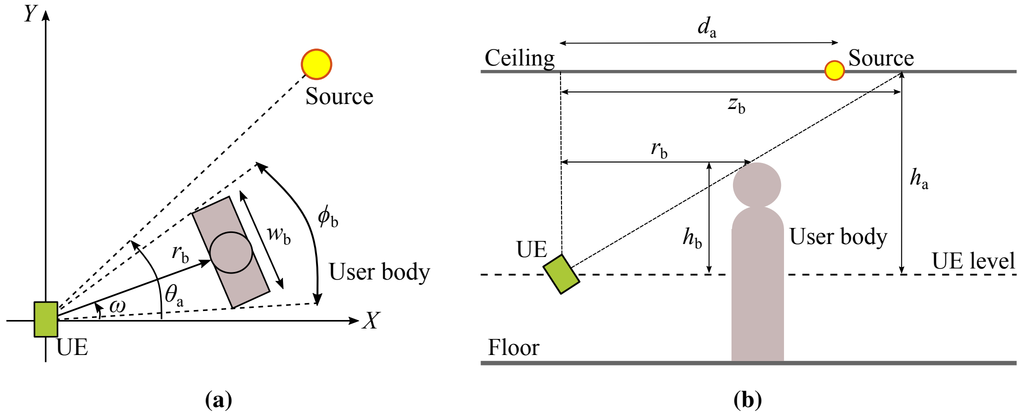

Figure 2.8: *Geometry of the body blockage model: (a) top view and, (b) side view.*

user body based on the height of the user. Fig. 2.8b shows the geometry of the body blockage model from the side view, where r_b denotes the distance between the UE and the user's body (or any other blockers). The radius of the blockage-free zone, z_b can be defined as [92]:

$$z_\text{b}(r_\text{b}) = h_\text{a} \cdot (r_\text{b}/h_\text{b}), \tag{2.24}$$

where h_b and h_a are the height difference between the user (or any other blockers) and the UE, and the height difference between the source and UE, respectively. Therefore, following the second condition, assuming that if the distance between the source and UE, denoted as d_a, is smaller than z_b, then the source is within the blockage-free zone, and the UE is not blocked by the user as shown in Fig. 2.8b. Otherwise, if d_a is larger than z_b, the source is outside of the blockage-free zone and the UE is considered to be blocked by the user.

2.7 Deep Neural Network Architectures

In order to achieve a high-speed LiFi system, having a realistic LiFi channel models is crucial for the system design. Channel components such as LOS and NLOS, random user device orientation, presence of the human body and furniture can provide a more realistic indoor LiFi environment [25], however considering them would increase the complexity of the channel model. Considering a realistic indoor environment, the performance of a LiFi network such as signal detection and resource allocation can be improved with accurate estimation of the channel knowledge. As previously mentioned, the information based on the LOS, NLOS, user behavior and furniture would provide better estimation of the quality of the wireless links [24]. However, solutions for channel estimation usually assume a general LiFi system settings which is not practical in real-life settings [28–31]. Channel estimation techniques such as LS and MMSE have been widely studied in the literature and when compared to DL techniques, it was shown that DL are capable of achieving significant gain in channel estimation compared to these conventional techniques [38]. Due to the increased complexity in the channel modelling, accurate channel estimation without the perfect channel knowledge is highly desirable. Thus, this motivates the need for DL to be used as an alternative approach to model a realistic LiFi channel as well as to offer a joint channel estimation and signal detection/resource allocation process that can be performed indirectly in real time by viewing the channel as a black box. By accurately identifying the complex mapping relationship between the input and output data, DL can address the overall channel impairments efficiently in order to recover the original symbols or to allocate the resources to users efficiently. In addition, it effectively reduces the pilot overhead compared to the traditional channel estimation techniques as shown in [38].

The implementation of DL requires a generation of sufficiently large amount of training data to be fed into the learning algorithm [93]. The DL process constitutes of two stages; offline training and online implementation. Using the realistic channel models that well describe the real channels and considering an optimal solution for the problem of interest, the training data can be generated by simulation. During training, the DL model learns a mapping function between the input and the output and minimizes the error between the output of the model with the actual value of the output signal [93]. Once the network is trained, it can be employed in real time deployment stage to give an accurate estimate of a desired task in which the system can be viewed as a black box. It should be noted that one of the features of the indoor environment is that the furniture does not necessarily move every minute or every hour. Therefore, the indoor environment can remain unchanged for some period of time [8]. In this case, training the deep learning methods based on a large set of channel realizations which consider random device orientations, random user locations, etc., is enough to help increase the generalization ability of the network. If the system changes over time (e.g., due to the placement of furniture at different locations), transfer learning can be used to update the deep learning network [94]. For the system to adapt to new changes, the part of systems that can be fixed and the part that needs to be fine-tuned should be determined. This can be considered as a future research direction. In the following subsections, commonly used deep learning methods in the literature known as LSTM and feedforward neural network (FNN) which are adopted in this thesis are introduced.

2.7.1 Feedforward Neural Network (FNN)

FNN, also known as multi-layer perceptron (MLP) is considered as the most popular type of supervised learning method used to solve nonlinear problems [95]. It has found success in many applications especially for classification problems and is favourable to be used for tasks that involves a deterministic mapping between input and output [95]. MLP in its most basic form is a type of feedforward artificial neural network (ANN) and is also known as the foundation architecture of deep feedforward neural network (DFNN) or deep learning. DFNN as shown in Figure 2.9, is a fully connected network which consists of an input layer which receives the input data, an output layer that makes the prediction or decision of the input signal, and one or more hidden layers which are considered as the network's computational engine. The output of a DFNN network is usually determined using a variety of activation functions such as rectified linear unit (ReLU), tanh and sigmoid. During the training process, an algorithm called 'backpropagation' is used as a supervised learning technique while various optimization approaches such as stochastic gradient descent (SGD) and adaptive moment estimation (ADAM) are also applied [96]. Furthermore, in order to achieve an optimal performance, the network requires tuning of several hyperparameters such as the number of hidden layers, neurons and iterations.

In this thesis, to ease the learning process and achieve better learning performance, ReLU function is used which can be mathematically defined as [97]:

$$\sigma_{\text{ReLU}}(x) = \max(0, x). \tag{2.25}$$

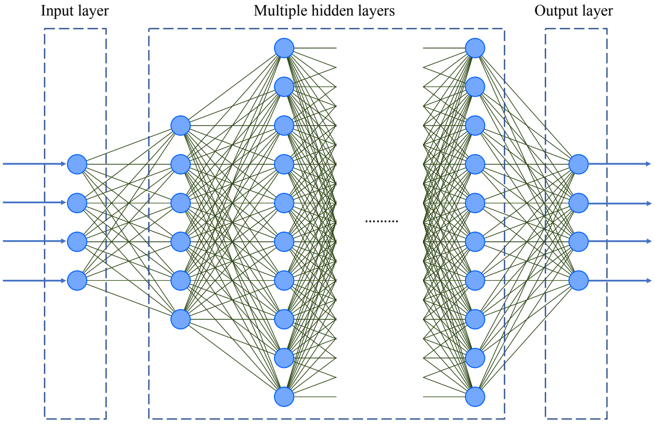

Figure 2.9: *Architecture of a deep feedforward neural network.*

Therefore, the forward propagation of DFNN can then be described as [98]:

$$z_i^{(l)} = \mathrm{W}_i^{(l)}\mathrm{y}^{(l-1)} + b_i^{(l)}, \qquad y_i^{(l)} = \sigma_{\mathrm{ReLU}}(z_i^{(l)}), \tag{2.26}$$

where $z_i^{(l)}$ is the output of the lth layer, $\mathrm{W}_i{}^{(l)}$ is the weight coefficient, $\mathrm{y}^{(l-1)}$ is the output of the previous layer, $\mathrm{b}_i{}^{(l)}$ denotes the bias, and finally $y_i^{(l)}$ denotes the output of lth layer after undergoing the nonlinear operation. During the backpropagation, the output values are compared with the target values in order to calculate the error. The error can be calculated by means of a loss function (e.g., mean square error (MSE)) which is then fed back through the network where the algorithm adjusts the weights of each connection in order to reduce the error. This process is called supervised learning [98].

2.7.2 Types of Recurrent Neural Network

Standard feedforward neural networks are unable to handle long sequence data well since they do not have a way to feed information from a later layer back to the previous layer. Thus, recurrent neural networks (RNN) have been introduced to take temporal dependencies into account. However, the shortcoming of RNN is that long-term dependencies due to the vanishing gradient problem cannot be handled [99]. Hence to overcome this issue, LSTM networks were introduced, which are a special case of RNN. LSTM takes both long-term and short-term dependencies in sequence data into account [95]. Similarily, gated recurrent unit (GRU) networks are an improvement of LSTM which also takes long-term dependencies into consideration with faster optimization [99]. However, it was shown in [99] that when RNN, LSTM, and GRU performances are evaluated on a reduced data set, the results demonstrate that LSTM achieves the best performance compared to the other techniques. The architecture of RNN, LSTM and GRU are discussed in the following subsections.

2.7.2.1 Recurrent Neural Network (RNN)

In RNN, the decision made at time $t-1$ affects the decision at time t. Therefore, the decision of how the network will respond to new data is dependent on the current input and the output from the recent past. RNN calculates its output by iteratively calculating the following equations [99]:

$$h_t = \sigma_h(\mathrm{W}_{xh}x_t + \mathrm{W}_{hh}h_{t-1} + b_h), \tag{2.27}$$

and

$$y_t = \mathrm{W}_{hy}h_t + b_y, \tag{2.28}$$

where x is the inputs, y is the output sequence, h is the hidden vector sequence at time slices $t = 1$ to T. W denotes the weight matrices, and b represents the biases. Moreover, σ_h is the activation function used at the hidden layers.

2.7.2.2 Long Short-Term Memory (LSTM) Neural Network

LSTM is a recurrent neural network capable of learning long-term dependencies between data sequence and has achieved success in sequence prediction problems [100, 101]. Their hidden layers consist of memory cells controlled by 'gates' which regulates the flow of information into and out of the memory cell. Hence, they decide what new information to be input to the cell, what old information to be discarded, and what will be the updated information to be output from the cell. Since LSTM has internal memory and makes its decision by considering the current input and the previous outputs, it can perform extremely well in processing sequences of data. This makes LSTM applicable to the signal detection problem as sequences of transmitted and received symbols are used to train the neural network. Figure 2.10 shows the typical architecture

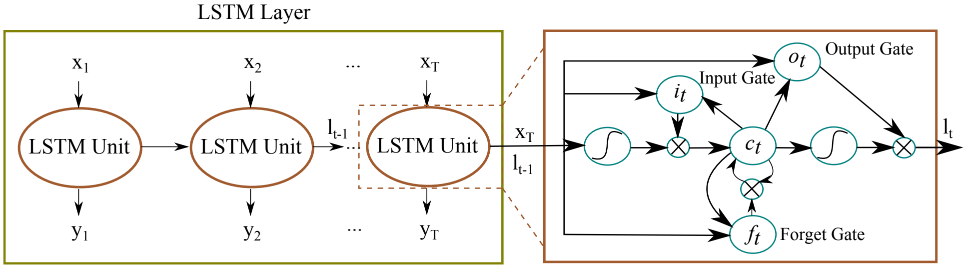

Figure 2.10: *Architecture of an LSTM layer. The LSTM unit takes the previous state of the network,* l_{t-1} *and the input sequence,* x_T *and computes the output* y_T *and the updated state* l_t*.*

of an LSTM network. The sequence of operations in LSTM at time step t can be found in [102]. LSTM consists of sigmoid gate activation function, $\sigma_g(.)$ and hyperbolic activation function, $\tanh(.)$ that act as squashing functions to ease the training of the network. The sigmoid function is considered as a gating function where it decides how much information will pass through the cell gates.

2.7.2.3 Gated Recurrent Unit (GRU)

GRU was first introduced in [103], where this neural network is similar to LSTM but with fewer parameters. GRU have gated units similar to LSTM which controls the flow of information inside the unit but without having separate memory cells. Unlike LSTM, GRU does not have an output gate, thus exposing its full content. The formulations of GRU are described in the following [99]:

$$r_t = \sigma_g(\mathrm{W}_{xr}x_t + \mathrm{W}_{hr}h_{t-1} + b_r), \tag{2.29}$$

and

$$z_t = \sigma_g(\mathrm{W}_{xz}x_t + \mathrm{W}_{hz}h_{t-1} + b_z), \tag{2.30}$$

and

$$\overline{h}_t = \tanh(\mathrm{W}_{xh}x_t + \mathrm{W}_{hh}(r_t \cdot h_{t-1}) + b_h), \tag{2.31}$$

and

$$h_t = z_t \cdot h_{t-1} + (1 - z_t) \cdot \overline{h}_t, \tag{2.32}$$

where r_t, z_t, x_t, and h_t are the reset gate, update gate, input vector and output vector, respectively. Both LSTM and GRU are equally capable of handling long term dependencies, and have been proved to be comparably efficient [104].

2.8 Reconfigurable Intelligent Surface

Recently, reconfigurable intelligent surfaces has gained interests due to its capability of modifying the wireless channel to improve the communication performance. Consequently, it has emerged as one of the most effective solutions to diminish the effect of blockage by providing alternative LOS paths when there exists an obstacle between the transmitter and receiver [49]. In LiFi, RIS usually comprises of a number of reflecting elements (e.g., mirror array) which manipulate/reflect the incident light towards a desired location in order to gain high-power signal [49]. In the current literature, RIS has been shown to be very successful in many different applications of the wireless communication systems [105–107]. Hence, due to its interesting properties, it is worth to incorporate RIS into the realistic indoor LiFi system and investigate the different designs of RIS that can best alleviate the joint blockage effect caused by several blocking factors such as the optical receiver's limited FOV, UE random orientation, self-body blockage and blockage by other external blockers (e.g., other users and furniture).

In this thesis, the incorporation of RIS is considered in the LiFi system to alleviate the effect of LOS blockage. RIS is an array of passive reflecting elements mounted on a wall which can be used to overcome blockage by focusing the incident light beam towards the user device. In this work, RIS is assumed to be of size $N_{\text{ris}} \times N_{\text{ris}}$ reflecting elements which are optimally oriented so that the angle of reflection of the LOS link is aligned towards the center of the UE. The geometry of the light propagation when RIS is included into the room environment is illustrated in Fig. 2.11 where the LOS link and reflected path by RIS are shown. As shown in the figure, it is assumed that RIS produce a specular reflection path where geometrically, the angle of irradiance equals to the angle of incidence (i.e., Snell's law of reflection). The reflected path through an RIS element is composed of two components: 1) The path from the source to RIS reflecting element, 2) The path from RIS reflecting element to the UE. In order for the UE to receive the signal, either the LOS path or RIS-reflected path must fall within the FOV of the receiver, Φ_{c} as

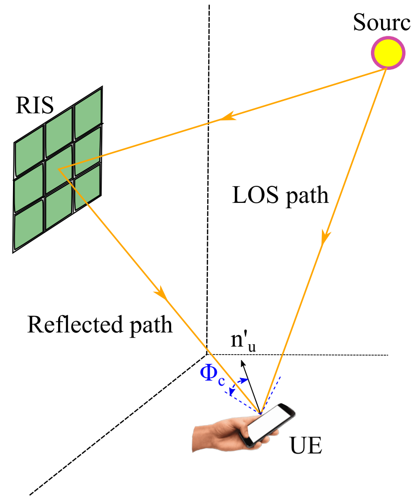

Figure 2.11: *Geometry of light propagation model for LOS between the source and UE, and a reflected path from RIS.*

shown in Fig. 2.11. Hence, the channel gain of the first reflected link by the n-th RIS reflector can be expressed as [108]:

$$H^{\mathrm{RIS}}_{\mathrm{u},n,\mathrm{a}} = \frac{\rho_n(m+1)}{2\pi(d_{\mathrm{a},n}+d_{n,\mathrm{u}})^2} A_{\mathrm{u}}\cos^m(\phi_{\mathrm{a},n})\cos(\psi_{n,\mathrm{u}})\mathrm{rect}(\frac{\psi_{n,\mathrm{u}}}{\Phi_{\mathrm{c}}}), \tag{2.33}$$

where ρ_n is the reflection coefficient of the n-th RIS reflecting element, $\phi_{\mathrm{a},n}$ and $\psi_{n,\mathrm{u}}$ denotes the radiance angle from the transmitter to the n-th reflector and the incidence angle from the n-th reflector to the UE, respectively. $d_{\mathrm{a},n}$ and $d_{n,\mathrm{u}}$ define the distance between the AP and the n-th reflector, and the distance between the n-th reflector and the UE, respectively.

2.9 Summary

In this chapter, LiFi including the channel responses of both front-end elements and LiFi have been studied. The LOS and NLOS DC gains have been explained and optical OFDM, which is an effective way of combating the ISI in LiFi networks, is described. The basic concept of LiFi attocells are provided and OFDMA as the most common multiuser access techniques in the downlink are described. The user behavior models which include the device orientation and blockage that can affect the system performance are explained. Different types of deep learning algorithms for solving non-linear channel estimations are discussed. Finally, RIS which is a method of diminishing the blockage effects are described.

Chapter 3

Learning Indoor Environment for Effective LiFi Communications

3.1 Introduction

In an indoor environment, the information on the channel condition (e.g., channel gain) can be exploited to improve the communication metrics such as the signal-to-noise ratio, bit-error ratio and user throughput [17]. For simplicity, most of the existing works assume general geometries and a deterministic channel to model an indoor LiFi system [109–111]. However, in a practical scenario, there are many contributing factors such as specific geometrical configurations of the network and the user behavior effects which are strong enough to influence the system's performance and therefore cannot be ignored during the communication system design. The LiFi channel highly depends on the behavior of light (e.g., line of sight, non-line of sight, link blockage), the geometry of the indoor environment (e.g., placement of furniture) and the behavior of the user (e.g., random orientation of the UE and hotspots). These effects make the performance of LiFi communication and networking schemes such as OFDM signal detection and resource allocation highly dependent on the specific features of the indoor environment. Hence, it is worth to investigate whether it is possible to adapt the design of the LiFi systems to the underlying indoor environment using learning techniques.

To optimize the performance of a LiFi OFDM system, accurate channel state information is required. CSI can be obtained using traditional channel estimation (CE) techniques such as LS and MMSE but with certain estimation errors. Nevertheless, these pilot-based CE approaches are commonly used and work well for linear systems. A study in [38] compared the performance of these two methods for CE in OFDM systems and show that LS provides a simple implementation but give insufficient channel estimation and detection performance due to not having any prior channel statistics. Meanwhile, MMSE is capable of offering a better channel estimation as it takes influence of noise into account but has higher computational complexity due to the inverse operations of the channel matrix. Their results show that when less pilots were used to estimate the channel, the BER curves of the LS and MMSE methods saturate when SNR is above 10 dB. Several works on CE in OWC systems (e.g., [112]) have used a generalized channel model (e.g., based on Gaussian channel gain) that does not consider user behavior and the geometry of the indoor environment. A deep neural network based CE method was proposed in [113] that can reduce the spectrum resources occupied by channel estimation compared to LS and MMSE, assuming point-to-point VLC system with only LOS channel considered. Compared to this thesis, the authors in [113] only considered LOS channel in their system and ignore the effect of blockage and user behavior. CE for indoor VLC systems assuming Gaussian channel gains have been discussed in [114] and [115], taking into consideration the types of reflectors' materials and light sources. Note that the existing works focused on a uniform scenario of the indoor LiFi systems where the effect of NLOS, link blockage, UE's random orientation and user hotspots were not considered.

Machine learning schemes such as deep learning can be used as an alternative approach to model a realistic LiFi channel. In contrast to the traditional approaches, DL offers a simple estimation process that can be performed indirectly in real time by viewing the channel as a black box. Useful channel information (e.g., channel gain, SNR, BER, etc.) which may not be easily or directly measured using conventional methods can be simply learned by the DL model based on the environment and the information on user behavior (e.g., UE orientation and hotspots) in order to consider the specific underlying geometry. Over the years, DL has achieved great success in designing different aspects of wireless communication systems, such as modulation, positioning, resource allocation, etc.. In [116], an automatic modulation recognition framework for detection of radio signals was proposed using convolutional neural network (CNN) and LSTM. The authors in [117], have proposed an iterative point-wise reinforcement learning for highly accurate indoor visible light positioning. In [38], the authors proposed a deep neural network (DNN) based CE technique for learning the wireless channel in an OFDM system. The proposed technique was shown to be more robust than the traditional methods (e.g., LS and MMSE) especially when fewer pilots were used, cyclic prefix were removed and with presence of nonlinear clipping noise. A reinforcement learning (RL) technique based on a meta-learning was proposed in [118] for access point selection and user association in terahertz (THz)/VLC wireless virtual reality (VR) networks that can accurately locate VR users using VLC and build THz links to transmit high-quality VR images while avoiding blockages caused by other users. A DL-based detection algorithm for molecular communication systems were developed in [119] where the model was trained in the absence of channel knowledge. Moreover, an LSTM aided system was proposed in [120] to predict human mobility and improve the accuracy of handover management. It can be envisioned that DL proposes a very promising solution to address the various channel characteristics and therefore can be applied in LiFi systems.

Considering a multiuser LiFi system, resource allocation and scheduling can become a vital issue as appropriate scheduling schemes are needed to ensure all of the available resource are allocated fairly to the users. It is important that these resources are allocated to users taking user behavior and specific geometry of the room into consideration as the LOS path can be easily blocked due to these effects. Hence, in this case, users with the worse channel should be prioritised for resource allocation. PF scheduling has been considered as an attractive bandwidth allocation criterion in wireless networks, capable of supporting high resource utilization while maintaining good fairness among network flows. Typically, it requires full channel knowledge which is practically difficult to obtain. The existing applications of PF has proven that it ensures a level of fairness to users [121, 122], however they do not account for the NLOS channel, user behavior and the specific geometry of the network. As the frequency response of the LiFi channel can be highly environment-dependent, it is important to consider these effects to ensure priority is given to the user with the poorest channel. DL has found success in solving resource allocation problems in LiFi systems under specific scenarios [123–125]. However, the literature mostly assume generalized channel models and neglect the effect of furniture and user behavior.

In order to incorporate the distinct features of realistic indoor environment in the design of LiFi systems, DL techniques are implemented in this chapter considering DL fits wireless communication channels well, and the principle is to train the deep neural network to fit the channel response through data. It is shown that DL can be very effective in learning specific characterizations of the indoor LiFi channels as well as the corresponding non-random user behavior imposed by the specific indoor environment (e.g., based on the furniture configuration, etc.), outperforming the traditional CE techniques. Hence, it is proven that DL techniques can learn and analyze the characteristics of channels, generate a model to help recover noisy signal and substitute for conventional CE techniques. Compared with the traditional CE scheme, it offers a method using fewer pilots and could work under bad conditions. To the best of our knowledge, this is the first time that DL-based communication schemes are investigated in the presence of a realistic LiFi channel in a typical room with furniture and different user behaviour while considering important effects such as the random orientation of the user device, blockage of LiFi links due to the existence of furniture and self-blockage by the users, and an infinity order of the NLOS channel components. Two deep learning-based schemes are designed for signal detection and resource allocation for LiFi communication in a realistic indoor environment based on LSTM and feed forward neural networks, respectively. The networks are trained considering specific geometrical configurations of the indoor environment and conditional hotspot models based on varying user distributions to show the effectiveness of our schemes in adapting to a particular scenario compared to the benchmark conventional methods. It is shown that when partial CSI is available, these schemes are able to indirectly estimate the underlying channel characteristics and improve the performance of signal detection and user scheduling. In practical scenarios with limited instantaneous CSI, the proposed methods can perform close to the optimal performance in the presence of full channel knowledge.

The rest of this chapter is organized as follows. Section 3.2, describes the system configuration. The problem formulations for signal detection and resource allocation are explained in Section 3.3. The deep learning implementation for signal detection and resource allocation in LiFi are introduced in Sections 3.4 and 3.5, respectively. Finally, the conclusions are drawn in Section 3.6.

3.2 System Configuration

A single input/single output (SISO) configuration of a LiFi system is assumed in this work where one access point transmits and one photodiode detects the signal. The LiFi system comprises of an LED transmitter located at the ceiling, facing vertically downwards and a PD receiver mounted on a user equipment, initially assumed to be oriented vertically upwards. In our analysis, we consider stochastic geometry to model the mobile nature of the users while we use the random orientation model proposed in [126] to consider the effect of receiver tilting as well as other realistic channel characteristics. We assumed that the indoor mobile network is quasi-static where the user can take different locations and random orientation angles. Hence, each channel realizations comprises of a snapshot of the network. Based on [126] and [127], it has been reported that the coherence time of the LiFi channel is in the order of a few hundreds of milliseconds (i.e., 130 ms) which justifies the assumption of quasi-static channel considering the typical data rates of LiFi systems. It is worth mentioning that for multiple cells, the user in a particular cell would be connected to one of the APs, while the signal from the remaining APs whould be considered as interference. Hence, an additional scenario where multiple LEDs are placed on the ceiling and the effect of interference from neighboring APs are considered to show that the average effect of interference is not significant on the overall performance and the generalization of the DL-based methods.

In LiFi systems, multiuser access can be supported by means of multiple access technique. In the following sections where we discuss in detail the DL-based resource allocation approach, we consider orthogonal frequency division multiple access to allow users to share the frequency resources at different subcarriers. By allocating subsets of subcarriers to different users, multiple access can be achieved while the quality of service of different users can be controlled. Therefore, OFDMA is regarded as a practical choice for downlink transmission. As mentioned previously, PF scheduling technique can be used to fairly allocate these subcarriers to different users. The decision of subcarrier allocation to users is based on the instantaneous CSI and the moving average data rate of the user. Hence, user with the weakest channel gain and lowest average data rate is prioritized for the next subcarrier allocation. The implementation of PF scheduling for this research is further described in the next sections.

3.3 Problem Formulation for Signal Detection and Resource Allocation

The signal detection problem follows the classical maximum likelihood (ML) optimization where optimal detection is achieved by minimizing the distance between the received and transmitted signals. Hence, ML can be defined as [128, 129]:

$$\text{ML} : \min |Y - HX|^2 \tag{3.1}$$

where Y, X and H are the received signal, transmitted signal and the channel gain, respectively.

The resource allocation problem is based on the PF scheme where it begins with the calculation of the priority for each user at each subcarrier, then the user with the maximum priority is assigned the subcarrier. The priority of the jth UE for the kth subcarrier is calculated based on the following metric [17, 42]:

$$\text{PF} : \arg\max_{j} \frac{R_{\text{req}}}{\bar{R}_j} \tag{3.2}$$

where $\bar{R}_j$ is the average data rate of the jth UE before allocating the kth resource, and R_{req} is the requested data rate of the jth UE. The algorithm then continues to assign the subcarriers to the user with the next maximum priority until all of the frequency subcarriers are allocated.

In our work, we assume that the full CSI is not available, and therefore, prior to signal detection and resource allocation, the system must first estimate the channel based on pilot signals. In order to do the channel estimation, we follow the classical CE methods such as MMSE and LS. For MMSE, the goal is to obtain the estimate of H and X that jointly minimize the mean square error between the actual value of the received pilot symbols and the estimated value of the pilot symbols. Hence, MMSE can be defined as [33, 112, 130]:

$$\text{MMSE} : \min \text{E}[||(Y - HX)||^2] \tag{3.3}$$

The goal of LS estimator is to minimize the square distance between the received pilot signal and the original pilot signal which can be defined as:

$$\text{LS} : \min ||Y - XH||^2 \tag{3.4}$$

The important connection that can be noted between the signal detection and resource allocation problems is that both of the considered problems are being affected by limited number of pilots and require for channel estimation. Therefore, in our work, we are looking at how imperfect CSI will affect the problem in signal detection and resource allocation. It should be noted that these are classical problems and the focus of this work is not to modify them in that perspective but rather focusing on the effect of limited pilots, furniture, indoor environment, etc., to demonstrate the potential of the learning techniques in effectively enhancing signal detection and resource allocation in the absence of full CSI.

3.4 Deep Learning-based Signal Detection

The architecture of our DL-based DCO-OFDM is illustrated in Fig. 3.1. As seen in the figure, the system is very similar to the conventional OFDM. The main difference is that firstly, the transmitted signal in DCO-OFDM must have Hermitian symmetry and secondly, a DC bias should be applied before transmitting the signal through the channel. This is to fulfil the requirements where the signal to be transmitted in IM/DD systems must be both real and non-negative. During the real-time operation, a sequence of symbols are randomly generated at the transmitter which then undergo modulation. Then, pilot symbols are uniformly inserted into the transmitting sequence. Due to Hermitian symmetry, the transmitted signal becomes real after going through IFFT. This means that the input sequence to the IFFT block should be in the form of $\boldsymbol{X} = [0, X_1, \ldots, X_{\mathcal{K}/2-1}, 0, X^*_{\mathcal{K}/2-1}, \ldots, X^*_1]$, where $\mathcal{K}$ is the total number of subcarriers and the modulated subcarriers carrying the information is only $\mathcal{K}/2-1$. Afterwards, in the time domain, CP is inserted and DC bias is added to make the signal positive before passing through the optical channel. At the receiver side, after removing the DC bias and the CP, FFT is performed to convert the signal from the time domain to the frequency domain. Hence, the received signal can then be described as: $Y(f) = H(f)X(f) + N(f)$ where $Y(f)$, $X(f)$, $H(f)$ and $N(f)$ are the FFT of $y(t)$, $x(t)$, $h(t)$ and $n(t)$, respectively. Finally, after demodulation, the estimated noisy version of the received symbols are fed as input to the trained LSTM model and the original transmitted data is recovered.

For the training stage, using the channel models discussed in Chapter 2, the training data can be generated by simulation. The training data is divided into training set and validation set. The latter is not used for training but is used to monitor the validation loss during the training process which helps determine if the network is overfitting the training data. In each simulation,

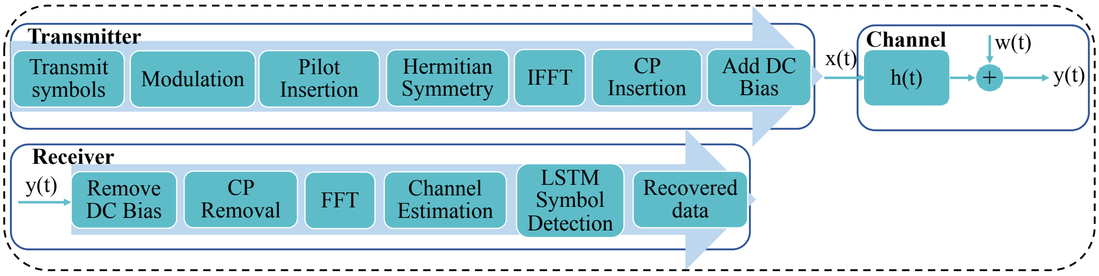

Figure 3.1: *The structure of deep learning-based DCO-OFDM system for signal detection.*

the transmitted signal undergoes channel distortions caused by the diffuse channel components and different noise samples to increase the generalization ability of the DL model during the online deployment stage. To collect the training data, a DCO-OFDM system with 127 subcarriers and quadrature phase shift keying (QPSK) modulation are considered. The transmit signal consist of 127 randomly generated symbols for 26 SNR values ranging from 0 dB to 50 dB. The generation of the same sequence of signal is repeated but added with different sequence of independent and identically distributed (i.i.d) noise samples in each iteration. In addition, to consider the randomness of the device orientation, the received signals were generated based on random samples of θ taken from a Laplace distribution with a mean value of 41° [126]. The user locations are chosen randomly either based on uniform distribution or the underlying hotspot model. In the locations where the user is sitting around a table, the direction of the user, Ω is fixed at a value of 45°, 135°, 225° or 315°, in order to face the table. In other locations, four samples of user direction were randomly chosen based on a uniform distribution that can take any value between 0° and 360°. Overall, 1×10^8 data samples are produced for training through random realization of different parameters (i.e., user location, device orientation, user direction, and noise) independently generated from each other. The transmitted and received symbols are collected as the training data. During the training stage, the DL model learns to minimize the error between the output of the neural network and the original transmitted data by re-adjusting the weights using a MSE loss function.

3.4.1 Learning Algorithm Design

Choosing a suitable size of training data set depends on the complexity of the system as well as the complexity of the learning algorithms. Using too little training data may cause poor performance since the model would be incapable of fully learning the diverse characteristics of the environment under study. Having too large training data may result in over-fitting, where the model corresponds too closely to the training data but fail to give good performance when new data is presented during the testing stage. Thus, we conduct several experiments to decide the suitable training data size and see which of them could offer the best BER performance. In this work, the DL model were trained on a computer with 2.3 GHz Quad-Core Intel i5 CPU taking between 0.6 to 1.5 hours to complete. It should be noted that one of the features of the indoor environment is that the furniture does not necessarily move every minute or every hour. Therefore, the indoor environment can remain unchanged for some period of time. In this case, training the deep learning methods based on a large set of channel realizations which consider random device orientations, random user locations, etc., is enough to help increase the generalization ability of the network. If the system changes over time (e.g., due to the placement of furniture at different locations), transfer learning can be used to update the deep learning network. For the system to adapt to new changes, we need to determine the part of systems that can be fixed and the part that needs to be fine-tuned. This can be considered as a future research direction.

Table 3.1 shows the effect of increasing the total number of training data for LSTM when the pilot ratio is 1/8 and 1/32, respectively. Considering the BER of 3.8×10^{-3} which is the forward error correction (FEC) threshold [131], we can see that increasing the training data size noticeably helps to reduce the SNR penalties against maximum likelihood when read at BER $= 3.8\times10^{-3}$. In order to decide on the number of layers to be used, several experiments were conducted by training different architecture complexities of the LSTM by varying the number of LSTM hidden layers. Table 3.2 shows the performance of LSTM with varying hidden layers. It is clear that by increasing the number of layers, LSTM works very well and perform close to ML. We can see that at BER $= 3.8 \times 10^{-3}$, the SNR penalty for 5 hidden layers compared to 10 hidden layers is almost 1 dB which is not a huge difference. Therefore, to avoid the risk of overfitting, 5 LSTM layers were chosen which gives good enough performance.

SNR penalty against ML (Full CSI) at BER $= 3.8 \times 10^{-3}$, (dB).			
Size of training data	3.4×10^8	8.5×10^8	1.7×10^9
LSTM with pilot ratio of 1/8	>10.0	1.9	0.9
LSTM with pilot ratio of 1/32	>10.0	4.0	1.0

Table 3.1: *The effect of the total number of training data when the pilot ratio is* $1/8$ *and* $1/32$.

SNR penalty against ML (Full CSI) at BER $= 3.8 \times 10^{-3}$, (dB).				
No. of hidden LSTM layers	3	5	7	10
SNR penalty (dB)	2.6	1	0.2	0.1

Table 3.2: *The effect of different number of hidden LSTM layers for full CSI with furniture.*

The hyperparameters (e.g., number of hidden layers, number of neurons, learning rate, etc.) are determined based on several experiments conducted using various configurations of the LSTM network. We manually search for the best value by trial and error (e.g., increasing and decreasing the number of hidden layers, the number of neurons, etc.). The number of neurons in each layer are adjusted to the complexity of the LiFi network where the number of neurons range is set to be between 5 to 100 neurons. The learning rate chosen for ADAM optimizer is 0.001, which gives a reasonable training time for the neural network. It is observed that the optimal performance can be achieved when our DL model consist of one input and one output layer, five hidden LSTM layers with 100, 50, 50, 25 and 10 neurons, respectively, one fully connected layer and one dropout layer. The LSTM layers process the whole input sequence using its feedback connections while the fully connected layer helps to map the output of the LSTM layer to the same size as the input layer. The dropout layer is added to help reduce overfitting and the model is trained until the validation loss stops decreasing or becomes larger than the previous minimum value. The high computational complexity of the proposed method is only during the training stage which is conducted offline. However, during the real-time implementation, the trained network is capable of offering a much faster solution.

3.4.2 Effect of Reduced Pilot Numbers

In order to show that our proposed method can give significant gains when partial CSI is considered, we compare the performance of our LSTM-based signal detection method, which for simplicity we call it LSTM, with the traditional LS estimation, and MMSE in terms of BERs

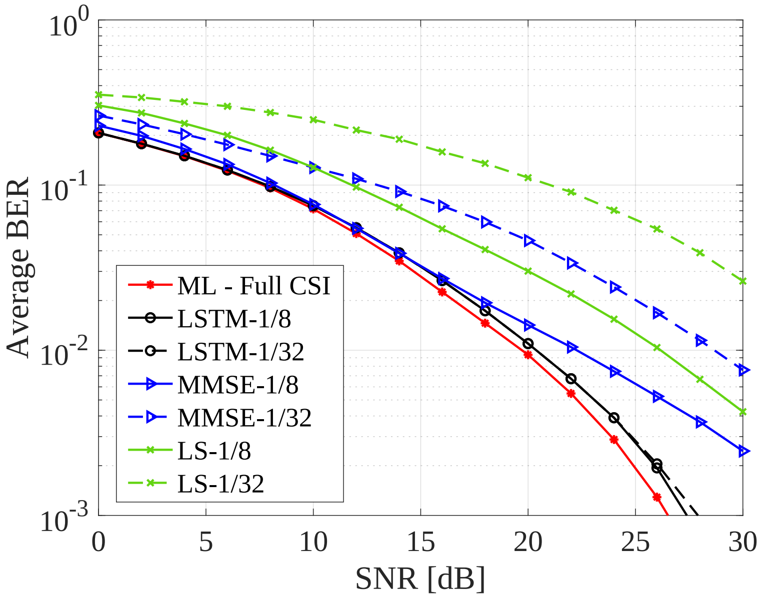

Figure 3.2: *The average BER versus SNR performance for different detection schemes when the pilot ratio is 1/8 and 1/32, assuming furniture is included in the room.*

for different SNRs. The simulation parameters are listed in Table 3.3. To test the accuracy of the DL network, we also implement ML detection as a benchmark which assumes perfect CSI. From the results depicted in Fig. 3.2, it is clear that the proposed model is proven to always achieve better performance than both LS and MMSE and can perform almost as good as the detection with full CSI. Our DL model offers excellent performance since it can adapt to the specific geometrical configurations and user behavior effects especially when fewer pilots were used. Focusing on the case where the pilot ratio is 1/32 and looking at BER $= 3.8 \times 10^{-3}$, an SNR gain of approximately 9 dB and 15 dB was obtained for LSTM-based approach compared to MMSE and LS, respectively. This can be expected as even when the number of pilots is reduced, the DL model has the ability to use the whole sequence of historical data to learn the channel characteristics and the user behavior effects and make reliable predictions of the transmitted signal. In comparison, LS and MMSE give poor performance since the reduced pilot number is not enough to accurately estimate the channel. Therefore, even when the system have partial channel information, the proposed model can still give excellent detection performance, that is similar to the detection with full CSI.

Parameter	Symbol	Value
Room dimension	$-$	$5\,\mathrm{m} \times 5\,\mathrm{m} \times 3\,\mathrm{m}$
LED half-intensity angle	$\Phi_{1/2}$	$60°$
Receiver FOV	Φ_c	$85°$
PD physical area	A	$1\,\mathrm{cm}^2$
PD responsivity	R_PD	1 A/W
Reflection coefficient	ρ	0.8
Transmit optical power	P_t	$1\,\mathrm{W}$
Number of subcarriers	$\mathcal{K}$	127

Table 3.3: *LiFi simulation parameters.*

Fig. 3.3 shows the MSE of the different detection schemes when the CSI is limited. From the figure, it can be seen that the MSE declines gradually with increasing SNR for all of the detection methods. It is clear that our LSTM-based detection scheme yields the best MSE performance for both full CSI and partial CSI scenarios. Once again, we can see that with partial CSI, LS gives the worst performance compared to LSTM and MMSE. This is expected as we know that LS does not take the channel statistics into account during channel estimation. Unlike LS, MMSE uses the first and second order of the channel statistics when performing channel estimation, which explains the better MSE performance obtained compared to LS.

3.4.3 Effect of Furniture

As previously mentioned in Section 3.1, in order to make the LiFi channel more realistic, we consider a very specific indoor scenario by including some furniture in the room as shown in Fig. 3.4. This figure shows the room configuration with different types of furniture (e.g., tables, chairs and cabinets) and the placement of APs when we consider multi-LED scenario in the later sections. The geometry of furniture and its locations are listed in Table 3.4.

To clearly see the effect it has on the performance of each methods, we compare their performance under two different scenarios; i) with furniture, ii) without furniture which can be seen in Fig. 3.5. We calculated the SNR penalties against ML for the performance of each detection schemes for the two different geometrical configurations (e.g., with and without furniture) which is shown in Table 3.5. We can see that without furniture, LSTM has a gain of 7 dB and 11 dB with respect to MMSE and LS. However, as also mentioned in the previous section, when

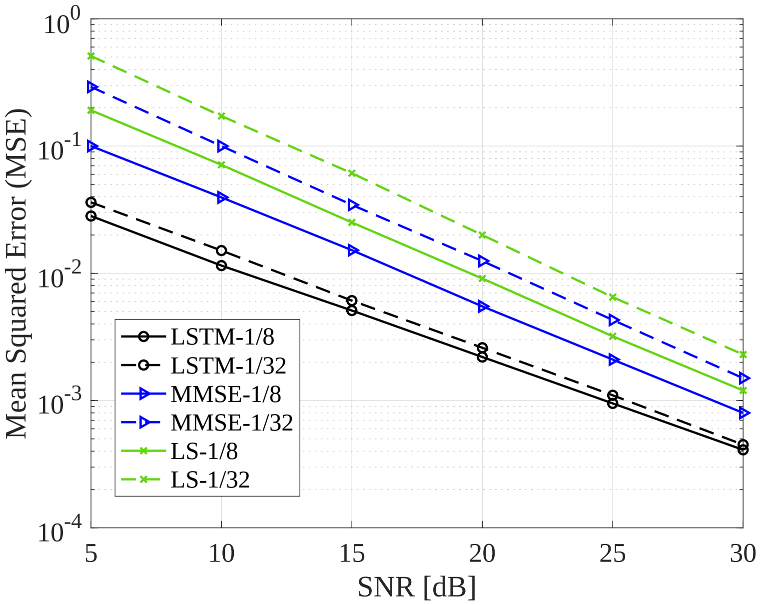

Figure 3.3: *MSE versus SNR performance for different detection schemes when the pilot ratio is 1/8 and 1/32, assuming furniture is included in the room.*

furniture is included in the room, LSTM performs very close to the respective ML with a gain of 9 dB and 15 dB compared to MMSE and LS, respectively to achieve BER $= 3.8 \times 10^{-3}$. This means that even when the geometrical configurations of the room changes, deep learning is able to capture those characteristics and outperforms the other traditional methods. By including furniture into the room, the blockage probability of the optical link increases, and the uniform scenario changes to become more specific. Therefore LS and MMSE perform worse in this case. These results prove our expectations of deep learning to learn the environment better than LS and MMSE when the geometry of the room becomes more complex by deviating from a symmetrical or uniform state. This conclusion is also confirmed in Table 3.5.

3.4.4 Effect of Conditional Hotspot Model

We further simulate the signal detection problem using the proposed method and train it based on a hotspot model. The idea of using a hotspot model is to see whether we can achieve higher gain in the DL method when the behavior of the user deviates from a uniform distribution thereby increasing the complexity of the environment. The hotspot model considers an area in the room

Figure 3.4: *Representation of the indoor environment when furniture are included.*

where the probability of the user being within this area is higher than being elsewhere. We collect the training data in a similar manner as the previous approach for all of the possible user locations. We then consider three types of scenarios where the probability of the user to be inside the hotspot area is 100%, 80% or 50%, namely Hotspot A, Hotspot B and Hotspot C, respectively. To realize this hotspot model, for each scenario, we train the LSTM network by using 100%, 80% and 50% of the total data collected from all possible locations of the user inside the hotspot area, respectively. For the second and third case, the balancing 20% and 50% of the data are taken from the random user positions located outside the hotspot area. We compare the performance between LSTM, MMSE and LS in the case where partial channel knowledge is considered. Fig. 3.6 presents the average BER curves for the three indoor scenarios where we remove LS performance to keep the figure less crowded. As expected, the best performance that is closest to the full CSI can be achieved by the learning-based scheme, especially when Hotspot A is considered. At BER $= 3.8 \times 10^{-3}$, there are gains of 9 dB, 7 dB and 6 dB for Hotspot A, Hotspot B and Hotspot C, respectively when comparing between LSTM and MMSE. Although the LSTM model would yield to a higher BER when the amount of training data based on the hotspot area is reduced, the model still provide good performance in comparison to MMSE.

Furniture type	Dimension, (width × length × height)	Location, (x, y, z)
Desk	90 cm × 180 cm × 70 cm	$(2.0, 1.6, -1.5)$
Table	120 cm × 120 cm × 70 cm	$(-0.9, 0.9, -1.5)$
Shelve	60 cm × 60 cm × 180 cm	$(2.2, -2.2, -1.5)$
Chair 1	40 cm × 40 cm × 40 cm	$(-0.9, 1.7, -1.5)$
Chair 2	40 cm × 40 cm × 40 cm	$(-0.1, 0.9, -1.5)$
Chair 3	40 cm × 40 cm × 40 cm	$(-0.9, 0.1, -1.5)$
Chair 4	40 cm × 40 cm × 40 cm	$(-1.7, 0.9, -1.5)$
Chair 5	40 cm × 40 cm × 40 cm	$(1.4, 1.6, -1.5)$

Table 3.4: *Furniture dimensions and positions*

SNR penalty against ML (Full CSI) at BER $= 3.8 \times 10^{-3}$, (dB).		
Method	Without Furniture	With Furniture
LSTM	0.3	0.9
MMSE	7.7	9.9
LS	11.6	16.4

Table 3.5: *The effect of furniture on the performance of different detection schemes assuming pilot ratio of 1/32 in terms of SNR penalty against ML with full CSI*

Hotspot A can be regarded as a fixed case where we are looking at a very specific scenario. Here the user is always sitting around the table in the hotspot area, rather than being randomly distributed within the room. Therefore, with this knowledge, it is easier for LSTM to learn and operate close to ML even with partial CSI. Hotspot B and Hotspot C cases can be viewed as random location scenarios, where the user can be anywhere in the room. For these random cases, the traditional methods benefit from more randomness and therefore gives better performance compared to Hotspot A. This is because the other 20% and 50% of the data are taken randomly and symmetrically outside the hotspot area, where there are parts of the room that has really good and really poor channels. The averaging effect eventually leads to LS and MMSE having improved BER performance. On the other hand, for Hotspot A, the channel gains are more highly influenced by the NLOS links which is a combination of many effects. This makes the frequency response of the system to be more complex and more difficult to estimate in the absence of full CSI particularly for LS and MMSE. Table 3.6 shows the effect of the different user behavior models to the performance of LSTM, MMSE and LS in the presence of partial CSI in terms of SNR penalty againts ML with full CSI. It can be seen that LSTM outperforms the other techniques by only having 1 dB to 2 dB SNR penalty against ML at BER $= 3.8 \times 10^{-3}$.

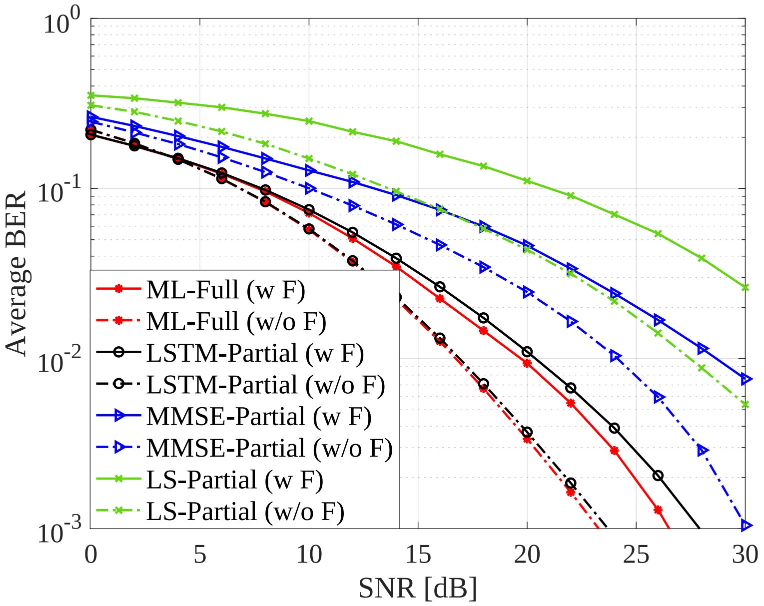

Figure 3.5: *The average BER versus SNR performance of different detection schemes under the effect of furniture and no furniture, assuming partial CSI with pilot ratio of 1/32.*

SNR penalty against ML (Full CSI) at BER $= 3.8 \times 10^{-3}$, (dB).			
Method	Hotspot A - 100%	Hotspot B - 80%	Hotspot C - 50%
LSTM	1.0	1.7	2.4
MMSE	9.9	9.0	8.7
LS	16.4	15.4	15.1

Table 3.6: *The effect of different user behavior on the performance of each detection methods with pilot ratio of 1/32 in terms of SNR penalty against ML with full CSI.*

Hence, from the result shown in Fig. 3.6 and in Table 3.6, we can confirm our earlier expectation that when different user behaviors exist, DL-based method should be able to capture and adapt to those specific characteristics of the channel and perform better compared to the traditional techniques.

3.4.5 Effect of Field of View and Multiple LEDs

In previous simulations, we have considered the FOV to be $85°$ and only a single LED is assumed. We now simulate two different cases in order to study the effect of FOV and multiple LED on the detection performance. Firstly, assuming partial CSI with furniture included in the

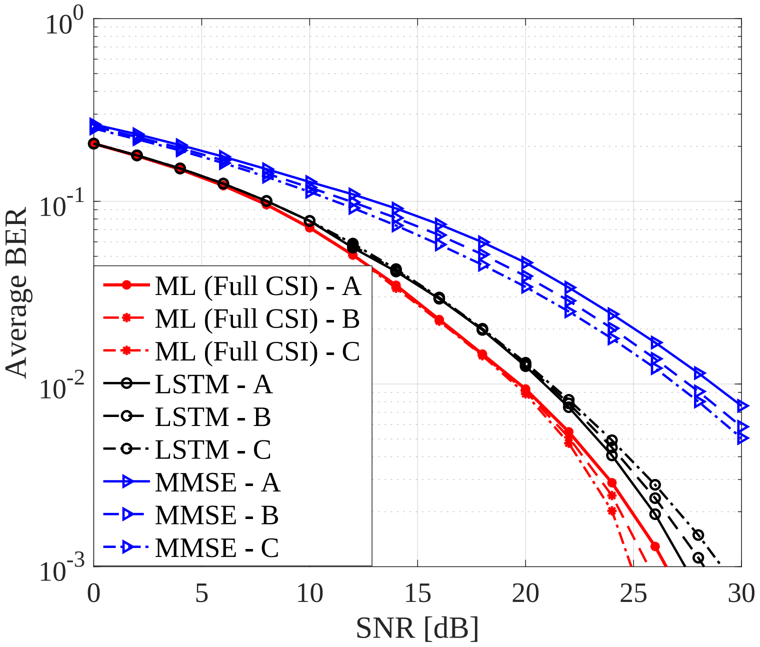

Figure 3.6: *The average BER versus SNR performance with different user behaviors based on conditional hotspot model where Hotspot A: 100%, Hotspot B: 80% and Hotspot C: 50% assuming partial CSI with pilot ratio of 1/32 and furniture is included in the room.*

room, we limit the value of the FOV to be $45°$. Fig. 3.7 show the performance comparison of different detection schemes between the two FOV values. It can be seen that when the FOV is reduced from $85°$ to $45°$, the performance of all detection methods degrades. However, LSTM shows that it is more robust to the effect of changing the FOV and can still give better detection performance compared to LS and MMSE. It is expected that the performance of detection methods degrades when compared to the case where the FOV value is $85°$. When setting the FOV to $45°$, the UE in some locations (e.g., users closer to the walls) may have no chance of accessing the AP as they may not see the LOS channel and there is less contribution of the NLOS channel.

Next, instead of focusing on a single LED, we investigate the effect of placing four LEDs on the ceiling as depicted in Fig. 3.4. For this particular scenario, we also assume partial CSI, furniture is included, and the FOV is fixed at the original value of $85°$. The LED half-intensity angle, $\Phi_{1/2}$ is set to be $35°$ which is chosen to fulfil the illumination requirements for an indoor environment [13]. Fig. 3.8 depicts the performance of each detection scheme when the effect

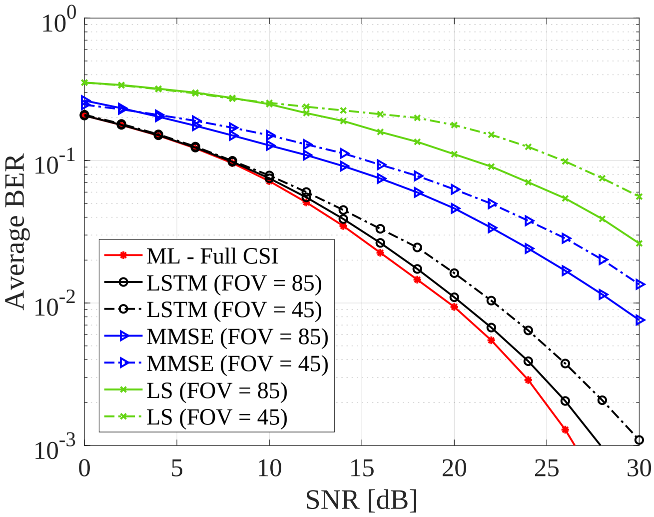

Figure 3.7: *The average BER versus SNR performance of different detection schemes with different FOV values, assuming partial CSI with pilot ratio of 1/32.*

of interference from the nearby APs is considered. From the result, it is shown that the added interference leads to no significant degradation in the average performance of LSTM as well as for MMSE and LS. Note that the average performance result shown does not consider any interference mitigation techniques such as fractional frequency reuse, which can also be applied to reduce the interference effect further particularly for the edge users.

3.4.6 Complexity Analysis

It has been mentioned in previous works that LSTM algorithm is very efficient and is local in space and time [100]. This means that the complexity of the network does not depend on the input sequence length and at each time step, the computational complexity of an LSTM layer per weight is $\mathcal{O}(1)$. Hence, the total complexity of an LSTM at each time step only depends on the number of weights which is $\mathcal{O}(w)$ where w is the number of weights. Therefore, the time complexity for our model is $\mathcal{O}(\sum_{l=1}^{d} w_l)$ where l and d are the index and the number of LSTM layers, respectively while w_l denotes the number of weights for the l-th layer. In our simulation, the LSTM model consist of 5 LSTM layers with 100, 50, 50, 25 and 10 hidden units, respectively. Note that the size of the training data samples exceeds the number of the neural network parameters, which means that the neural network will not overfit the data.

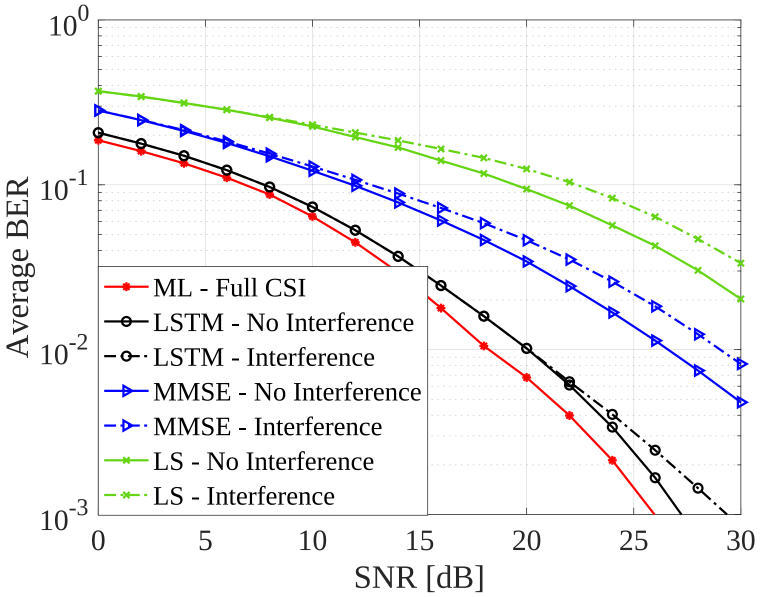

Figure 3.8: *The average BER versus SNR performance for multiple LED case, assuming partial CSI with pilot ratio of 1/32 and furniture is included in the room.*

It was mentioned earlier that channel estimation using LS requires low complexity and can be obtained by a simple division of the received pilot symbols under the effect of the optical channel over the transmitted pilot symbols. However channel estimation with LS gives inadequate performance as opposed to the DL techniques. LS channel estimation can be expressed as [28]:

$$\widehat{\mathbf{H}}_{\mathrm{LS}} = \left[\mathbf{Y}\left(p_1\right)/\mathbf{X}\left(p_1\right), \ldots, \mathbf{Y}\left(p_n\right)/\mathbf{X}\left(p_n\right), \mathbf{Y}\left(p_N\right)/\mathbf{X}\left(p_N\right)\right]^T, \tag{3.5}$$

where p_n is the n-th pilot index of the signal, $\mathrm{X}(p_n)$ is the transmitted pilot signal and $\mathrm{Y}(p_n)$ is the received pilot signal. Interpolation is then used to obtain the rest of the data subcarriers to get the full channel estimates. Assuming N is the total length of the pilot symbols, the complexity of LS can be described as $\mathcal{O}(N)$. Meanwhile, MMSE estimates the channel by minimizing the mean squared error. Unlike LS, it can provide better channel estimates as it utilizes the second order statistics of the channel. However, this results to an increase in complexity due to the inverse operations of the channel covariance matrix. MMSE can be expressed as [132]:

$$\widehat{\mathbf{H}}_{\mathrm{MMSE}} = R_{HH}\left(R_{HH} + \sigma^2\left(\mathbf{X}^H\mathbf{X}\right)^{-1}\right)^{-1}\widehat{\mathbf{H}}_{\mathrm{LS}}, \tag{3.6}$$

where $R_{HH} = \mathrm{E}[\mathbf{H}^H\mathbf{H}]$ is the channel covariance matrix in the frequency domain and σ^2 is the noise variance. The channel covariance matrix is calculated based on the statistical CSI across all subcarriers. Thus, the complexity of MMSE can be described as $\mathcal{O}(k^3)$, where k is the number of frequency subcarriers. Finally, ML detection is carried out by assuming the full knowledge of the CSI to provide a benchmark for optimal detection. Hence, due to the assumption of the availability of full CSI in this case, the complexity comparison would not be insightful.

3.5 Deep Learning-based Resource Allocation

The conventional resource allocation strategies in LiFi are usually iterative where the implementation complexity increases with the number of users. Most importantly, traditional resource allocation strategies require perfect CSI of all the users in the network, which is usually challenging to acquire in real-time, especially when we consider a high number of users. In multiuser systems, the users normally compete for resources. One of the popular scheduling technique namely proportional fair ensures efficient bandwidth allocation to users in order to support high utilization of resources while maintaining a level of fairness among the users [133]. However, PF scheduling algorithm requires full knowledge of the channel which may not be easily obtained in practice. Hence, motivated by the previous problem where accurate signal detection can be achieved using deep learning using only partial CSI, we propose a novel DFNN-based resource allocation scheme for multiuser LiFi systems.

We assume OFDMA based on DCO-OFDM in order to support multiple access between users. The signal transmissions for OFDMA are similar to what have been described in the detection problem. As the optimal benchmark, we simulate PF scheduling using full CSI. Considering H_j is the optical channel gain vector from the AP to the UE_j based on the realistic channel model proposed in the previous section, during the first round of scheduling, the user that has the maximum channel gain will be selected to connect to the AP. The PF scheduler then allocates a number of subcarriers to the UE_j based on the user's requested data rate and its link quality. The scheduler allocates the kth resources to jth UE following the metric defined as [17, 133]:

$$j = \arg\max_{j} \left(\frac{R_{\mathrm{req}}}{\bar{R}_j} \right), \tag{3.7}$$

where $\bar{R}_j$ is the average data rate of the jth UE before allocating the kth resource, and R_{req} is the requested data rate of the UE. In this work, we assume that the request data rate for all users are the same. After all of the resources has been allocated to all users, the downlink rate of UE$_j$ can be obtained using:

$$R_{\mathrm{d},j} = \frac{B_{\mathrm{d},n}}{\mathcal{K}} \sum_{k=1}^{\mathcal{K}/2-1} \log_2\left(1 + s_{j,k}\gamma_{\mathrm{d},j,k}\right), \tag{3.8}$$

where $s_{j,k} = 1$ if the kth subcarrier is allocated to the UE$_j$ and $s_{j,k} = 0$ otherwise. The SNR of the UE$_j$ on the kth subcarrier served by the AP, denoted as $\gamma_{\mathrm{d},j,k}$ can be described as:

$$\gamma_{\mathrm{d},j,k} = \frac{R_{\mathrm{PD}}^2 P_{\mathrm{t}}^2 H_{j,k}^2}{(\mathcal{K}-2)\eta^2\sigma_{j,k}^2}, \tag{3.9}$$

where R_{PD} is the PD responsivity, P_{t} is the transmitted optical power, $H_{j,k}$ is the channel gain on the kth subcarrier, $\mathcal{K}$ denotes the total number of subcarriers, η is the conversion factor, where we choose $\eta = 3$ to guarantee less than 1% of clipped signal. $\sigma_{j,k}$ is the noise power on the kth subcarrier of UE$_j$ expressed as:

$$\sigma_{j,k}^2 = \frac{N_0 B_{\mathrm{d}}}{\mathcal{K}}, \tag{3.10}$$

where N_0 is the noise power spectral density and B_{d} is the downlink bandwidth.

3.5.1 Learning Algorithm Design and Complexity Analysis

The PF algorithm takes in the channel gain data and outputs the user index of the allocated subcarriers. After all of the subcarriers have been successfully assigned to the users using PF scheduling technique, the channel realizations and the corresponding user allocation at each subcarrier are collected to be used as input and output training data, respectively. The user scheduling can be seen as a classification problem, where the channel gain is fed as input to the network, and the network then outputs the user index that has been allocated a subcarrier. As previously mentioned in Section II, the channel is assumed to be quasi-static where the resource allocation is performed over a single coherence time of the channel. Since the resource allocation problem does not really exploit the temporal memory of the channel, implementing LSTM will add unnecessary degrees of freedom, making the neural network design complex compared to a regular feed forward network. Hence, a feed forward network was chosen due to the state-free mapping from the input to the output. For this work, we consider a deep feedforward model which consist of an input layer, an output layer, and 7 hidden fully connected layers with 100, 50, 25, 20, 15, 10 and 5 neurons, respectively. The architecture of the DFNN network used for this problem can be seen in Fig. 2.9. The DFNN is trained based on the training data collected using the conventional PF user scheduling strategy. The trained network is later used in real-time implementation to efficiently conduct user scheduling based on the received input channel gains, with lower complexity. Same as the detection problem, the training for the network in resource allocation is conducted offline.

To analyse the performance of DFNN with different network architectures, we trained five DFNN models consisting of different numbers of hidden layers and compared their performance in terms of average throughput versus SNR. To test the accuracy of the trained networks, PF with full CSI is used as a benchmark. In Table 3.7, it appears that by increasing the number of layers of the network, DFNN can perform much better and even achieve very close performance to the PF scheduling. However, other than the issue of increased computational complexity when the number of layers are increased, it is also important to note that if the number of layers for the DFNN is too high, the network may overfit the training data, hence resulting in extremely good performance. As previously mentioned, overfitting occurs when the network corresponds too closely, or exactly to a particular set of data. Therefore, in order to avoid this problem, we have chosen to use 7 hidden layers which still gives good performance and is close enough to the performance of PF scheduling.

The online computational complexity of DFNN can be generally represented by the number of multiplications needed to compute the activation of all neurons in all of the network layers. The transition between the lth and $(l-1)$th layers requires $w_l \cdot w_{l-1}$ multiplications, where w_l are the weights at the lth layer and w_{l-1} are the weights at the previous layer. Therefore, the total complexity in DFNN network is given by $\mathcal{O}(\sum_{l=1}^{L} w_l)$, where L is the total number of layers. For PF scheduling, the major operation blocks consist of determining the average data rate at $\bar{R}_j$ and the metric j. Hence, its complexity can be described as $O(N_{\text{u}}k^2)$, where N_{u} is the total number of users and k is the number of subcarriers.

SNR penalty against PF (Full CSI) at target average throughput, R = 20 Mbps, (dB).					
No. of hidden layers	3	5	7	8	10
Value	7	3	0.6	0.3	0.2

Table 3.7: *The effect of different number of DFNN hidden layers on the performance of each user scheduling methods in terms of SNR penalty against PF with full CSI at a target average throughput of 20 Mbps.*

3.5.2 Effect of Reduced Pilot Numbers

Similar to the analysis in the OFDM signal detection problem, we compare the performance of our DFNN-based resource allocation scheme, which for simplicity we call it DFNN, with the traditional PF scheduling algorithm in terms of averaged throughput for different SNRs. Using the same simulation parameters as listed in Table 3.3, we consider an OFDMA system based on DCO-OFDM with the number of users, $N_\mathrm{u} = 4$ and the requested data rate, $R_\mathrm{req} = 20$ Mbps. To analyse the performance of the DFNN network, we set the PF scheduling technique which assumes perfect CSI as a benchmark. For the case of partial CSI, we apply PF scheduling which firstly estimates the channel based on LS and MMSE before moving on to the scheduling algorithm based on the estimated channel. We also compare two DFNN model which are trained based on full CSI and partial CSI. Fig. 3.9 show that the DFNN-based scheduling scheme for both scenarios (i.e., full and partial CSI) can achieve almost similar performance to the optimal PF scheduling technique which considers full channel knowledge. For the partial CSI case, it is clear that the DL method are proven to always achieve better performance compared to PF scheduling using LS and MMSE. We once again show that LS and MMSE based channel estimation give poorer performance when a realistic environment is considered. In contrast to PF scheduling with partial CSI, our DFNN model offers excellent performance since it has the ability to specifically adapt to the complex geometrical configurations and the user behavior effects. Hence, we can see a significant gain between the learning and non-learning techniques especially when fewer pilots were used.

Fig. 3.10 compares the MSE of the different scheduling schemes for the case of full CSI and partial CSI. Similar to the detection problem, the MSE declines gradually with increasing SNR for all of the scheduling schemes. It can be seen that the proposed DFNN-based scheduling scheme

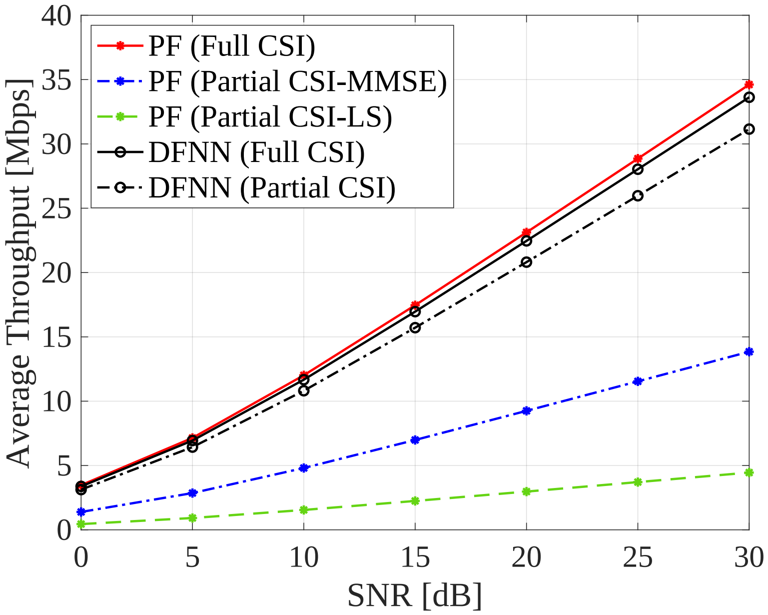

Figure 3.9: *Comparison between different scheduling schemes in terms of average throughput versus SNR for the case of full CSI and partial CSI with pilot ratio of 1/32, assuming furniture is included.*

provides the best MSE performance for both full CSI and partial CSI scenarios. As previously mentioned, we can expect that PF-LS gives the worst performance compared to DFNN and PF-MMSE when partial CSI is considered. This is due to LS not taking the channel statistics into account during channel estimation while MMSE uses the first and second order of the channel statistics.

Moreover, we compare the fairness among the users for the different scheduling algorithms to determine whether the users are receiving a fair share of the system resources. Many approaches to quantify fairness has been proposed in the literature with the most commonly used being Jain's fairness index. The user fairness index can be described as:

$$FI = \frac{\left(\sum_{j=1}^{N_\mathrm{u}} R_j\right)^2}{N_\mathrm{u} \sum_{j=1}^{N_\mathrm{u}} \left(R_j\right)^2}, \tag{3.11}$$

where N_u is the total number of users and R_j is the average throughput of user j. The value of the fairness index is 1 for the highest fairness when all users have the same throughput. The

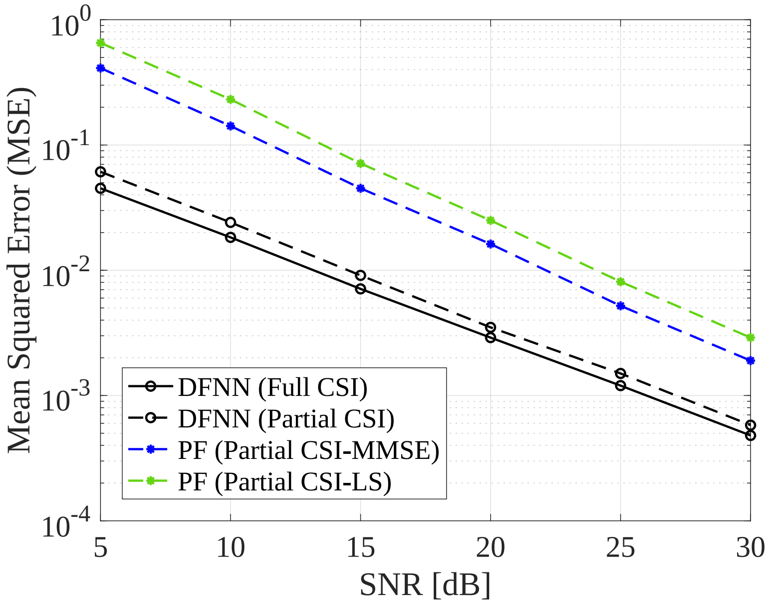

Figure 3.10: *MSE versus SNR performance for different scheduling schemes with full and partial CSI, assuming furniture is included in the room.*

N_u	PF-full	PF-LS	PF-MMSE	DFNN-full	DFNN-partial
4	1.0000	1.0000	1.0000	1.0000	0.9998

Table 3.8: *Fairness index among users for different user scheduling schemes.*

values of the Jain's fairness index for the users using different resource allocation schemes were calculated using (3.11) and are tabulated in Table 3.8. It is clear that most of the scheduling algorithms are able to achieve the fairness value of 1. For all of the PF schemes, the schedulers allocate the resources to the user who has the worst current channel realization relative to its own average. Hence, it guarantees an equal amount of resources for all users. The DFNN-based resource allocation scheme imitates the way PF allocates the subcarriers to users based on the given training data. Therefore it is also able to achieve fairness index value of 1 when full channel knowledge is available, or very close to 1 with partial CSI.

3.5.3 Effect of Furniture

In this subsection, we also compare the performance of the different scheduling schemes when we take into account the effect of furniture in the room. Similar to the detection problem, the

SNR penalty against PF (Full CSI) at target average throughput, R = 20 Mbps, (dB).		
Method	Without Furniture	With Furniture
DFNN	1.1	2
PF-MMSE	13.2	26.1
PF-LS	25.5	>50

Table 3.9: *The effect of furniture on the performance of each user scheduling methods with pilot ratio of 1/32 in terms of SNR penalty against PF with full CSI at a target average throughput of 20 Mbps.*

performance is compared between two different scenarios; i) with furniture, ii) without furniture where the result is shown in Fig. 3.11. The SNR penalties against the respective PF scheduling algorithm for each scheduling schemes are also tabulated in Table 3.9. In these results, we can see the same trend is happening as in the detection problem.

Looking at Fig. 3.11, assuming a target throughput of 20 Mbps, it is obvious that there is not a huge difference for DFNN-based method when we include the furniture. There is a 3 dB difference between DFNN with furniture and DFNN without furniture, and it can still operate close to the optimal PF scheduling. However, looking at the performance of PF based on LS and MMSE, there is quite a significant change when we include furniture in the room. As mentioned in the previous sections, the blockage probability of the optical link increases when furniture is included, and the room geometry becomes more specific and no longer symmetrical. In this case, PF-LS and PF-MMSE will perform worse compared to DFNN. The significant degradation in SNR for PF-LS scheme when furniture is included can also be explained due to the effect of user's fixed direction (i.e., the user is facing towards the table) at the area where the user is sitting, and since the LOS link from the AP is not strong enough at these locations, the LOS link can be easily blocked by the user itself. Therefore, it is clear that when furniture is added, PF-LS and PF-MMSE degrade substantially as it was the case in the signal detection problem. Once again our results show that deep learning-based system is able to perform better than the traditional methods when we consider specific geometrical configurations of the room that add complexity to the channel frequency response.

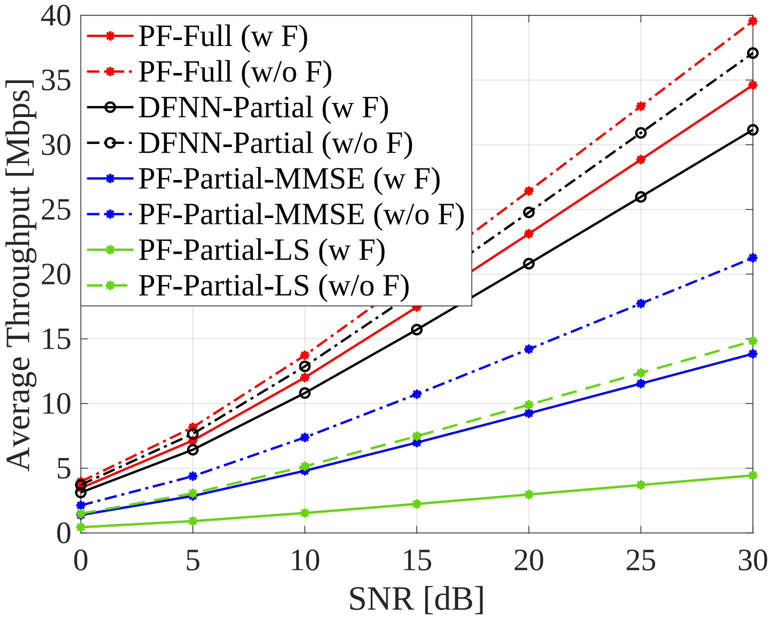

Figure 3.11: *The effect of furniture on the performance of different scheduling schemes in terms of average throughput versus SNR, assuming partial CSI with pilot ratio of 1/32.*

3.5.4 Effect of Conditional Hotspot Model

For this section, we applied the hotspot model for the proposed scheduling technique to see the effect of user behavior on the performance of our learning approach. As mentioned previously, the hotspot model considers an area within the room where users are most likely to be compared to other locations. We still consider three different user behavior scenarios where the probability of the user to be located within the hotspot area is 100%, 80% and 50%, and is referred to as Hotspot A, Hotspot B and Hotspot C, respectively. Focusing on the case with partial channel knowledge (i.e., having less pilot numbers), the performance is compared between our proposed DFNN technique and PF based on LS and MMSE. Fig. 3.12 shows the average throughput versus SNR curves for DFNN and PF-MMSE when different user behavior models are considered. These effects can also be seen in Table 3.10 where the performance is compared in terms of SNR penalty against PF with full CSI when we assume a target average throughput of 20 Mbps. Similar to the results in detection problem, we can see that DFNN is able to achieve the best performance even when the knowledge of user behavior decreases. It can also be seen that there is an increase in gain between the learning technique and PF with partial CSI when the

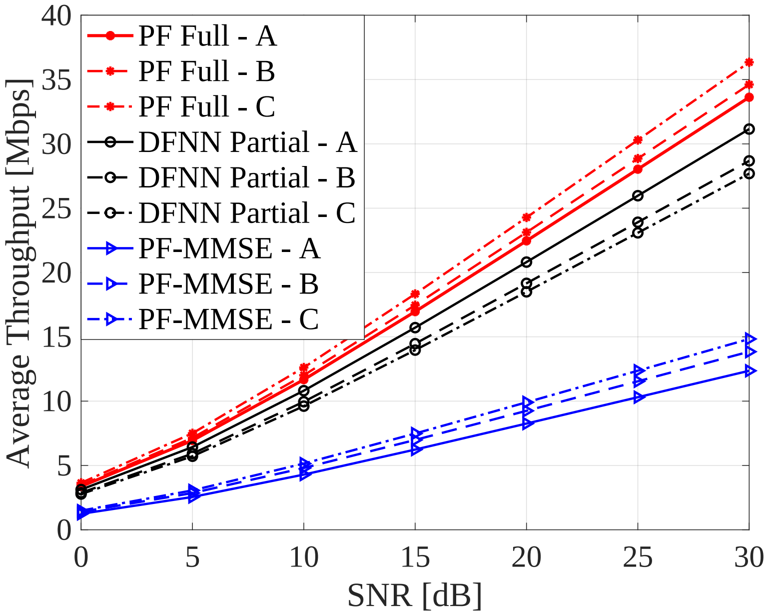

Figure 3.12: *The average throughput versus SNR performance for different user behaviors based on conditional hotspot model where Hotspot A: 100%, Hotspot B: 80% and Hotspot C: 50%, assuming partial CSI with pilot ratio of 1/32 and furniture included in the room.*

dependence to user behavior increases. Similar to the signal detection problem, it is expected that PF based on MMSE and LS estimation work well in a more random scenario where the performance is averaged over different channel conditions, which is why, for Hotspot B and Hotspot C, PF-MMSE and PF-LS provide better performance compared to when Hotspot A is considered. Meanwhile, for Hotspot A, we are looking at a very specific scenario in which the users are always around the table area. Since for this case MMSE and LS depends fully on the channels within the hotspot area, due to the nature of the light and furniture within the room, the channel is highly influenced by the NLOS links. Therefore, it may be challenging for MMSE and LS to estimate the channel accurately, which then leads to worse performance. Hence, this confirms the effectiveness and robustness of the learning method to adapt to different user behavior compared to the conventional techniques.

SNR penalty against PF (Full CSI) at target average throughput, R = 20 Mbps, (dB).			
Method	Hotspot A - 100%	Hotspot B - 80%	Hotspot C - 50%
DFNN	1.5	3.7	5.2
PF-MMSE	30.8	26.1	24.1

Table 3.10: *The effect of different user behavior on the performance of each user scheduling methods with pilot ratio of 1/32 in terms of SNR penalty against PF with full CSI.*

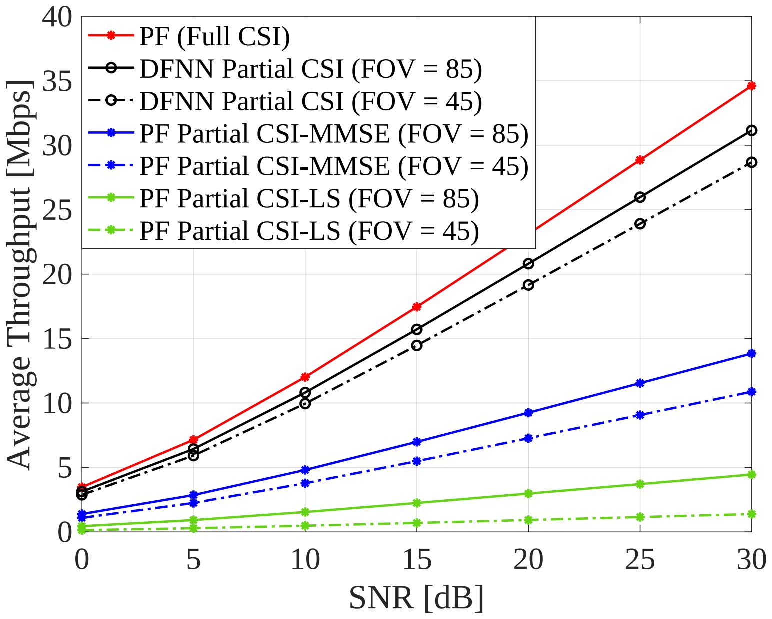

Figure 3.13: *The average throughput versus SNR between different scheduling methods with different FOV values, assuming partial CSI and with furniture.*

3.5.5 Effect of Field of View

We study the effect of limiting the FOV from 85° to 45° on the performance of each resource allocation schemes. Here, again, one AP provides coverage for the whole room so that the assumption of multiple users within a cell considered for the resource allocation problem is justified under the existing geometry of the room. As expected from the results of signal detection problem, Fig. 3.13 shows that when the FOV becomes smaller, the performance of all resource allocation schemes degrades while DFNN proves to be robust against FOV reduction achieving significantly better performance than PF-LS and PF-MMSE. As stated previously, due to the narrow FOV, the UE in some locations such as the users closer to the walls may not see the LOS channel and the contribution of the NLOS channel is smaller.

3.6 Summary

In this chapter, an indoor LiFi system with realistic channel model was considered by including the specific geometrical configurations and user behavior effects. With these channel models, two deep-learning based approaches were then introduced for improving the performance of signal detection and resource allocation. We compared the performance between the proposed learning methods and the conventional algorithms and demonstrated that the learning based schemes outperform the traditional methods as it has the ability to adapt to the specific changes in the environment and user behavior scenarios. Unlike the conventional techniques, the DL-based method has shown to give good performance even when there are irregularities in the system environment. By considering the channel as a black box, the proposed DL methods were able to indirectly estimate the channel and yield high gains in the performance of signal detection with an SNR gain of approximately 9 dB and 15 dB was obtained for LSTM-based approach compared to MMSE and LS, respectively, and resource allocation especially in the event of having partial CSI and with furniture taken into account. Simulation results showed that our DL models, with limited instantaneous knowledge of the channel, were able to perform almost similar to the optimal traditional techniques with perfect CSI. We also demonstrated the robustness of the learning based schemes in adapting to different user behavior scenarios by implementing user hotspot models. The simulated results confirm our expectation that DL-based schemes are able to operate better than traditional methods when specific indoor scenarios were considered with LSTM achieving SNR penalty of less than 2.5 dB against the optimal maximum likelihood estimation.

In the next chapters (e.g., Chapter 3 and Chapter 4), RIS is studied to improve the performance of a realistic indoor LiFi system under link blockage, user behaviour, random orientation, limited FOV, etc. RIS comprise of tunable reflecting elements to perform beamforming towards intended user locations. However, this concept requires complex operations in order to optimize the RIS elements configuration, which are mainly realized via wired control connections. Thus, based on the success application of deep learning in this chapter, it can be envisioned that deep learning methods can also be applied for efficient online wireless configuration of RIS when deployed in indoor communication environments. As a future research direction, the deep neural network can be trained to learn the mapping between the measured coordinate information at a user location and the optimal configuration of the RIS elements (e.g., the orientation of RIS units) which maximizes the user's received signal strength. Hence, during the online phase, the trained neural network will be fed with the measured position information at the target user to output the optimal orientations of the RIS elements for signal power focusing on this intended location.

Chapter 4
RIS Assisted OWC System Design and Outage Analysis

4.1 Introduction

It is noted that in most literature, the receiver is usually oriented vertically upwards and link blockage only covers the LOS obstruction by human bodies (either self-blockage or blockage by other users) [46–48, 110, 134, 135]. Hence, it is of paramount importance to incorporate all of these angular factors which contribute to blockage of the LOS path in order to provide a more realistic framework for the performance analysis of an indoor LiFi system. Recently, reconfigurable intelligent surfaces has gained interests due to its capability of modifying the wireless channel to improve the communication performance. Consequently, it has emerged as one of the most effective solutions to diminish the effect of blockage by providing alternative LOS paths when there exists an obstacle between the transmitter and receiver [49]. In LiFi, RIS usually comprises of a number of reflecting elements (e.g., mirror array) which can manipulate or reflect the incident light towards a desired location in order to gain high-power signal [49]. In the current literature, RIS has been shown to be very successful in many different applications of the wireless communication systems [105–107]. Hence, due to its interesting properties, it is worth to incorporate RIS into the realistic indoor OWC system and investigate the different designs of RIS that can best alleviate the joint blockage effect caused by the optical receiver's limited FOV, UE random orientation, self-body blockage and blockage by other external blockers (e.g., other users and furniture).

Blockage has been studied to a certain extent in the OWC domain. In [136], an interference mitigation technique for a multi-user indoor OWC was designed considering the impact of self-blockage and random human blockage. The results show that the effect blockage has on minimum throughput is more severe where blockage causes $40-50\%$ reductions in throughput.

In [137], a mechanism was developed to improve the blockage robustness for visible light communication networks. In this work, the users are guided by the network to rotate themselves for the improvement of the system performance as well as the individual user experience (e.g., by avoiding link blockage). The simulation and experimental results demonstrate that the proposed method can improve the system throughput by 46% and user fairness by 15%. However, it was noted that only self-blockage was considered and it was assumed that the receiver is always facing towards the ceiling. Blockage effects caused by the human body and random orientation has been considered in [138] where the authors presented a transmitter assignment scheme to alleviate these issues. It was shown in the simulation results that the proposed scheme could significantly decrease the outage probability and improve quality of service of the LiFi system under the effect of blockage and random receiver orientation. In [139], analytical expressions for uplink OWC channels were derived under the influence of link blockage and random device orientation considering a single static user and the results show that the effects of random orientation and link blockage lead to a decrease in coverage probability by $10 - 40\%$ with various SNR thresholds. Furthermore, the performance analysis of indoor VLC system under the impact of static and mobile human blockages were also studied in [140] and in [141]. In [140], it was demonstrated that at a lower density of human blockages in the room, the 4-LED configuration outperforms the 8-LED configuration. However, at a higher density of human blockages, the 8-LED configuration outperforms the 4-LED configuration for the same total power constraint.

As previously mentioned, the requirement of direct LOS link between the transmitter and receiver remains a key limiting factor in the OWC systems. Additionally, the random orientation of the UE, the limited receiver's FOV as well as blockage by the human bodies also affects the existence and quality of the LOS channel. Hence, it is necessary for LiFi to use a different technology such as RIS to solve these issues. Several studies have been made on the use of RIS in VLC systems including [108, 142–145], however, most of these studies except from [145] have made a simplified assumption that the UE is facing upwards towards the ceiling and therefore the impact of random orientation of the user device were not considered. From the literature, it has been proven that the use of RIS can enhance key performance indicators such as achievable data rate, energy efficiency, spectral efficiency and secrecy rate [54, 146–149]. In this work, we analyse the different designs of RIS to improve the network performance in terms of outage probability while considering the important factors contributing to the blockage of LOS path between the transmitter and the receiver.

In this chapter, the effects of the LOS optical link blockage on the outage performance of a LiFi network is studied considering different indoor scenarios and efficient RIS-based solutions, capable of diminishing the blockage effect is proposed. The performance analysis take into account the crucial blocking factors such as the limited FOV of the user device, random device orientation, user's self blockage, and blockage by other blockers as well as the user's distribution. The main contributions of this work can be summarized as follows. We propose an efficient channel acquisition method for the RIS-assisted indoor OWC system which relies on the geometry of the RIS elements and the structural information of the optical channels. More specifically, the user's location is estimated based on the received signal strength between the RIS elements and the different locations of the room. This method offers a much lower computational complexity as it significantly reduces the dimension of the decision variables required for RIS-based channel acquisition. We then investigate several RIS attributes such as shape, size, height and distribution on the performance of a single source LiFi system under the influence of blockage by the receiver's limited FOV, UE random orientation and user's self blockage. We show that these attributes play important roles in increasing the network performance in terms of outage probability. Finally, we provide numerical-based performance analysis for an RIS-aided realistic indoor LiFi network with multiple source and extend the analysis by also considering the blockage effects by other fixed and random blockers (e.g., blockage by other users and furniture). We show how the incorporation of furniture into the geometry of the room will also influence the user distribution (e.g., hotspot) which increases the complexity of the system.

The remainder of this chapter is organized as follows. Section 4.2 describes the considered indoor LiFi environment, the definition of outage probability and the considered hotspot model. The channel acquisition algorithm for RIS-aided systems are explained in Section 4.3. Furthermore, the optimization of RIS design is shown in Section 4.4. Section 4.5 discusses the performance analysis of a RIS-aided realistic indoor LiFi network. Finally, this work is concluded in Section 4.6.

Parameter	**Value**	**Parameter**	**Value**
Receiver FOV	60°	Reflection coefficient (wall)	0.6
Body shadowing angle	67.38°	Reflection coefficient (ceiling)	0.8
User body width	0.4 m	Reflection coefficient (floor)	0.2
Horizonal distance of UE to user	0.3 m	Reflection coefficient (RIS)	1.0
User body height (standing)	1.7 m	Height difference of UE to user (standing)	0.6 m
User body height (sitting)	1.15 m	Height difference of UE to user (sitting)	0.3 m

Table 4.1: *List of simulation parameters*

4.2 RIS-Aided System Model

A setup of an indoor LiFi room environment of size 5 m × 5 m × 3 m is considered, initially with one AP and one user to investigate the impact of different RIS designs on the indoor LiFi system. In this simulation, the combination of direct LOS channel gain between the AP and the UE, the NLOS channel gains contributed from the surface of the room (e.g., walls, ceiling and floor) and reflections from the RIS elements, as well as other effects such as the random orientation of the UE and blockage by the user body as described in Chapter 2 are considered. Note that in order to limit the computational complexity, we focus only on the first-order reflections of NLOS and RIS. The considered receiver's field of view is 60°. The simulation parameters for this section are chosen and summarised in Table 4.1. For this set up, the RIS designs are varied in terms of height, size, shape and total number of elements and we compare their performance in terms of outage probability. In the later sections, we extend the study by considering multiple APs and a realistic indoor environment with the inclusion of furniture, blockage effects by other users and non-uniform distribution of users based on a hotspot model.

4.2.1 Definition of Outage Probability

In this chapter, outage probability is used as the main metric for the performance analysis. We define the outage probability at a user's location with coordinate L_u, denoted by $\mathcal{P}_\mathrm{out}(L_\mathrm{u})$, as the probability that the instantaneous SNR of the receiver falling below a threshold value of the required SNR. Mathematically, it is formulated as:

$$\mathcal{P}_\mathrm{out}(L_\mathrm{u}) = \mathrm{P}(\mathrm{SNR} \leq \mathrm{SNR}_\mathrm{Th}), \tag{4.1}$$

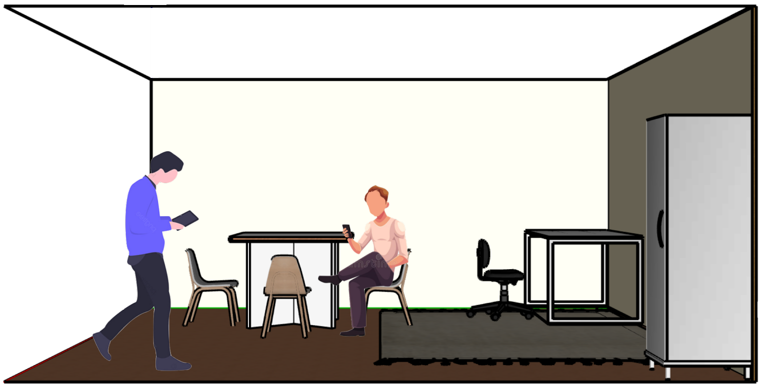

Figure 4.1: *Illustration of the room with furniture.*

where the received electrical SNR can be acquired as:

$$\mathrm{SNR} = \frac{(R_{\mathrm{PD}} H_{\mathrm{ow}} P_{\mathrm{t}})^2}{N_0 B_{\mathrm{d}}}, \tag{4.2}$$

and $\mathrm{SNR}_{\mathrm{Th}}$ denotes the SNR threshold value while $\mathrm{P}(.)$ denotes the probability. Note that in this chapter, H_{ow} is the combination of the LOS links and first-order reflections of the NLOS and RIS links and under the influence of link blockage. The outage probability across all receiver's locations can therefore be calculated as:

$$\overline{\mathcal{P}}_{\mathrm{out}} = \mathrm{E}[\mathcal{P}_{\mathrm{out}}(L_{\mathrm{u}})]. \tag{4.3}$$

4.2.2 Hotspot Model

The idea to model a hotspot in this chapter is to analyse blockage when the behavior of the user deviates from a uniform distribution. The hotspot model considers a certain area in the room where the probability of the user location being within this area is higher than being outside of this area. Therefore, to realise this model, we consider an indoor environment with typical furniture included (e.g., working desk, table, chairs and cupboard) with fixed positions in the room as depicted in Fig. 4.1. We consider the hotspot area to cover the locations where the tables and chairs are placed. It is assumed that for a number of realizations, the probability that the users are sitting on the chairs with fixed user directions (i.e., the user is facing towards the table) is higher than the probability of the standing users at other locations in the room with random user directions (i.e., the user could be facing towards any direction). Hence, we define λ and $(1-\lambda)$ as the factors determining the probability of the users distribution for sitting and standing, respectively, in the room. We can then define the outage probability based on the hotspot model as:

$$\overline{\mathcal{P}}_{\text{out}} = \lambda\overline{\mathcal{P}}_{\text{sit}} + (1-\lambda)\overline{\mathcal{P}}_{\text{stand}}, \tag{4.4}$$

where $\overline{\mathcal{P}}_{\text{sit}}$ and $\overline{\mathcal{P}}_{\text{stand}}$ denotes the average outage probability of the sitting and standing locations, respectively.

4.3 RIS-aided Channel State Information (CSI) Acquisition

As discussed in the previous sections, one of the fundamental challenges in indoor LiFi systems is the susceptibility to blockage effects and a way to alleviate these effects is to use RIS to reconfigure the optical channel propagation. However, due to the large number of RIS elements, the channel acquisition can be a challenging problem. Majority of studies assume perfect CSI availability to avoid huge pilot overhead when implementing RIS systems with massive number of elements. It is also worth mentioning that if the UE is mobile, the time-varying location of the UE makes it crucial to learn the channel within a short time interval. Therefore, as a possible solution to this problem, we propose a low complexity CSI acquisition method for RIS-aided LiFi network which significantly reduces the dimension of the optimization variables required to provide beam-forming towards a specific user's location. To the best of our knowledge, this is the first low-complexity CSI acquisition method for an RIS-aided LiFi network.

Despite the large number of RIS reflecting elements, the channel between the RIS and the AP/UE in an indoor environment has a unique geometrical structure that can be exploited during channel acquisition. The key idea of our CSI acquisition method is to segment the receiver plane to a 2D grid (see Fig. 4.2a) with N individual squares where each square can be illuminated by the beam spot reflected from a single RIS element. Let A_r be the area of the squares of the 2D grid, which is determined by the size of the smallest beam spot generated by an RIS element on the receiver plane. The grid square where the user is located can be then identified through a number of channel measurement steps during which the problem is exponentially reduced in size. Firstly, assuming that RIS with a total number of M elements are placed across different

Algorithm 1 Proposed CSI Acquisition Method

```
Initialization: Denote $M$ as the total number of RIS elements; $\mathcal{T}$ and $A_{\mathcal{T}}$ denote the current target section of the room where the user is estimated to be located and its area respectively; $A_\mathrm{r}$ as the area of the reflected beam spot from a single RIS element; $L_\mathrm{a} = (x_\mathrm{a}, y_\mathrm{a}, z_\mathrm{a})$ as the location of the AP; $L_n = (x_n, y_n, z_n)$ as the location of the $n$-th RIS element; $\hat{L}_\mathrm{u} = (x_\mathrm{u}, y_\mathrm{u}, z_\mathrm{u})$ as the estimated location of the UE;
The initial target area, $\mathcal{T}$, is assumed to be the whole room.
while $A_{\mathcal{T}} > A_\mathrm{r}$ do
    Segment the target area, $\mathcal{T}$, into a grid of $2 \times 2$ subareas, namely $\mathcal{T}_1$, $\mathcal{T}_2$, $\mathcal{T}_3$, and $\mathcal{T}_4$.
    Calculate the number of beam spots required to cover each subarea $\mathcal{T}_i$ as $\mathcal{N} = A_{\mathcal{T}}/4/A_\mathrm{r}$
    for $i = 1 : 4$ do
        for $j = 1 : \mathcal{N}$ do
            Choose a $\lfloor M/\mathcal{N} \rfloor$ subset of optimally oriented RIS elements that collaboratively illuminate spot $j$ of subarea $\mathcal{T}_i$. The optimal orientation of RIS elements are read from the pre-computed look-up table.
        end for
        Measure the received signal strength as $S(i)$.
    end for
    $i_\mathrm{max} = \mathrm{argmax}[S(1), S(2), S(3), S(4)]$
    $\mathcal{T} = \mathcal{T}_{i_\mathrm{max}}$
end while
Return coordinates of the center of the current target area $\mathcal{T}$ and assign as the estimated position of the UE, $\hat{L}_\mathrm{u} = (x_\mathrm{u}, y_\mathrm{u}, z_\mathrm{u})$
Return the optimal orientations of RIS elements to illuminate $\mathcal{T}$ from the look-up table.
```

walls of the room, the whole room is considered as the target area for user location denoted by $\mathcal{T}$. In each step, we segment the target area into a grid of 2×2, illuminate each of the 4 subarea sequentially and determine the new target area of the quarter of the original size by identifying the maximum received power out of 4 channel measurements across the subareas. This way, the size of the target area exponentially decreases in some steps from the whole room to A_r, which can be illuminated by a single IRS element.

Considering the target area $\mathcal{T}$ with area $A_{\mathcal{T}}$, there is $\mathcal{N} = A_{\mathcal{T}}/4/A_\mathrm{r}$ squares to illuminate in each subarea. Therefore, to illuminate each grid square covering the subareas on the receiver

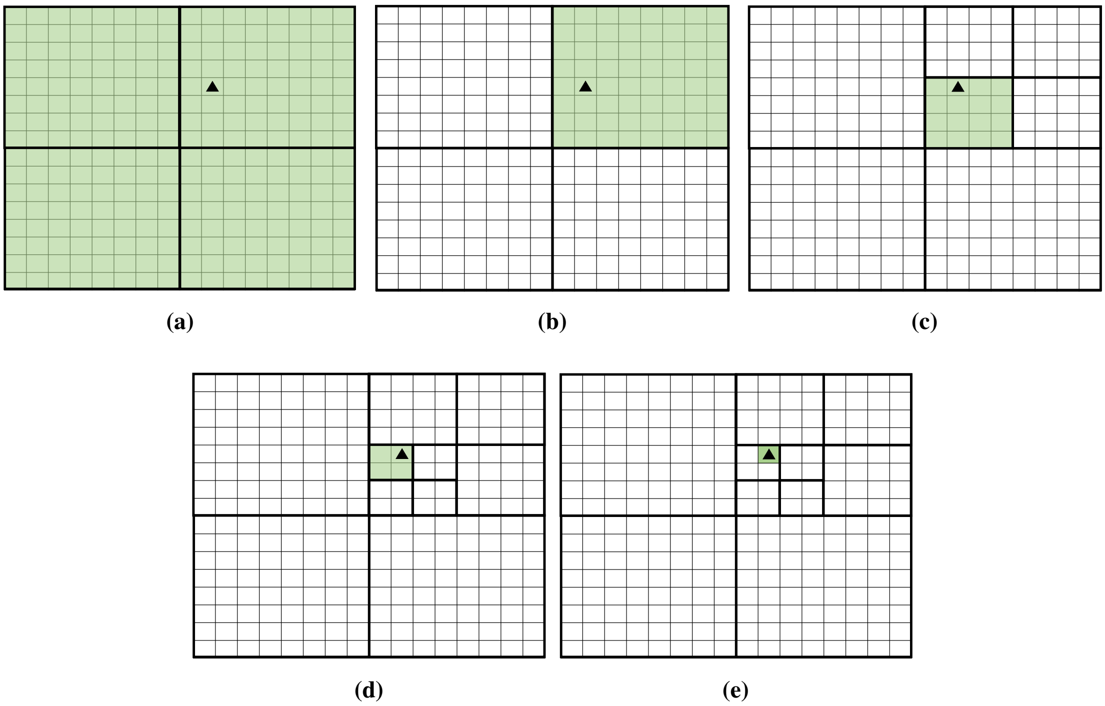

Figure 4.2: *Stages of finding the optimal location of the UE based on Algorithm 1. The grid illustrates the receiver's plane in 2D where the green colour shows the target area at each iteration and the symbol ▲ denotes the actual location of the UE. The whole room initially considered as the target area where the UE could be located as shown in (a). Then, the target area is reduced by 1/4 at each step as in (b),(c) and (d). At the final step, the estimated location of the UE is determined as seen in (e)*

plane, a subset of $\lfloor M/\mathcal{N} \rfloor$ optimally oriented RIS elements from different walls is chosen. Note that the respective RIS elements and their optimal orientations can be retrieved from a pre-computed look-up table, which uses the geometry of the room including the locations of the AP, RIS elements, and the grid squares in the receiver plane to calculate the optimal orientation of each RIS element and to estimate their reflected light level on each square. The low-complexity CSI acquisition method can be summarized in Algorithm 1.

Considering Fig. 4.2, where the room is covered by a 2D grid of $N = 256$ squares, Algorithm 1 first segments the receiver's plane into four large subareas as shown in Fig. 4.2a and calculates the number of beam spots that is required to cover each subarea as $\mathcal{N} = 64$. Next, for each square, the RIS elements from each wall are chosen to be optimally oriented towards the different

Scheme	Dimension of optimization variables
Conventional	$k^2 \times M$
RSF	N
Proposed	$2\log_2 N$

Table 4.2: *Comparison between the number of decision variables for different schemes.*

spots in the target area and their optimal orientation is taken from a look-up table. For example, for $M = 256$, 4 RIS elements are selected to illuminate each square in order for M RIS elements to collectively cover the whole considered area and then the received signal strength is measured by the user. This step is repeated for the rest of the segmented subareas and by comparing the received signal strength between the four subareas, the algorithm selects the area with the maximum signal strength as illustrated in Fig. 4.2b as the new target area for the user location. Then, as long as the size of the target area, A_T is bigger than A_{r}, the algorithm continues to segment the target area into another four smaller grids and repeats the process as depicted in Fig. 4.2c, 4.2d, and 4.2e until finally the size of the target area is approximately the same size as the reflected beam spot from a single RIS element (i.e., this means that one RIS element is enough to cover the target area) as shown in Fig. 4.2e. The final target section is then considered as the optimal estimation of user location based on which the optimal orientation of each RIS element is determined to reflect the light towards the user. Note that the proposed CSI acquisition methods still requires feedback from the UE to indicate the strength of the signal which can be transmitted using pilots. Based on this example, it is important to mention that the proposed method only requires 16 pilot symbols to be transmitted across the four steps to estimate the location of the user which significantly reduces the complexity of the CSI acquisition process compared to the conventional methods.

The complexity of the conventional channel acquisition technique often used in the literature [145, 150–153] depends on the dynamic range of the two dimensional orientation angle of the RIS elements. Hence, the number of optimisation variables would increase proportionally to the number of RIS elements due to the requirement of finding the optimal combination of the orientation angles. To reduce the high dimensional problem of the CSI acquisition, a reflected spot finding (RSF) scheme has been proposed in [144]. In their study, it was assumed that the combination of the RIS orientation angles has a one-to-one correspondence to the position of the reflected spot in the received plane. Therefore, instead of optimizing two angles of orientation for each RIS element, the RSF method finds the optimal position of the reflected spot which makes the optimization problem to only depend on the grid size considered in their environment, i.e., N. In comparison to the method introduced in [144], our method is able to further reduce the dimension of the decision variables as the proposed algorithm can exponentially reduce the size of the target areas that estimate the location of the user in iterative steps. Therefore, the number of measurement steps to converge to the user location would reduce to $\log_2\sqrt{N}$, while four measurements are conducted per step making the total number of measurements to be $4\log_2\sqrt{N} = 2\log_2 N$. The comparison between the complexity of our method with the CSI acquisition techniques proposed in the literature can be found in Table 4.2, where k denotes the degrees of freedom of each orientation angle of the RIS elements. The table shows the dimension of the optimization variables, which is equivalent to the number of pilot signals that needs to be transmitted for channel measurement in each scheme.

4.4 RIS Layout Optimization

In this subsection, we investigate the effect of different RIS layouts on the performance of a single AP LiFi system. In particular, we vary the RIS height, elements size, shape, number of elements, and its distribution on the walls (i.e., RIS is either placed on one wall or four walls). In order to limit the complexity of analysis, only first order reflection of RIS and NLOS links are considered. Note that in this chapter, the main focus is to show the gain of implementing RIS in indoor LiFi system in order to alleviate the effect of link blockage and improve the outage performance. Thus, we assume that the RIS elements are optimally oriented towards the target users and provide 100% reflection using mirror arrays. The optimization of optimal configuration of RIS elements (e.g., finding the optimal orientation of the mirror arrays) owing to the ”intelligence” of RIS can be considered as a future research direction.

4.4.1 Impact of RIS Height

We first determine the optimal RIS layout by investigating the different height placements of the RIS, its size and shape to see which design would maximize the average channel gain for the

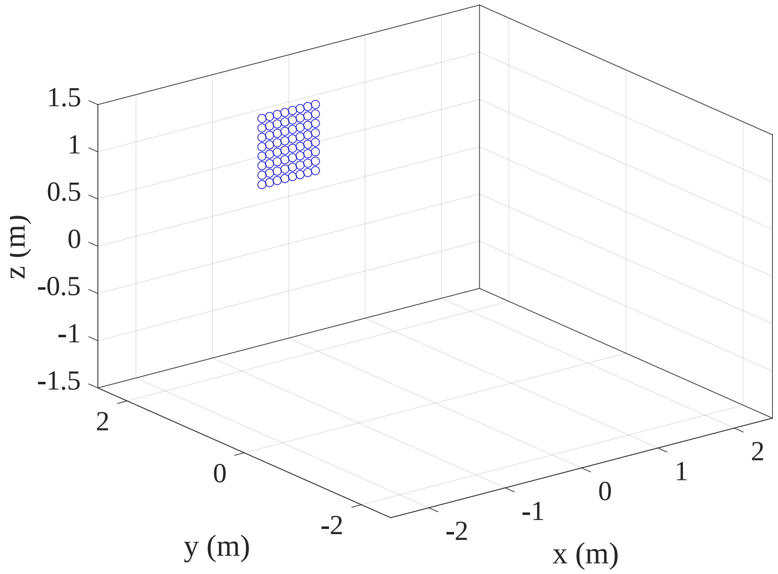

Figure 4.3: *Room geometry with RIS of 64 elements placed on one wall where the height of its center element is the midpoint between the height of UE and the ceiling.*

whole room. Fig. 4.3 shows the room geometry with square shaped RIS of 64 elements where it is assumed that each of the RIS elements are of size 10 cm × 10 cm. In order to determine the optimal height of the RIS placement, we calculate the average channel gain for different rows of RIS starting from the bottom row (e.g., row index $= 1$) going towards the top row of RIS (e.g., row index $= 8$). Note that the channel gain is only from the contribution from the reflection of RIS elements and excluding the contributions of direct LOS from the AP and NLOS reflections from the walls. From Fig. 4.4, it can be seen that the channel gain improves as the height of the RIS elements are increased. This is expected as the higher the RIS is positioned, the higher the chance for the UE to receive the reflected link from the RIS due to the limited FOV of the UE as well as the effect of the random device orientation. However, it is noted that after a certain height (e.g., sixth row), the channel gain decreases (e.g., seventh and eighth row), indicating that placing the RIS higher on the walls does not necessarily mean that it will give the best performance compared to lower heights, and that there is an optimal height placement for the RIS elements that needs to be determined. Again, this may be due to the effect of the UE's field of view, random orientations and self-blockage at the user locations near the RIS. For these locations, as the height difference between the RIS and the UE becomes too large, the channel gain may become smaller. From Fig. 4.4, it seems that the RIS elements placed at row 6

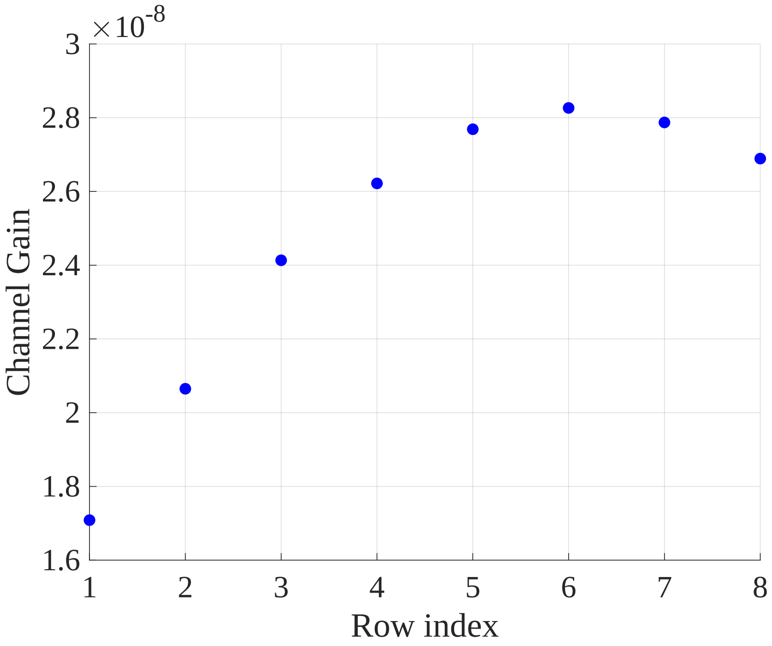

Figure 4.4: *Average channel gain for different RIS rows across all locations in the room.*

provides the maximum channel gain, while row 7 gives the second-best channel gain compared to the other rows. Therefore, it is clear that the optimal height placement for the RIS elements are at row 6.

4.4.2 Impact of RIS Size

Since the optimal height of RIS placement has been determined, we now investigate the suitable size for one RIS element that would provide accurate outage probability performance. In the previous section, we assumed RIS elements of size $10\,\mathrm{cm} \times 10\,\mathrm{cm}$ and thus in this section, we increase the size of each RIS elements to analyse the impact it has on the outage probability performance. To limit the simulation complexity, in this analysis we only assume one user location which is situated at the corner of the room. The comparison in outage probability performance with increasing transmit power between different RIS sizes is depicted in Fig. 4.5. It is seen in the result that increasing the size of the RIS elements would only lead to inaccurate outage probability performance. However, decreasing the size of RIS elements yields to a more accurate outage probability performance. This effect can be clearly seen for RIS of size $50\,\mathrm{cm} \times$

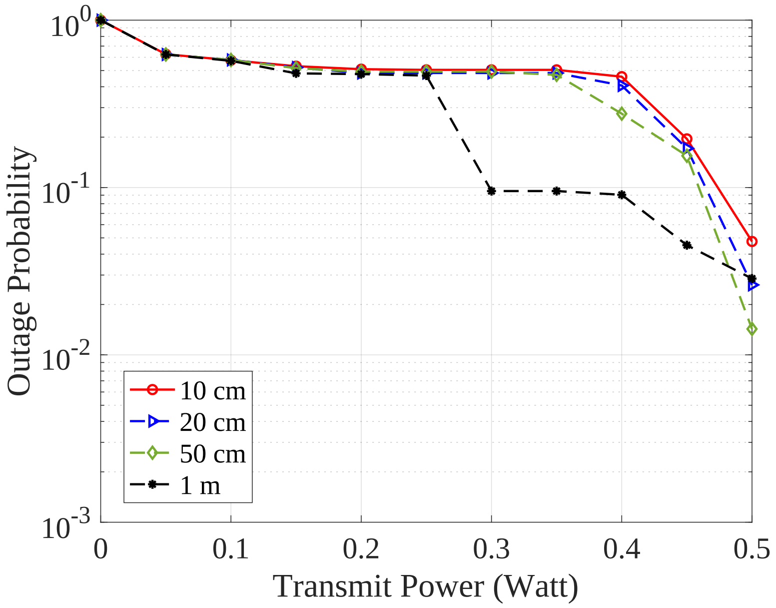

Figure 4.5: *Comparison of outage probability between different RIS elements size for one user location.*

50 cm and 20 cm × 20 cm, where the outage probability curves almost come to a merge with RIS of size 10 cm × 10 cm with increasing transmit power. This can be explained due to the fact that with larger size of RIS elements, there are fewer number of elements that can be considered on the wall. Thus, when there are less number of RIS elements, the coverage area on the receiver's plane by the RIS elements also decreases (i.e., the RIS elements are directed towards only certain parts of the room and does not cover all possible user locations). For smaller RIS size (e.g., 10 cm × 10 cm), there are more number of elements that can fit on the wall where each of the elements are directed towards different parts of the room and therefore able to provide larger coverage area. Although in Fig. 4.5 it is shown that RIS of size 10 cm × 10 cm yields a high outage probability performance whereas the desired outage probability would be below 10^{-2}, reducing the RIS size even further would only increase the computational complexity while the gain in terms of outage probability will not be as significant. Furthermore, this result can serve as a benchmark for the most basic scenario (e.g., square shaped RIS placed on only one wall) where in the next sections of this chapter, we try to reduce the outage probability even further by changing the shape of RIS, its distribution on different walls and the number of RIS elements. Hence, for the rest of this work we continue to assume the size of 10 cm × 10 cm for the RIS

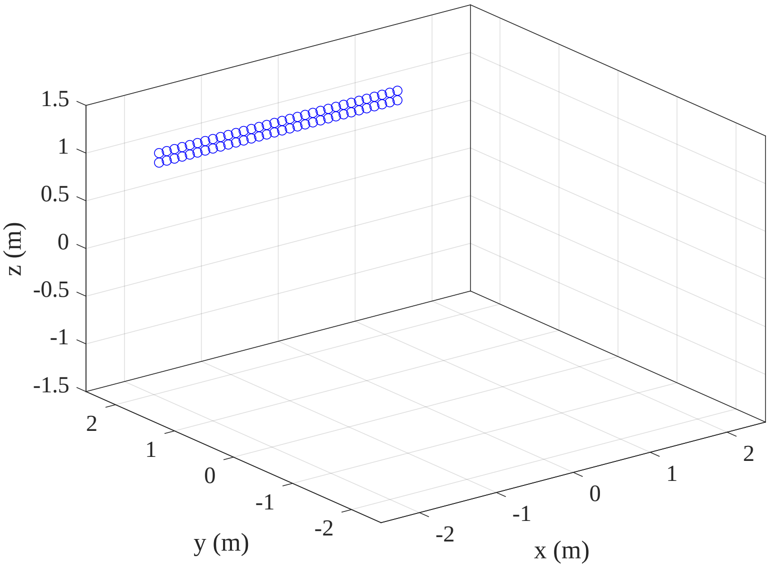

Figure 4.6: *RIS of 64 elements placed on one wall with a rectangular shape design. The RIS elements are arranged in two rows based on the previously determined optimal height (e.g., row 6 and row 7 in Fig. 4.4)*

elements.

4.4.3 Impact of RIS Shape

Next, we change the shape of the RIS from square shaped to rectangular shaped such that the RIS consists of only two rows and the elements are placed based on the optimal height of the RIS (e.g., at row 6 and row 7 in Fig. 4.3) as shown in Fig. 4.6. In the next results, we compare the outage probability performance between the different RIS shapes and heights. Fig.4.7 depicts the outage probability for the whole room when a total of $M = 64$ elements are placed on one wall. The performance of RIS-assisted communication system is compared between having square shaped and rectangle shaped with two rows of RIS elements, placed at the center of the wall. It can be seen that there is not much difference in outage probability for square shaped and rectangle shaped when the RIS elements are positioned at the center. For square shaped RIS, even when the height is increased to the upper half of the wall, there is only little improvement in the outage probability. However, it is noted that some gain can be achieved when using rectangle shaped RIS especially when it is placed at a higher position on the wall. This effect

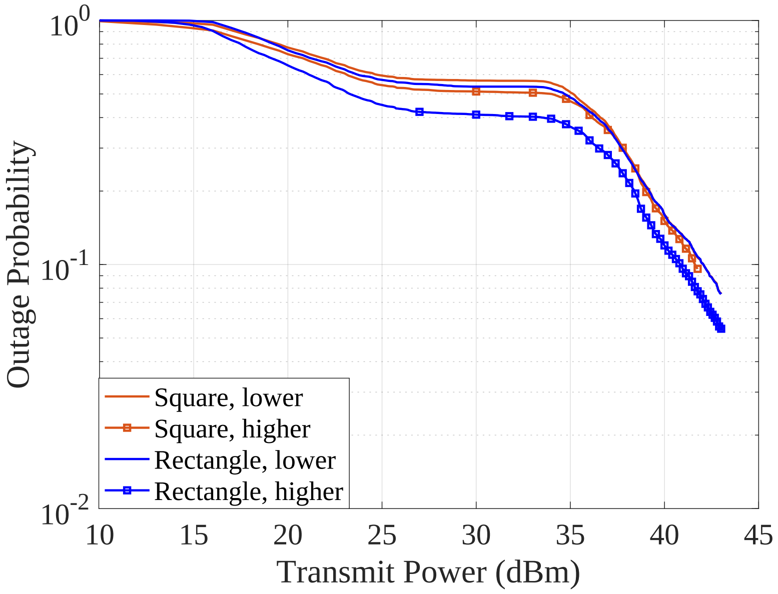

Figure 4.7: *Comparison of outage probability performance between different RIS shapes and heights when RIS is placed on one wall.*

is in fact directly related to the receiver limited FOV, the random orientation of the UE and the height of the UE. Recall from Chapter 2 that it was reported in [126] that the UE random orientation follows a Laplace distribution for sitting users ($\mu_{\mathrm{L}} = 41.39°, \sigma_{\mathrm{L}} = 7.68°$) and Gaussian distribution for walking users ($\mu_{\mathrm{L}} = 29.67°, \sigma_{\mathrm{L}} = 7.78°$). Hence, there is a minimum and maximum angle of the receiver orientation where the source may be visible by the UE and this RIS configuration can help to narrow this effect. If we consider the square shaped RIS placed at the center of the wall, it is expected that only some locations on the receivers plane that can actually receive the reflected beam from the RIS elements, which is most likely to be the locations near the wall where the RIS is placed. Also, considering the height of the receiver, the RIS elements which are below the height of the receiver will become useless as the UE will not receive the reflected signal. Moreover, when the UE gets further away from the RIS, outage will occur if the reflected link from the RIS is not within the FOV of the optical receiver. By increasing the height of the RIS elements on the wall, there is a higher chance that the reflected beam is within the FOV of the user device especially when rectangle shaped RIS is used instead of square shaped since more RIS elements are placed at a higher position on the walls.

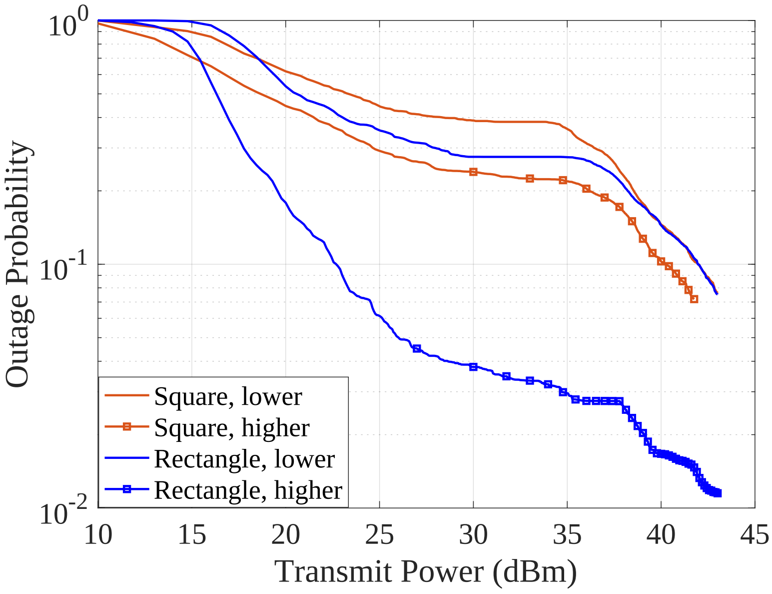

Figure 4.8: *Comparison of outage probability performance between different RIS shapes and heights when RIS is placed on all four walls.*

4.4.4 Impact of RIS Distribution

Previously, we assumed that the RIS elements are placed on only one wall. We now change the distribution of RIS where the RIS elements are now located on all four walls of the room. Fig.4.8 shows the outage probability for the whole room when RIS is placed on all four walls with each wall having the same number of RIS elements as in the previous one wall scenario. Again, we compare the outage performance between the square shaped and rectangle shaped RIS, placed either at the center or higher on the walls. By comparing Fig.4.8 with Fig.4.7, we can see that there is a considerable amount of improvement in the outage probability for square shaped RIS when they are placed on all four walls instead of only on one wall. This is obviously due to the increased total number of elements, as well as since the RIS are now evenly distributed on all sides of the room, it helps the coverage area by the RIS elements on the receiver's plane to increase and thus the UE can be in any locations in the room and still have a high chance of receiving the signal from any of the RIS elements. Furthermore, when comparing between square shaped RIS placed at the center with square shaped RIS placed at the optimal position, there is a sizeable difference in gain between the two curves for the four walls scenario whereas the gain between the two curves are comparable in the previous one wall scenario. It is noted that

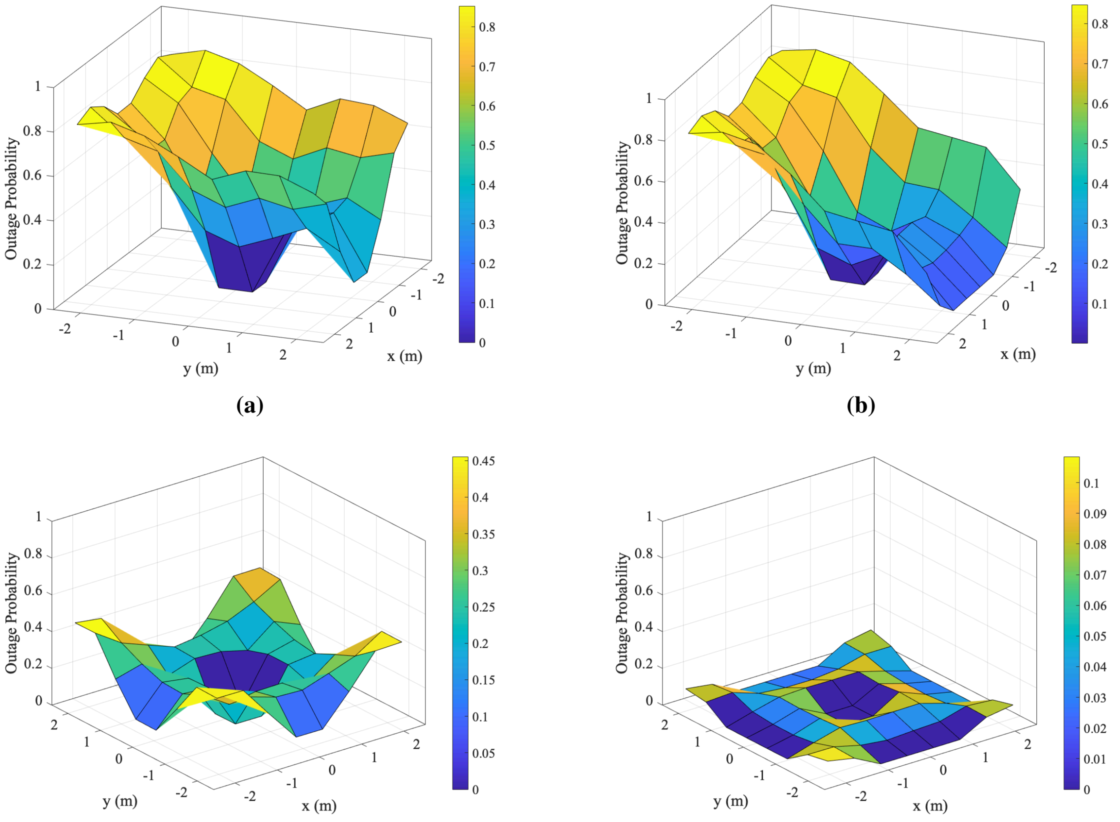

(a) **(b)**

(c) **(d)**

Figure 4.9: *Outage probability for different locations in the room: (a) one wall ($y = 2.5$), square (b) one wall ($y = 2.5$), rectangle (c) four walls, square, and (d) four walls, rectangle.*

significant improvement can be obtained when having rectangle shaped RIS placed at a higher position on the wall. For example, at outage probability of 10^{-1}, a gain of approximately 19 dB can be achieved for the four walls scenario compared to only 1 dB gain in the one wall case. Since we have determined in the previous sections that placing the RIS higher on the walls and rectangle shaped RIS would be the optimal choice of design, it is obvious that the combination of the optimal design in terms of height, shape and distribution would give the best performance in terms of outage probability.

Finally, the effect of shape and distribution of the RIS elements on the outage probability performance can be clearly seen in Fig. 4.9, which shows the 3D illustration of the outage probability

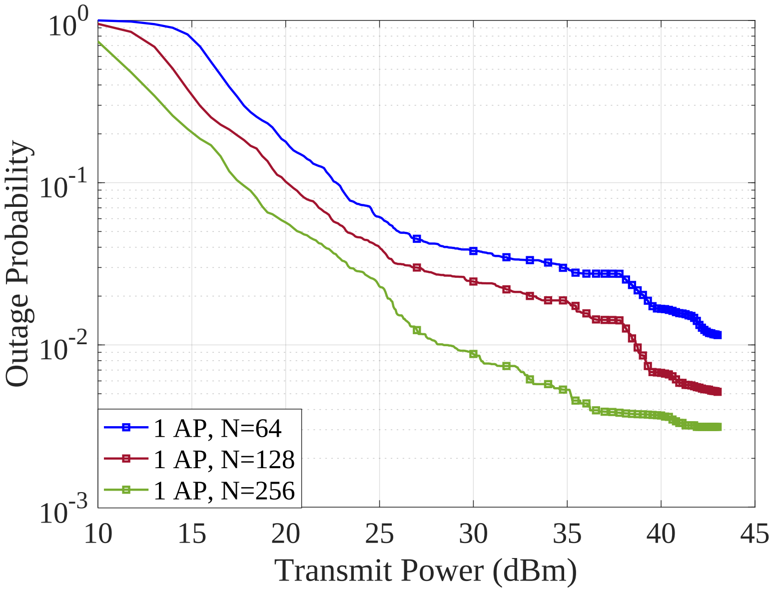

Figure 4.10: *Comparison of outage probability performance between different RIS size when RIS is placed on four walls and one AP is implemented.*

across different locations in the room. Note that for these results, the optimal height is chosen for the RIS placement. From Fig. 4.9a and Fig. 4.9b we can see how the rectangle shaped RIS further reduces the outage probability around the locations where the RIS is placed. While this effect can also be seen in Fig. 4.9c and Fig. 4.9d, comparing between Fig. 4.9a with Fig. 4.9c and Fig. 4.9b with Fig. 4.9d clearly shows the benefits of distributing the RIS on all of the walls where the outage probability close to zero can be achieved on almost all locations in the room in Fig. 4.9d which is the best scenario. Hence from the results shown in this section, it is evident that the height, size, shape, and distribution of the RIS elements have a significant effect in the performance of outage probability and it can be concluded from the results that using rectangle shaped RIS at a higher position on all four walls yields the best outage probability performance compared to the other RIS designs.

4.4.5 Impact of Number of RIS Elements

Focusing on the four walls scenario, we now investigate the effect of increasing the number of RIS elements using the best RIS design in the previous case which is the rectangular shaped

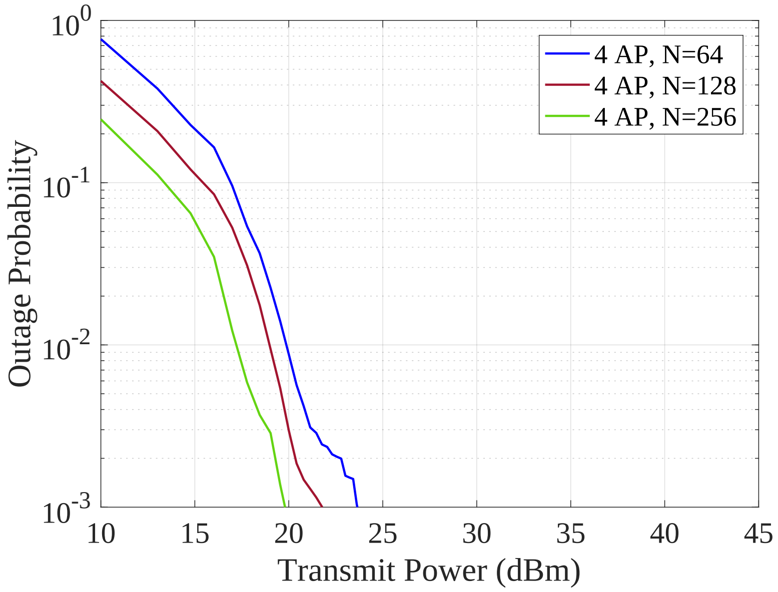

Figure 4.11: *Comparison of outage probability performance between different RIS size when RIS is placed on four walls and four APs are implemented.*

RIS placed at the higher position of the wall. Note that for this section, we consider N as the number of RIS elements per wall. Fig. 4.10 illustrate the outage probability curve for the different number of RIS elements. It is clear that by increasing the RIS elements, the outage probability can be improved considerably. As explained in the previous sections, with larger size of RIS elements, They can be focused towards more parts of the room and therefore result in an increased coverage area. Nevertheless, it is important to note that increasing the number of RIS elements will significantly increase the overall systems complexity. Hence, it is ideal to come up with a different solution to further improve the outage probability of the LiFi network with smaller number of RIS elements. This can be achieved by implementing more access points on the ceiling as the LOS link from the AP to the UE is much more stronger than the reflected links from the RIS elements. Note that even though the LOS link is stronger compared to the reflected RIS links, RIS are still needed to provide alternative LOS paths between the AP and UE when blockage exists.

Fig. 4.11 shows the outage probability when four access points are implemented. It is shown that there is a remarkable reduction in the outage probability for four AP compared to the one AP scenario. The results in Fig. 4.11 also shows that when four access points are implemented,

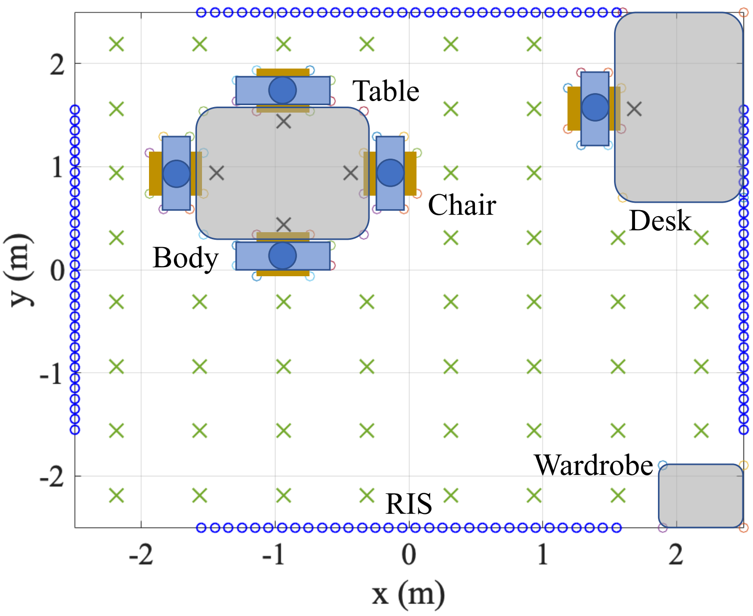

Figure 4.12: *Room geometry considered in the simulation with fixed and random blockers.*

increasing the number of RIS elements provides a slight improvement in the outage probability. As mentioned previously, the LOS links between the AP and the UE are much stronger than the RIS links, hence the gain of increasing the number of RIS elements in this case is smaller compared to when only one AP is considered. However, it should be noted that with larger number of RIS elements, we can still obtain improvements in the outage probability performance in both one AP and four APs cases. Thus, it is interesting to see from the results that with four APs, RIS with only 64 elements can achieve similar outage probability performance with that of a higher number of RIS but with even much lower computational complexity.

4.5 RIS-Aided System Performance Analysis in a Realistic Indoor Environment

In this section, we extend the analysis by also considering blockage by other fixed and random blockers (e.g., blockage by other users and furniture). The incorporation of furniture into the geometry of the room will influence the user distribution as there will be certain area within the room that will be considered as hotspot as illustrated in Fig. 4.12. In this figure, the green

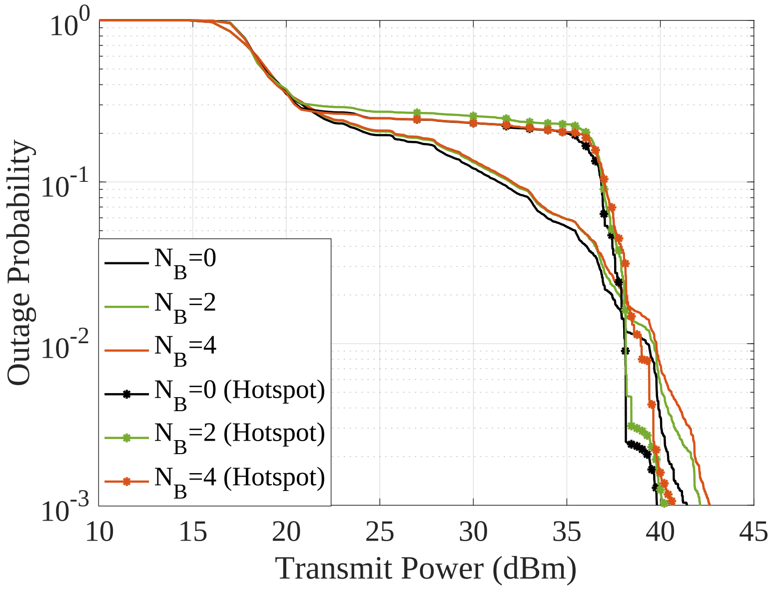

Figure 4.13: *Comparison of outage probability performance for four APs with different number of blockers, with/without hotspots and without RIS.*

colored '$\times$' symbol shows the positions of the UE when the users are standing, while the black colored '$\times$' symbol shows the locations of the UE when the users are sitting. Based on (4.4), we assume that for a number of realizations, 80% of the time, the user is sitting while the other 20% of the time, the user is standing (i.e., $\lambda = 0.8$). As a benchmark, we first compare the outage probability performance when only four APs are considered as optical source and no RIS elements are included. Fig. 4.13 shows the outage probability comparison for the case of with and without hotspot and with varying number of other user blockers. It can be seen in the figure that when furniture is included which results to having hotspots around the locations where the table, desk and chairs are placed, the outage probability becomes worse compared to the performance without hotspot for smaller transmit power. As the transmit power increases, the outage probability curves for the hotspot scenario outperform the non-hotspot case. This can be explained as for the area where the user is sitting, the user has a fixed direction (i.e., the user is facing towards the table) and the hotspot is located where the LOS link from the other APs is not strong enough since the LOS link can be easily blocked by the user itself. Thus, focusing at transmit power between $35-45$ dBm, it can be noted that when hotspots exist, higher transmit power is required in order for the outage probability to drop. Moreover, Fig. 4.13 also illustrate

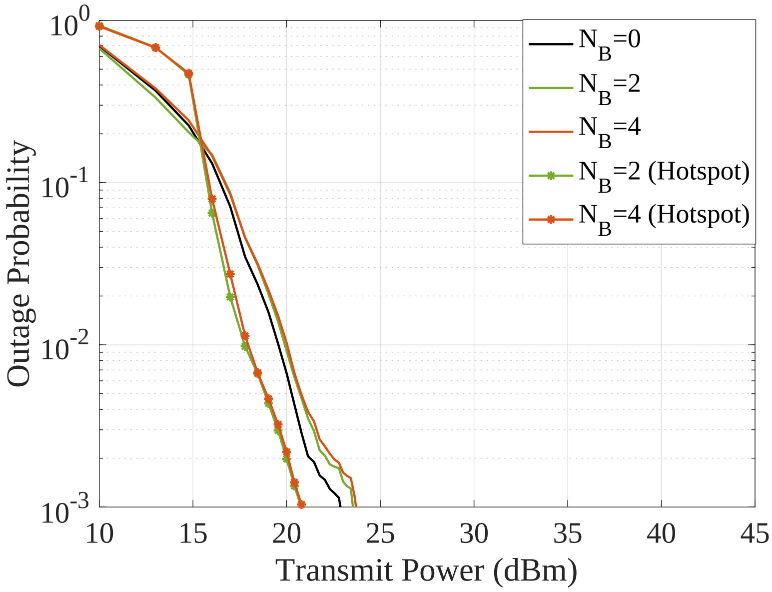

Figure 4.14: *Comparison of outage probability performance for four APs with different number of blockers, with/without hotspots and when RIS is placed on four walls.*

the effect of increasing the number of other user blockers, where the effect can be seen for both hotspot and non-hotspot scenarios. Note that in this analysis, other user blockers are assumed to be standing and is randomly distributed within the room. It is expected that with higher number of other users in the room, the UE can be easily blocked by the standing blockers which is why the outage probability gets worse especially when the number of blockers are increased.

Fig.4.14 shows the outage probability curves for the case of with and without hotspot and with varying number of other user blockers when RIS is included into the geometry of the room. It is noticeable that significant improvement in the outage probability can be obtained compared to the no RIS case in Fig. 4.13. From these results, it is evident that RIS is beneficial in helping to reduce the blockage effect caused by the user itself and also by other user blockers. From Fig. 4.14 it can be seen that when read at outage probability of 10^{-3} there is almost 20 dB improvement in the performance when RIS is placed on all four walls of the room. Furthermore, it is interesting to see that when RIS is implemented, there is almost no difference between the outage probability curves for the hotspot scenario when the number of other user blockers are increased. Therefore, it is very clear that RIS can help diminishing the effect of blockage even when the geometry of the room becomes more complex (e.g., in the presence of hotspots).

4.6 Summary

In this chapter, the effects of LOS optical link blockage on the outage performance of a LiFi network was studied. The performance analysis take into account the crucial blocking factors such as the limited FOV of the user device, random device orientation, user's self blockage, and blockage by other blockers as well as the user's distribution. An efficient method for estimating the location of user in an RIS-assisted indoor OWC system which offers a much lower computational complexity is proposed. Several RIS attributes such as shape, size, height and distribution were investigated and shown to have significant effect on the network outage probability. Finally, a numerical-based performance analysis for an RIS-aided realistic indoor LiFi network were provided where blockage by other fixed and random blockers were also considered. The proposed RIS-based solutions were shown to be capable of diminishing the blockage effect. The results show that under realistic channel conditions (e.g., effect of furniture, random orientation, FOV, blockage by other users, etc.), it is evident that RIS is beneficial in reducing the blockage effect where a gain of almost 20 dB was achieved for the outage probability performance when rectangular shaped RIS is placed on the higher side of the wall and distributed across all four walls of the room.

Chapter 5

Link Blockage Analysis for RIS-Aided Indoor OWC

5.1 Introduction

LiFi faces a number of challenges when it comes to providing seamless connectivity between the transmitter and the receiver. For example, establishing a line of sight link that achieves uninterrupted optical wireless connectivity in a realistic indoor environment can be challenging. Some of the important factors that contribute to the obstruction of the LOS link include the presence of the human body, random device orientation and the limited field of view of optical receivers. In most previous studies, only blockage by the human body are considered. However, in practical scenarios, it is also important to take into account the effect of random orientation of the user device as well as the receiver's limited FOV.

It is known that OWC is highly sensitive to the random orientation of user equipment [45]. Due to the fact that in reality most users would hold their devices in a comfortable manner, there will exist some random orientation of the UE. This random orientation is a crucial factor as a slight change in the device orientation can influence the overall performance of the UE. Another important issue is that optical receivers have commonly limited FOV. This is mainly due to the use of optics, which are significantly larger than PDs, to collect sufficient optical power while maintaining a high bandwidth for the receiver. However, this means that the angle at which the receiver can detect the optical signals is restricted. In other words, in order to establish a connection between the transmitter and the receiver, the LOS link must fall within the FOV of the receiver. When the UE is randomly oriented, the angle of the arrival beam may be occasionally beyond the limited FOV of the optical receiver, which can severely disrupt the system performance. The link blockage analysis in the literature usually consider only the LOS obstruction by the human bodies rather than also considering the impact of limited FOV of the optical receivers [46–48]. Furthermore, a unified framework to investigate the combined blockage effect including UE random orientation, FOV, and blockage by human bodies is lacking in the literature. Hence, it is important to incorporate all of these angular factors that contribute to the blockage of the LOS path in order to provide a more realistic framework for the performance analysis of an indoor OWC system.

To address the issue of blockages in an indoor LiFi communication system, a strategy that is able to establish alternative LOS paths is required. Recently, reconfigurable intelligent surfaces have emerged as one of the most effective solutions to overcome link blockages and provide coverage extension in LiFi networks [49]. In LiFi systems, RIS can be implemented either at the transmitter side, the receiver side, or in the wireless propagation medium between the transmitter and the receiver, depending on the desired functionality. RIS comprises of a number of reflecting elements that work together to create a reconfigurable wireless propagation environment in order to enhance the communication performance. Typical RIS hardware includes metasurfaces and mirror arrays which are often used in RF and LiFi systems. The optimization of RIS in RF mainly focuses on optimizing the phase shifts of the RIS elements while RIS parameters such as mirror orientation angles are typically considered in the design of RIS-aided LiFi systems. It has been shown that RIS can be successful in many different applications of the wireless communication systems, both in RF and LiFi [105–107, 154]. With this in mind, it is worth to investigate the LOS link availability in an RIS-assisted indoor LiFi communication system taking into account important effects such as the optical receiver's limited FOV, fixed and random blockers, and UE random orientation.

In the radio frequency literature, link blockage has been studied mostly in the context of millimeter wave networks as they are susceptible to severe path loss and shadowing effects. In [155] the authors have proposed a spatial-spectral interference model for dense mmWave networks, where blockage was modelled based on circular blockers with different sizes randomly placed in a finite-area. The proposed model accounts for randomness in both spectral and spatial network configurations as well as blockage effects and the results demonstrate how beam directionality and randomness in node configuration impact the accumulated interference at arbitrary locations of a mmWave network. In [156], a cone blocking model which characterizes the effect of user self-blockage was proposed for downlink mmWave systems, considering the orientation and position changes of the user body. The results in this study characterize how self-body blocking impacts the SINR coverage, however due to the larger bandwidth in mmWave systems, it can still outperform conventional systems at lower frequencies, in terms of the achievable rate. Moreover, [92, 157] have developed a body blockage model for indoor mmWave networks and the analytical expressions for the probability of blockage were derived. The authors of [92, 157] have considered the height of the blocker as one of the blocking factor, however it was assumed that the UE directionality is always aligned with the orientation of the serving AP.

Blockage has been also investigated in the OWC literature. The impact of shadowing caused by blockers were investigated in [158] for VLC systems where the expressions of the shadow area and position were derived. In [137], a system called 'NutVLC' was proposed for VLC networks to improve robustness to blockage by finding the optimal user orientation. In this work, the authors assumed that the receiver is always oriented towards the ceiling and only consider changes in the azimuth orientation of the user. The study in [159] demonstrates the implementation of cooperative and precoding schemes in VLC to overcome blockage and shadowing effects. The proposed scheme uses techniques that exploit non-line of sight components, cooperation among access points and signal processing techniques that is capable of reducing interference. RIS has been employed in non-orthogonal multiple access (NOMA) based VLC systems in [160] to provide significant enhancements in link reliability when the link is subject to blockage by other mobile users and random device orientation. The work in [160] focuses only on blockage by other users and is based on numerical simulations. Furthermore, [161, 162] proposed an access point assignment and mobility management techniques for hybrid LiFi and WiFi networks in the presence of light-path blockage. The proposed method exploits the users statistical information of LiFi channel blockage and selectively switch LiFi users to WiFi when the optical link is blocked. The authors in [139] investigated the uplink transmission of a wireless infrared-based LiFi system under the effects of random device orientation and link blockage. In this study, analytical expressions to evaluate the coverage probability of the LiFi uplink transmission were developed. Moreover, in [163], the authors investigated the impact of user mobility, random device orientation and blockage by human bodies on the performance of LiFi networks using measurement-based channel models. They have proposed a multi-directional receiver which helps to reduce the effect of random device orientation and blockage probability where blockers were modelled as rectangular prisms.

Angle diversity transmitters (ADTs) are considered as an approach to improve LOS coverage. ADTs employ multiple LED arrays where each array faces a direction specified by an elevation angle in order to focus the optical beams while creating multiple smaller cells to aid in multi-user access [164, 165]. It is important to consider an appropriate elevation angle for the LED array as it can greatly affect the systems performance. However, in most studies [166–169], the elevation angles are usually fixed and does not adapt to any changes in the LiFi environment (e.g., furniture and blockers, number of users and position of users, etc.). Meanwhile, angle diversity receivers (ADRs) are composed of multiple PDs with narrow FOV facing in different directions to allow for the expansion of the receiver FOV [170]. However, the structure of ADRs are more complex than the conventional receivers. Note that the analysis presented in this thesis focuses on receivers with limited FOV (whether with or without an ADR design), which is a common feature of most optical wireless receivers.

As previously mentioned, there are a number of reasons for which an OWC system may not be able to establish a LOS path between the transmitter and the receiver. In a practical OWC system, even in the absence of any external blockers, the limited FOV of receivers restricts the angle at which the optical signals can be collected and this limitation also depends on the random orientation of the mobile device. The LOS optical signal can be also blocked by the user's own body, furniture or other users, which are related to the user position and its direction. Note that the probability of LOS optical signal loss induced by these effects are not necessarily statistically independent from each other and therefore a unified framework is required for the performance analysis of indoor OWC systems, which is lacking in the existing literature.

In this chapter, we investigate the LOS optical link availability between the source and the user device by considering different indoor scenarios. For this purpose, we develop analytical expressions of LOS coverage probability which take into account, the limited FOV of the receiver, random device orientation, user's self blockage, and other fixed or random blockers. The main contributions of this chapter include, firstly proposing a novel analytical framework to calculate the LOS coverage probability for the single source scenario considering all the effects mentioned above. Then, we extend the analytical derivations of the LOS coverage probability to multiple source scenarios considering different source configurations. This multi-source analysis also applies to RIS-assisted OWC systems where the RIS elements can be considered as passive sources. Using the analytical model, we provide an in-depth investigation of LOS link availability by changing the crucial parameters such as FOV, the azimuth orientation of the user, the locations of the sources, and the horizontal distance between the UE and the center of the room. The accuracy of the analytical models are verified by comparing with simulation-based results and are shown to be perfectly matched. Finally, our results demonstrate the effectiveness of RIS to increase LOS coverage by considering the distribution of the RIS elements with different height positions.

The rest of this chapter is organized as follows. Section 5.2 demonstrates the analytical framework for the LOS coverage probability for single source and multi-source scenarios. The numerical results and discussions are presented in Section 5.3. Finally, this chapter is concluded in Section 5.4, and future works are highlighted.

5.2 Analytical Framework for LOS Coverage Analysis

In this section, we provide analytical expressions to calculate the LOS coverage probability considering the effects of random orientation of the UE, limited FOV, and blockage by external blockers for single-source and multiple-source scenarios, including RIS-assisted OWC networks. We show that some closed-form expressions can be derived where they are validated with numerical simulation results and therefore can be used to reduce the computational complexity of the system-level simulation.

5.2.1 Definition of LOS Coverage Probability

In order to estimate the LOS coverage probability, we define the following events with P(.) denoting the probability of an event happening:

Event 1: The event where the LOS link between the source and UE is within the FOV, defined as $\mathcal{E}_1$ as illustrated in Fig. 2.6, occurs when the angle between the source and the UE, θ_{u} is within the semi-angle FOV, Φ_{c}, i.e.:

$$\mathrm{P}(\mathcal{E}_1) = \mathrm{P}(\theta_{\mathrm{u}} \leq \Phi_{\mathrm{c}}). \tag{5.1}$$

Event 2: The event that the UE user's body is not in between the source and the UE, defined as $\mathcal{E}_2$ as illustrated in Fig. 2.8a, occurs when the azimuth angle of the UE, ω does not fall within the range defined by Θ_b, i.e.:

$$\mathrm{P}(\mathcal{E}_2) = \mathrm{P}(\omega \notin \Theta_\mathrm{b}). \tag{5.2}$$

Event 3: The event that the source is inside the blockage-free zone, defined as $\mathcal{E}_3$ as illustrated in Fig. 2.8b, occurs when the horizontal distance between the source and the UE, d_a is less than the blockage-free zone radius, z_b, i.e.:

$$\mathrm{P}(\mathcal{E}_3) = \mathrm{P}(d_\mathrm{a} \leq z_\mathrm{b}). \tag{5.3}$$

The above equation only considers a single blocker. Assuming multiple blockers at distances $r_\mathrm{b} = r_i$ from the UE, we will then have:

$$\mathrm{P}(\mathcal{E}_3) = \mathrm{P}(d_\mathrm{a} \leq \min_i[z_\mathrm{b}(r_i)]) = \prod_i \mathrm{P}(d_\mathrm{a} \leq z_\mathrm{b}(r_i)), \tag{5.4}$$

where the second equality comes from the statistical independence between the random position of different blockers and $\prod(.)$ is the product operator. Finally, the event where the UE is covered by an LOS OWC link is described by the three aforementioned events, thereby the coverage probability can be expressed as:

$$\mathcal{P}_\mathrm{c} = \mathrm{P}(\mathcal{E}_1 \cap (\mathcal{E}_2 \cup \mathcal{E}_3)). \tag{5.5}$$

5.2.2 LOS Coverage Probability for a Single Source

Given the position vector of a single optical source as $L_\mathrm{a} = (x_\mathrm{a}, y_\mathrm{a}, z_\mathrm{a})$, and the position vector of the UE as $L_\mathrm{u} = (x_\mathrm{u}, y_\mathrm{u}, z_\mathrm{u})$, the LOS link vector between the source and UE can be defined as $L_\mathrm{los} = (x_\delta, y_\delta, z_\delta) = L_\mathrm{a} - L_\mathrm{u}$. Note that the parameters defined in the last section can be described based on these position vectors. For example, $d_\mathrm{a} = \sqrt{x_\delta^2 + y_\delta^2}$ and $h_\mathrm{a} = z_\delta$. Accordingly, the angle between $\mathbf{n}'_\mathrm{u}$ and L_los can be calculated using their normalized dot product as $\cos\theta_\mathrm{u} = (\mathbf{n}'_\mathrm{u} \cdot L_\mathrm{los})/(|\mathbf{n}'_\mathrm{u}||L_\mathrm{los}|)$, where $|.|$ is the Euclidean norm operator and the magnitude of $\mathbf{n}'_{\mathrm{u}}$ is assumed to be 1. By replacing $\mathbf{n}'_{\mathrm{u}}$ with (2.22), $\cos\theta_{\mathrm{u}}$ can then be expressed as:

$$\cos\theta_{\mathrm{u}} = \frac{[\sin(\theta)\cos(\omega), \sin(\theta)\sin(\omega), \cos(\theta)]^{\mathrm{T}} \cdot (x_\delta, y_\delta, z_\delta)}{\sqrt{x_\delta^2 + y_\delta^2 + z_\delta^2}}. \tag{5.6}$$

In order for the LOS link to be available considering the limited FOV of the UE, the following condition needs to be met:

$$\cos\theta_{\mathrm{u}} \geq \cos\Phi_{\mathrm{c}}. \tag{5.7}$$

Hence, by substituting (5.6) into (5.7), we have:

$$x_\delta \sin\theta\cos\omega + y_\delta \sin\theta\sin\omega + z_\delta\cos\theta \geq \cos\Phi_{\mathrm{c}}\sqrt{x_\delta^2 + y_\delta^2 + z_\delta^2}. \tag{5.8}$$

To simplify and present equations in a compact way, let us define the left-side of (5.8) as

$$f(\omega) \triangleq (x_\delta\cos\omega + y_\delta\sin\omega)\sin\theta + z_\delta\cos\theta, \tag{5.9}$$

and the right-side of (5.8) as

$$\alpha \triangleq \cos\Phi_{\mathrm{c}}\sqrt{x_\delta^2 + y_\delta^2 + z_\delta^2}. \tag{5.10}$$

Therefore (5.8) can be represented as:

$$f(\omega) \geq \alpha. \tag{5.11}$$

By using trigonometric identities, we can rewrite (5.9) as:

$$f(\omega) = f_{\mathrm{b}}(\omega)\cos(\theta + f_{\mathrm{a}}(\omega)), \tag{5.12}$$

where

$$f_{\mathrm{a}}(\omega) = \tan^{-1}\left(\frac{-x_\delta\cos\omega - y_\delta\sin\omega}{z_\delta}\right), \tag{5.13}$$

and

$$f_{\mathrm{b}}(\omega) = \sqrt{(-x_\delta\cos\omega - y_\delta\sin\omega)^2 + z_\delta^2}. \tag{5.14}$$

By substituting (5.12) into (5.11) we have:

$$-\left|\cos^{-1}\frac{\alpha}{f_{\mathrm{b}}(\omega)}\right| \leq \theta + f_{\mathrm{a}}(\omega) \leq \left|\cos^{-1}\frac{\alpha}{f_{\mathrm{b}}(\omega)}\right|. \tag{5.15}$$

We can rewrite (5.15) as $g_{\mathrm{d}}(\omega, L_{\mathrm{u}}) \leq \theta \leq g_{\mathrm{u}}(\omega, L_{\mathrm{u}})$, where g_{d} and g_{u} are the minimum and maximum angle of the receiver orientation where the source may be visible by the UE and are functions of ω and L_{u}. Next, we mainly focus on a fixed user location, so for simplicity, we initially drop the functionality to user locations as:

$$g_{\mathrm{d}}(\omega) = -\left|\cos^{-1}\frac{\alpha}{f_{\mathrm{b}}(\omega)}\right| - f_{\mathrm{a}}(\omega), \tag{5.16}$$

and

$$g_{\mathrm{u}}(\omega) = \left|\cos^{-1}\frac{\alpha}{f_{\mathrm{b}}(\omega)}\right| - f_{\mathrm{a}}(\omega). \tag{5.17}$$

Hence, given the location of the UE, L_{u}, the polar angle of the UE, θ, and the azimuth angle of the UE, ω, the LOS coverage probability satisfying the event $\mathcal{E}_1$ can be calculated as:

$$\mathcal{P}_{\mathrm{FOV}}(\omega, L_{\mathrm{u}}) = \mathrm{P}(\mathcal{E}_1) = \int_{g_{\mathrm{d}}(\omega)}^{g_{\mathrm{u}}(\omega)} \tilde{f}_\theta \, \mathrm{d}\theta, \tag{5.18}$$

where $\tilde{f}_\theta$ is the PDF of θ which is defined based on the activity of the user. The study in [45] have collected experimental measurements of θ for sitting and walking activities and have shown that for sitting activities, Laplace distribution closely matches the distribution of the experimental measurements, while for walking activities, θ follows Gaussian distribution. Considering the sitting activity, $\tilde{f}_\theta$ can be defined as [126]:

$$\tilde{f}_\theta = \frac{\exp\left(-\frac{|\theta-\mu_\theta|}{b_\theta}\right)}{2b_\theta}. \tag{5.19}$$

Here, μ_θ and b_θ are the mean and scale parameters of Laplacian fitting, respectively, where $b_\theta = \sqrt{\sigma^2/2}$ and σ is the standard deviation obtained from experimental measurements, where the samples of angle θ are shown to be restricted to the range $[0, \frac{\pi}{2}]$ [45]. By solving the integral in (5.18) based on Laplace distribution, we obtain a closed-form expression for the LOS coverage probability due to receiver FOV limitation by averaging over different θ samples for sitting activities given as:

$$\mathcal{P}_{\text{FOV}}(\omega, L_{\text{u}}) = \begin{cases} \frac{1}{2}\bigg(\exp^{\frac{g_{\text{u}}-\mu_\theta}{b_\theta}} - \exp^{\frac{g_{\text{d}}-\mu_\theta}{b_\theta}} \bigg), & g_{\text{d}}(\omega) \leq \mu_\theta \;\;\&\;\; g_{\text{u}}(\omega) \leq \mu_\theta \\ \frac{1}{2}\bigg(\exp^{\frac{\mu_\theta - g_{\text{d}}}{b_\theta}} - \exp^{\frac{\mu_\theta - g_{\text{u}}}{b_\theta}} \bigg), & g_{\text{d}}(\omega) \geq \mu_\theta \;\;\&\;\; g_{\text{u}}(\omega) \geq \mu_\theta \\ 1 - \frac{1}{2}\bigg(\exp^{\frac{g_{\text{d}}-\mu_\theta}{b_\theta}} + \exp^{\frac{\mu_\theta - g_{\text{u}}}{b_\theta}} \bigg), & g_{\text{d}}(\omega) \leq \mu_\theta \;\;\&\;\; g_{\text{u}}(\omega) \geq \mu_\theta. \end{cases} \tag{5.20}$$

For walking activities, $\tilde{f}_\theta$ follows Gaussian distribution which is defined as [126]:

$$\tilde{f}_\theta = \frac{1}{\sigma\sqrt{2\pi}} \exp\bigg(-\frac{1}{2}\Big(\frac{\theta - \mu_\theta}{\sigma}\Big)^2 \bigg), \tag{5.21}$$

where μ_θ and σ are the mean and standard deviation of Gaussian fitting. By solving (5.18) with Gaussian distribution, the non-blockage probability for walking activities can therefore be expressed as:

$$\mathcal{P}_{\text{FOV}}(\omega, L_{\text{u}}) = \frac{1}{2}\bigg(\operatorname{erf}\Big(\frac{g_{\text{u}}(\omega) - \mu}{\sigma\sqrt{2}}\Big) - \operatorname{erf}\Big(\frac{g_{\text{d}}(\omega) - \mu}{\sigma\sqrt{2}}\Big) \bigg), \tag{5.22}$$

where $\operatorname{erf}(.)$ denotes the error function. So far, the probability of receiving the LOS signal within the receiver's FOV is analysed in the absence of any external blockers. Now, we can include the effect of any external blockers including the self blockage by defining the indicator functions that represent whether or not the LOS link is blocked before reaching the receiver. Considering the self blockage by the UE user, we can define:

$$\mathbb{1}(\omega, L_{\text{u}}) = \begin{cases} 0, & \theta_{\text{a}} - \frac{\phi_{\text{b}}}{2} \leq \omega \leq \theta_{\text{a}} + \frac{\phi_{\text{b}}}{2} \;\;\&\;\; d_{\text{a}} > z_{\text{b}} \\ 1, & \text{otherwise.} \end{cases} \tag{5.23}$$

The indicator function in (5.23) outputs a value of 1 if the body is not blocking the UE which was defined based on Θ_b and the blockage-free zone, z_{b}. Otherwise, if the body is in between the source and the UE, the function will output a value of 0, meaning that the body is blocking the UE. Note that $\text{P}(\mathcal{E}_2 \cup \mathcal{E}_3) = \text{E}[\mathbb{1}(\omega, L_{\text{u}})]$ in the case of self blockage. Now, given the user's direction, Ω, and user's location, L_{u}, the LOS coverage probability considering the effects of limited FOV and also blockage by the user's body can be obtained as:

$$\mathcal{P}_{\mathrm{c}}(\omega, L_{\mathrm{u}}) = \mathrm{P}(\mathcal{E}_1 \cap (\mathcal{E}_2 \cup \mathcal{E}_3)|\omega, L_{\mathrm{u}}) = \mathcal{P}_{\mathrm{FOV}}(\omega, L_{\mathrm{u}}) \cdot \mathbb{1}(\omega, L_{\mathrm{u}}). \tag{5.24}$$

Similarly, we can add the effect of other external blockers including fixed blockers (e.g., furniture) and/or random blockers (e.g., other users) by defining the relevant indicator functions as:

$$\mathbb{1}(L_{\mathrm{u}}, L_i) = \begin{cases} 0, & d_{\mathrm{a}} > z_{\mathrm{b}}(L_{\mathrm{u}}, L_i) \\ 1, & \text{otherwise}, \end{cases} \tag{5.25}$$

which is a function of the location of user, L_{u}, and the location of the external blocker, L_i. Then considering N_{F} fixed blockers and N_{B} random blockers, the conditional coverage probability can be written as:

$$\mathcal{P}_{\mathrm{c}}(\omega, L_{\mathrm{u}}, L_i) = \mathcal{P}_{\mathrm{FOV}}(\omega, L_{\mathrm{u}}) \cdot \mathbb{1}(\omega, L_{\mathrm{u}}) \cdot \prod_{i=1}^{N_{\mathrm{B}}} \mathbb{1}(L_{\mathrm{u}}, L_i) \cdot \prod_{j=1}^{N_{\mathrm{F}}} \mathbb{1}(L_{\mathrm{u}}, \hat{L}_j). \tag{5.26}$$

Averaging (5.26) over the location of random blockers L_i and rewrite the equation as:

$$\begin{aligned} \mathcal{P}_{\mathrm{c}}(\omega, L_{\mathrm{u}}) &= \mathcal{P}_{\mathrm{FOV}}(\omega, L_{\mathrm{u}}) \cdot \mathbb{1}(\omega, L_{\mathrm{u}}) \cdot \mathrm{E}\left[\prod_{i=1}^{N_{\mathrm{B}}} \mathbb{1}(L_{\mathrm{u}}, L_i)\right] \cdot \prod_{j=1}^{N_{\mathrm{F}}} \mathbb{1}(L_{\mathrm{u}}, \hat{L}_j) \\ &= \mathcal{P}_{\mathrm{FOV}}(\omega, L_{\mathrm{u}}) \cdot \mathbb{1}(\omega, L_{\mathrm{u}}) \cdot [1 - \mathcal{P}_{\mathrm{br}}(L_{\mathrm{u}})]^{N_{\mathrm{B}}} \cdot \prod_{j=1}^{N_{\mathrm{F}}} \mathbb{1}(L_{\mathrm{u}}, \hat{L}_j), \end{aligned} \tag{5.27}$$

where we define $\mathcal{P}_{\mathrm{br}}(L_{\mathrm{u}}) = 1 - \mathrm{E}[\mathbb{1}(L_{\mathrm{u}}, L_i)]$ as the blockage probability caused by a random blocker, which can be calculated separately for different geometries and blocker distributions. Note that the second equality in (5.27) comes from the assumption that the location of different random blockers are independent and identically distributed. Now averaging (5.27) over ω which is uniformly distributed from 0 to 2π, we have:

$$\mathcal{P}_{\mathrm{c}}(L_{\mathrm{u}}) = [1 - \mathcal{P}_{\mathrm{br}}(L_{\mathrm{u}})]^{N_{\mathrm{B}}} \cdot \prod_{j=1}^{N_{\mathrm{F}}} \mathbb{1}(L_{\mathrm{u}}, \hat{L}_j) \cdot \frac{1}{2\pi} \int_0^{2\pi} \mathcal{P}_{\mathrm{FOV}}(\omega, L_{\mathrm{u}}) \cdot \mathbb{1}(\omega, L_{\mathrm{u}}) \, \mathrm{d}\omega. \tag{5.28}$$

Note that the integral in (5.28) is not tractable but can be readily calculated numerically using closed-form equations of (5.20), (5.22), and (5.23).

5.2.3 LOS Coverage Probability of OWC Networks with RIS and/or Multiple Sources

The deployment of multiple sources is a common assumption in OWC and LiFi either for establishing a cellular network or to provide uniform illumination and increase network reliability against impairments such as blockage. Recently, the use of RIS technology is also proposed to improve network resilience. The coverage analysis of networks with multiple sources would be different from that with a single source as the UE is able to collect LOS signal from different sources. Moreover, assuming RIS elements are able to direct the light towards the user, the coverage analysis of RIS-assisted OWC networks can be also simplified into a multi-source scenario where a set of additional sources are placed at the position of different RIS elements. Therefore, here, a 'source' is considered to be either a light source or an RIS element that reflects light towards the user.

Denoting N as the total number of optical sources (i.e., including any RIS element), we first define $N_{\mathrm{A}}(\omega, L_{\mathrm{u}}, L_i) = |\mathcal{A}(\omega, L_{\mathrm{u}}, L_i)|$ as the cardinality of the set $\mathcal{A}(\omega, L_{\mathrm{u}}, L_i)$, which is the set of all 'active' sources that are not blocked by an external obstacle including the user body, furniture or other random blockers. Considering the UE user, N_{F} fixed blockers and N_{B} random blockers, the condition for the k-th source (or RIS element), denoted by S_k and located at $L_{\mathrm{a}} = L_k$, to be active is

$$\mathbb{1}(\omega, L_{\mathrm{u}}) \cdot \prod_{i=1}^{N_{\mathrm{B}}} \mathbb{1}(L_{\mathrm{u}}, L_i) \cdot \prod_{j=1}^{N_{\mathrm{F}}} \mathbb{1}(L_{\mathrm{u}}, \hat{L}_j) = 1, \tag{5.29}$$

where the indicator functions in Eq. (5.29) are given by Eq. (5.23) and Eq. (5.25). Therefore, by defining $\mathcal{P}_{\mathrm{FOV}}^{\mathcal{A}}(\omega, L_{\mathrm{u}}, L_i)$ as the probability that the LOS signal of at least one of the sources in the active set $\mathcal{A}(\omega, L_{\mathrm{u}}, L_i)$ is within the FOV of the UE, the LOS coverage probability of the OWC network with multiple light sources and/or RIS can be described as:

$$\mathcal{P}_{\mathrm{c}}(\omega, L_{\mathrm{u}}, L_i) = \mathcal{P}_{\mathrm{FOV}}^{\mathcal{A}}(\omega, L_{\mathrm{u}}, L_i). \tag{5.30}$$

Similar to the single source analysis, taking average of Eq. (5.30) over the position of random users L_i and ω which is uniformly distributed from 0 to 2π, we will have:

$$\mathcal{P}_{\mathrm{c}}(L_{\mathrm{u}}) = \mathrm{E}[\mathcal{P}_{\text{FOV}}^{\mathcal{A}}(\omega, L_{\mathrm{u}}, L_i)]. \tag{5.31}$$

Next, we present a theorem that introduces the derivation of $\mathcal{P}_{\text{FOV}}^{\mathcal{A}}(\omega, L_{\mathrm{u}}, L_i)$.

Theorem 1. *Assuming an active set of light sources and RIS elements, $\mathcal{A}(\omega, L_u, L_i)$, the LOS coverage probability (i.e., the probability that the LOS signal of at least one of the sources in the active set is within the FOV of the UE) is given by*:

$$\mathcal{P}_{\text{FOV}}^{\mathcal{A}}(\omega, L_{\mathrm{u}}, L_i) = \int_{g_{\mathrm{d}}^{1}}^{\max\limits_{1\le i\le N_{\mathrm{A}}}(g_{\mathrm{u}}^{i})} \tilde{f}_{\theta}\,\mathrm{d}\theta - \sum_{k=1}^{N_{\mathrm{A}}-1} \int_{\max(g_{\mathrm{u}}^{1},\ldots,g_{\mathrm{u}}^{k})}^{\max(g_{\mathrm{u}}^{1},\ldots,g_{\mathrm{u}}^{k},g_{\mathrm{d}}^{k+1})} \tilde{f}_{\theta}\,\mathrm{d}\theta. \tag{5.32}$$

Proof: Note that g_{d} and g_{u} are defined as the minimum and maximum angle of the receiver orientation, respectively, where an active light source or RIS element can possibly be visible by the UE. For convenience of notation, we assume that the index of the active sources are sorted in ascending order based on their respective g_{d}. Hence, after sorting, the sources are associated with pairs of g_{d}^{i} and g_{u}^{i} which are calculated based on Eq. (5.16) and Eq. (5.17), respectively, where $i = (1, 2, ..., N_{\mathrm{A}})$ indicates the i-th source. First, note that the lower and upper limits of the integral in the first term of Eq. (5.32) are the smallest angle g_{d}^{1} and largest angle $\max(g_{\mathrm{u}}^{i})$ among all active sources being visible within the receiver FOV. Hence, if the visible intervals $[g_{\mathrm{d}}^{i}, g_{\mathrm{u}}^{i}]$ for different sources are overlapping, there could be a case where the overall range of the angles are defined by the limits of integral $[g_{\mathrm{d}}^{1}, \max(g_{\mathrm{u}}^{i})]$ indicating that there is at least one visible active source. Thus, in this case, the probability of non-blockage can be simply described by the first term of (5.32). However, depending on the geometry of the light sources, RIS elements and the user locations, the union of the individual intervals is not necessarily equal to the total interval $[g_{\mathrm{d}}^{1}, \max(g_{\mathrm{u}}^{i})]$. In such case, there exist gaps between the individual intervals $[g_{\mathrm{d}}^{i}, g_{\mathrm{u}}^{i}]$ consisting of the range of angles where the source is not visible by the UE. Hence, the probability of such gaps needs to be removed from the first term in (5.32). It should be noted that for N_{A} light sources and RIS elements, there can be at most $N_{\mathrm{A}} - 1$ possible number of gaps in the visibility region of the multiple sources that must be subtracted, as shown in the second term of Eq. (5.32). This is explained in more detail and illustrated in the following base case. Next,

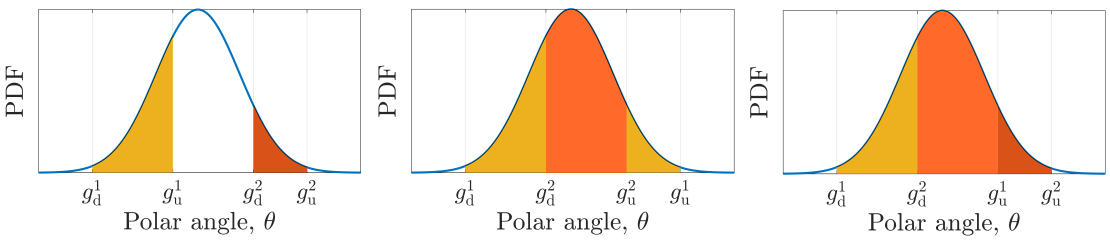

(a) **(b)** **(c)**

Figure 5.1: *Interval conditions for $N_A = 2$ (a) Condition 1: g_d^2 is greater than g_u^1, (b) Condition 2: g_d^2 is less than g_u^1 with g_u^2 also less than g_u^1, (c) Condition 2: g_d^2 is less than g_u^1 with g_u^2 greater than g_u^1.*

we use the proof by induction and show the validity of Eq. (5.32) for $N_{\mathrm{A}} = 2$ first. Then, by assuming that it is true for any $N_{\mathrm{A}} = m$, we prove that Eq.c(5.32) is also valid for $N_{\mathrm{A}} = m + 1$.

The Base Case: We first consider a base case of $N_{\mathrm{A}} = 2$ where there exist two active sources with visible intervals of $[g_{\mathrm{d}}^1, g_{\mathrm{u}}^1]$ and $[g_{\mathrm{d}}^2, g_{\mathrm{u}}^2]$. In order to determine the number of possible gaps and the limits of their integrals, we investigate two different conditions which are explained as follows.

Condition 1. $g_{\mathrm{d}}^2 > g_{\mathrm{u}}^1$: This also implies that $g_{\mathrm{u}}^2 \geq g_{\mathrm{u}}^1$ and considering Fig. 5.1a, there is a single gap between the visibility intervals of the two sources (i.e., $N_{\mathrm{A}} = 2$, thus there is $N_{\mathrm{A}} - 1 = 1$ gap in between the interval $[g_{\mathrm{d}}^1, g_{\mathrm{u}}^1]$ and $[g_{\mathrm{d}}^2, g_{\mathrm{u}}^2]$), while the LOS coverage probability can be calculated based on integration over the corresponding visible ranges as:

$$\mathcal{P}_{\mathrm{FOV}}^{\mathcal{A}}(\omega, L_{\mathrm{u}}, L_i) = \int_{g_{\mathrm{d}}^1}^{g_{\mathrm{u}}^2} \tilde{f}_\theta \, \mathrm{d}\theta - \int_{g_{\mathrm{u}}^1}^{g_{\mathrm{d}}^2} \tilde{f}_\theta \, \mathrm{d}\theta, \tag{5.33}$$

which is equivalent to (5.32) for this case.

Condition 2. $g_{\mathrm{d}}^2 \leq g_{\mathrm{u}}^1$: This condition leads to the two cases shown in Fig. 5.1b and Fig. 5.1c where it can be observed that there is no gap in the visible range of the two sources. Applying this condition to (5.32) we will get:

$$\mathcal{P}_{\mathrm{FOV}}^{\mathcal{A}}(\omega, L_{\mathrm{u}}, L_i) = \int_{g_{\mathrm{d}}^1}^{\max(g_{\mathrm{u}}^1, g_{\mathrm{u}}^2)} \tilde{f}_\theta \, \mathrm{d}\theta - \int_{\max(g_{\mathrm{u}}^1, g_{\mathrm{u}}^2)}^{\max(g_{\mathrm{u}}^1, g_{\mathrm{u}}^2)} \mathrm{d}\theta = \int_{g_{\mathrm{d}}^1}^{\max(g_{\mathrm{u}}^1, g_{\mathrm{u}}^2)} \tilde{f}_\theta \, \mathrm{d}\theta, \tag{5.34}$$

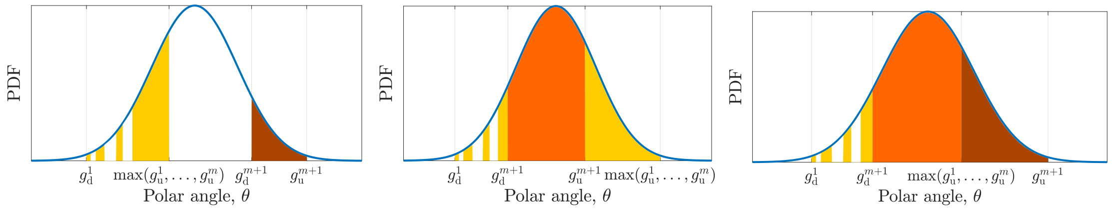

(a) **(b)** **(c)**

Figure 5.2: *Interval conditions for $N_A = m+1$ (a) Condition 1: g_d^{m+1} is greater than $\max(g_u^1,\ldots,g_u^m)$, (b) Condition 2: g_d^{m+1} is less than $\max(g_u^1,\ldots,g_u^m)$ with g_u^{m+1} also less than $\max(g_u^1,\ldots,g_u^m)$, (c) Condition 2: g_d^{m+1} is less than $\max(g_u^1,\ldots,g_u^m)$ with g_u^{m+1} greater than $\max(g_u^1,\ldots,g_u^m)$.*

which shows the validity of (5.32) that also reduces to integration over the maximum possible visible range of the two sources as shown in Fig. 5.1b and Fig. 5.1c.

The Induction Step: Here, we prove that (5.32) is valid for any $N_{\mathrm{A}} = m+1$, assuming that it is valid for any $N_{\mathrm{A}} = m$, which completes the proof by induction for any N_{A}. Consider a scenario where we have $N_{\mathrm{A}} = m+1$ arbitrary active sources, we first leave the $(m+1)$-th source out and focus on the first m sources. Noting that the index of active sources are sorted in ascending order based on their respective g_{d}, the $(m+1)$-th source is the one with largest g_{d}. Since (5.32) is assumed to be valid for any $N_{\mathrm{A}} = m$ sources, the probability of LOS coverage for the first m sources is given as:

$$\mathcal{P}_{\mathrm{FOV}}^{\mathcal{A}}(\omega, L_{\mathrm{u}}, L_i) = \int_{g_{\mathrm{d}}^{1}}^{\max\limits_{1\le i\le m}(g_{\mathrm{u}}^{i})} \tilde{f}_{\theta}\,\mathrm{d}\theta - \sum_{k=1}^{m-1} \int_{\max(g_{\mathrm{u}}^{1},\ldots,g_{\mathrm{u}}^{k})}^{\max(g_{\mathrm{u}}^{1},\ldots,g_{\mathrm{u}}^{k},g_{\mathrm{d}}^{k+1})} \tilde{f}_{\theta}\,\mathrm{d}\theta. \tag{5.35}$$

Now, if we add the $(m+1)$-th source to the rest of the group, the upper limit of the first term of (5.35) needs to include g_{u}^{m+1} since the largest visible angle of the new added source may be greater than the maximum of that of other sources. This transforms the first term of (5.35) to the first term of (5.32). It is also possible that the inclusion of the $(m+1)$-th active source changes the gaps calculated by the second term in (5.35), which is investigated below by considering two different conditions:

Condition 1. $g_{\mathrm{d}}^{m+1} > \max(g_{\mathrm{u}}^{1},\ldots,g_{\mathrm{u}}^{m})$: This also implies that $g_{\mathrm{u}}^{m+1} > \max(g_{\mathrm{u}}^{1},\ldots,g_{\mathrm{u}}^{m})$ and it is observed from Fig. 5.2a that there is a new single gap generated from $\max(g_{\mathrm{u}}^{1},\ldots,g_{\mathrm{u}}^{m})$ to

g_{d}^{m+1}. Therefore, the additional term below needs to be subtracted from (5.35):

$$\int_{\max(g_{\mathrm{u}}^1,\ldots,g_{\mathrm{u}}^m)}^{g_{\mathrm{d}}^{m+1}} \tilde{f}_\theta \,\mathrm{d}\theta = \int_{\max(g_{\mathrm{u}}^1,\ldots,g_{\mathrm{u}}^m)}^{\max(g_{\mathrm{u}}^1,\ldots,g_{\mathrm{u}}^m,g_{\mathrm{d}}^{m+1})} \tilde{f}_\theta \,\mathrm{d}\theta, \tag{5.36}$$

which simply transforms that second term of (5.35) to the second term of (5.32) and confirming the validity of (5.32) for this condition.

Condition 2. $g_{\mathrm{d}}^{m+1} \leq \max(g_{\mathrm{u}}^1,\ldots,g_{\mathrm{u}}^m)$: For this scenario, which is equivalent to Fig. 5.2b and Fig. 5.2c, there is no additional gap generated, meaning that no new terms should be subtracted from (5.35) for this condition. It is also important to note that the inclusion of the new active source does not affect the original terms of the sum in (5.35). This is because $g_{\mathrm{d}}^i \leq g_{\mathrm{d}}^{m+1}, \forall 1 \leq i \leq m$ due to initial sorting. Moreover, note that applying $g_{\mathrm{d}}^{m+1} \leq \max(g_{\mathrm{u}}^1,\ldots,g_{\mathrm{u}}^m)$ to the last term (i.e., $k = m+1$) of the sum in (5.32) reduces it to zero as:

$$\int_{\max(g_{\mathrm{u}}^1,\ldots,g_{\mathrm{u}}^m)}^{\max(g_{\mathrm{u}}^1,\ldots,g_{\mathrm{u}}^m,g_{\mathrm{d}}^{m+1})} \tilde{f}_\theta \,\mathrm{d}\theta = \int_{\max(g_{\mathrm{u}}^1,\ldots,g_{\mathrm{u}}^m)}^{\max(g_{\mathrm{u}}^1,\ldots,g_{\mathrm{u}}^m)} \tilde{f}_\theta \,\mathrm{d}\theta = 0, \tag{5.37}$$

which proves the validity of (5.32) for this condition as well and concludes the proof by induction. ■

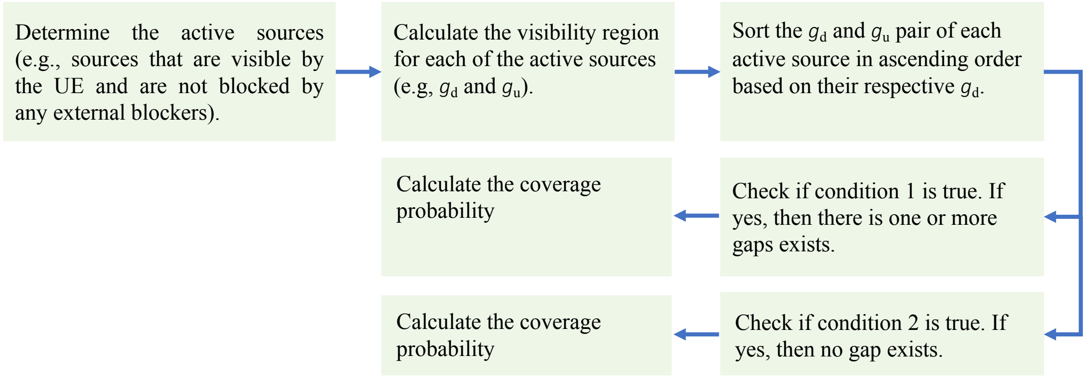

Figure 5.3: *Steps for calculating the LOS coverage probability for multiple source scenario*

Corollary 1. *By applying Gaussian probability distribution to* (5.32) *, the closed-form expression of the LOS coverage probability for walking users can be calculated based on* (5.30) *in the* *presence of multiple light sources and/or RIS elements as:*

$$\mathcal{P}_{\mathrm{c}}(\omega, L_{\mathrm{u}}) = \frac{1}{2}\Bigg(\mathrm{erf}\left(\frac{\max\limits_{1\leq i\leq N_{\mathrm{A}}} (g_{\mathrm{u}}^{i}) - \mu_{\theta}}{\sigma\sqrt{2}} \right) - \mathrm{erf}\left(\frac{g_{\mathrm{d}}^{1} - \mu_{\theta}}{\sigma\sqrt{2}} \right)\Bigg)$$
$$- \sum_{k=1}^{N_{\mathrm{A}}-1} \frac{1}{2}\Bigg(\mathrm{erf}\left(\frac{\max(g_{\mathrm{u}}^{1}, \ldots, g_{\mathrm{u}}^{k}, g_{\mathrm{d}}^{k+1}) - \mu_{\theta}}{\sigma\sqrt{2}} \right) - \mathrm{erf}\left(\frac{\max(g_{\mathrm{u}}^{1}, \ldots, g_{\mathrm{u}}^{k}) - \mu_{\theta}}{\sigma\sqrt{2}} \right)\Bigg). \quad (5.38)$$

Note that the LOS coverage probability can be similarly calculated for sitting activities. The main steps for calculating the LOS coverage probability for RIS and/or multiple sources is summarised in Fig. 5.3.

5.3 Performance Analysis

Parameter	**Value**	**Parameter**	**Value**
RIS elements per wall, $N_{\mathrm{ris}} \times N_{\mathrm{ris}}$	16	Size of each RIS element	$10\,\mathrm{cm} \times 10\,\mathrm{cm}$
Receiver FOV, Φ_c	$45°, 60°, 90°$	Number of source, N	$1, 4$
User body width, w_{b}	$40\,\mathrm{cm}$	Body shadowing angle, ϕ_{b}	$67.38°$
User body height, h_{u}	$170\,\mathrm{cm}$	Blockage free zone radius, z_{b}	$95\,\mathrm{cm}$
Horizonal distance of UE to user, r_{b}	$30\,\mathrm{cm}$	Height difference of UE to user, h_{b}	$60\,\mathrm{cm}$
Height difference of UE to source, h_{a}	$190\,\mathrm{cm}$		

Table 5.1: *List of Parameters*

In this section, we discuss the LOS link availability in the presence of blockage due to the user body, random orientation of user device, and limited FOV and we show the results in terms of LOS coverage probability for single source and multiple source scenario as well as in the absence and presence of RIS. Considering that there are several works in the literature focusing on the impact of blockage by external blockers, in this section we mainly focus on self-blockage by the user and the impact of limited FOV and random orientation of the user device in order to give a more generic insight into the LOS coverage of the LiFi networks. Note that, the analysis presented in the last section can be also applied for any realistic indoor environment with a set of fixed furniture and potential random blockers. In our numerical results, we consider a $5\,\mathrm{m} \times 5\,\mathrm{m} \times 3\,\mathrm{m}$ room and a target user with a height h_{u} of $1.7\,\mathrm{m}$ and a body width w_{b} of $0.4\,\mathrm{m}$. The height difference between the user and the UE, denoted as h_{b}, where $h_{\mathrm{b}} = h_{\mathrm{u}} - z_{\mathrm{u}}$ is assumed to be $0.6\,\mathrm{m}$ and the UE is placed at a distance, r_{b} of $0.3\,\mathrm{m}$ away from the user. The user facing direction, Ω and UE azimuth angle ω takes value between $0°$ to $360°$ based on a uniform distribution. The UE polar angle, θ is generated based on Laplace or Gaussian distribution, depending on the user activity. In the single source scenario, the optical source is assumed to be positioned at the centre of the ceiling (i.e., $L_{\text{a}} = (0, 0, 1.5)$ while for the multiple source scenario, four optical sources are placed on the ceiling following a square topology (i.e., $L_{\text{a}} = (\pm 1.25, \pm 1.25, 1.5)$). We also consider the incorporation of RIS with $N_{\text{ris}} \times N_{\text{ris}}$ elements, which will be shown to be crucial in increasing LOS coverage probability in an indoor environment. We assume a commonly used square-shaped RIS structure to get a general insight of the benefits of RIS in improving the LOS coverage in an indoor LiFi systems [49, 106, 107]. The list of simulation parameters with fixed values used in this work can be found in Table 5.1 [45].

Algorithm 2: Simulation Algorithm

```
Initialization; denote $L_{\text{a}} = (x_{\text{a}}, y_{\text{a}}, z_{\text{a}})$ as the source location; $L_{\text{u}} = (x_{\text{u}}, y_{\text{u}}, z_{\text{u}})$ as the UE's location; $\cos\Phi_{\text{c}}$ as the UE FOV; $w_{\text{b}}$ as the user body width; $h_{\text{b}}$ as the user body height;
for each location do
    Calculate $L_{\text{los}}$, $\theta_{\text{a}}$, $\phi_{\text{b}}$, $z_{\text{b}}$ and $d_{\text{a}}$
    for each $\Omega$ do
        for each AP do
            if $d_{\text{a}} > z_{\text{b}}$ then
                if $\omega \in \mathbb{\Theta}_{\text{b}}$ then
                    AP body blockage status = 1
                else
                    AP body blockage status = 0
                end if
            else
                AP body blockage status = 0
            end if
        end for
        Generate $\theta$ samples based on Laplace or Gaussian distribution
        for each $\theta$ do
            Calculate $\theta_{\text{u}}$
            Check condition ($\cos\theta_{\text{u}} >= \cos\Phi_{\text{c}}$)
            Return LOS coverage status; if any one of the AP covers the UE, then LOS coverage
```

```
status = 1, otherwise, LOS coverage status = 0
            end for
            Calculate LOS coverage probability averaged over all $\theta$ samples
        end for
        Calculate LOS coverage probability averaged over all $\Omega$ values
        Return LOS coverage probability
    end for
```

As an example, we describe the simulation for the multiple source scenario which shows how blockage (e.g., self-blockage) is determined based on the different conditions mentioned in Section 5.2. Using the fixed parameters listed in Table 1, and given the location of the source, L_a and the location of the UE, L_u, the user facing direction, Ω can take any value between $0°$ to $360°$. To include the effect of random orientation of the user device, samples of the UE polar angle, θ is generated based on Laplace or Gaussian distribution, depending on the user activity (e.g., whether the user is sitting or walking). For a given location, L_los, θ_a, ϕ_b, z_b and d_a are calculated. Then, for each user facing direction (i.e., Ω), the LOS coverage status from each source considering self-blockage by the user body is determined based on the conditions mentioned in Section 5.2.1. In order to do this, we first check whether d_a is greater than z_b (i.e., the source is outside the blockage-free zone). If this condition is true, we then determine whether the user body is in between the UE and the source by checking whether ω is within the range Θ_b. This will give the blockage status of the UE due to the user body. If the UE is not blocked by the user body, we then determine whether there is LOS coverage due to the effect of receiver FOV. Hence, for each θ samples, θ_u is calculated based on the dot product between L_los and n'_u. If θ_u is smaller than the receiver FOV, then the UE is covered, otherwise there is no LOS coverage for the UE. This process is repeated to determine the LOS coverage status for different values of Ω and θ samples. Finally, we calculate the LOS coverage probability for that single location by averaging over all considered orientation angles. This simulation procedure is summarized in Algorithm 2.

5.3.1 Single Source

This section presents the results when a single optical source in considered in a LiFi system. Firstly, Fig. 5.4 shows the analytical and simulation results for the LOS coverage probability for

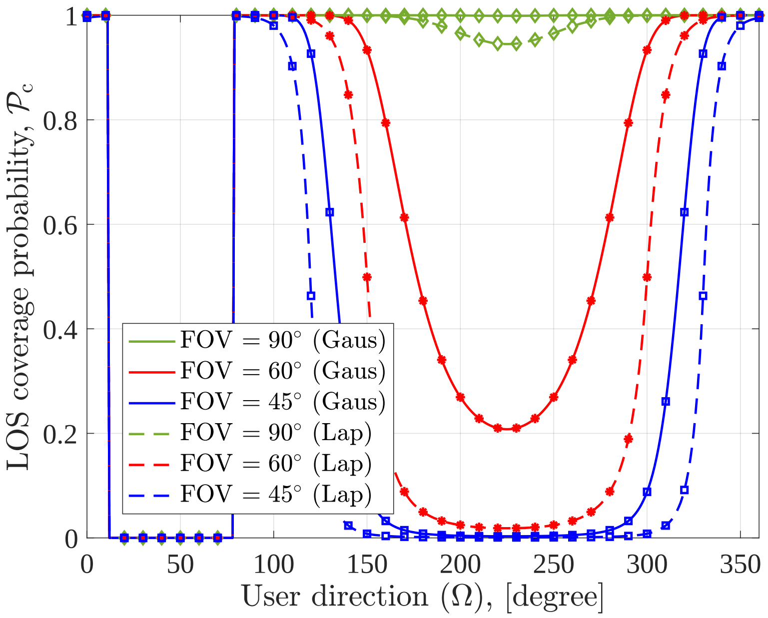

Figure 5.4: *Single source scenario - Effect of body blockage and limited FOV with changing user facing direction for a given location.*

both static and walking scenarios (i.e., PDF of θ follows either Laplace or Gaussian distribution) when the location of the UE is assumed to be $L_\text{u} = (1, 1, z_\text{u})$ and given the user direction. Note that the solid and dashed lines indicate the results based on the analytical model, while the markers indicate the simulation results obtained based on Algorithm 2 for the single source scenario. When varying the user direction, Ω, (e.g., the user rotates it's body at a fixed location as seen in Fig. 2.6.2) which is linearly related to the angle ω, the effect of limiting the FOV can clearly be seen. At a certain angle, the coverage probability is at its maximum when the UE is facing the optical source and when the body is not blocking the UE. In other words, there is a direct LOS between the source and the UE. Due to the random orientation of the receiver, as the user changes its direction, the UE starts to face away from the source and we can see that the LOS coverage probability decreases gradually. The coverage probability later increases again when the UE goes back to its original facing direction where the LOS link is strong. We can also observe the effect of blockage due to the user body being in between the source and the UE. This only happens when $\theta_\text{a} - \frac{\phi_\text{b}}{2} \leq \omega \leq \theta_\text{a} + \frac{\phi_\text{b}}{2}$. In this scenario, when Ω is ranging from 11° and 79°, the UE is completely blocked by the user and the LOS coverage probability becomes zero. Moreover, when comparing the performance between different FOV values, it is clear that with

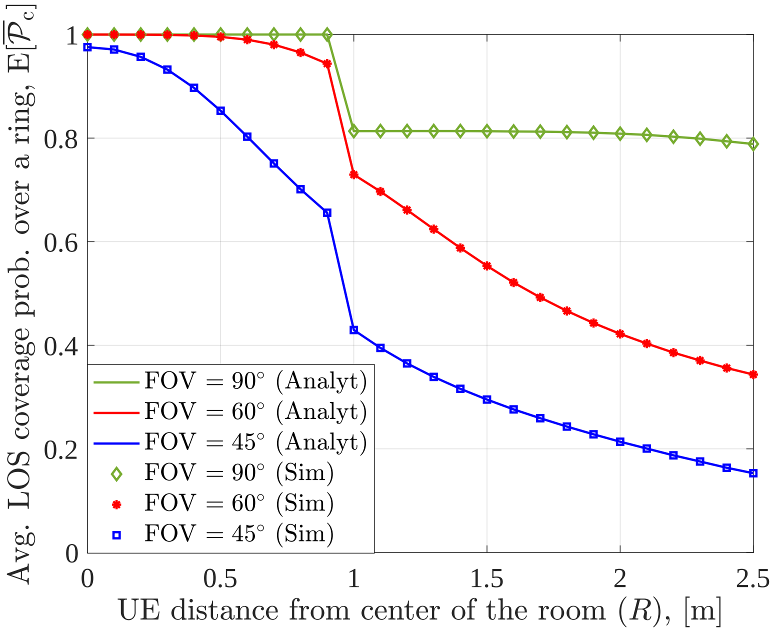

Figure 5.5: *Single source scenario - Effect of body blockage and limited FOV with increasing distance between the UE and the center of the room.*

smaller FOV, the coverage probability decreases since the angle at which the receiver is able to capture the LOS link is smaller.

Fig. 5.4 also shows the comparison of the LOS coverage probabilities between two different user scenarios, namely, the static users (e.g., the user is sitting) and the walking users. As mentioned in the previous sections, for sitting activities, the PDF of the polar angle, θ follows Laplace distribution, while for walking activities, the PDF of θ follows Gaussian distribution. From this figure, we can see that the coverage probability is slightly higher for mobile users compared to static users. This is expected as Gaussian distribution has a higher standard deviation compared to Laplace distribution, and therefore the values of θ are spread out over a wider range. Note that for the rest of this study, we mainly focus on the results for mobile users scenario and therefore Gaussian distribution is used to model the PDF of the polar angle.

The effect of body blockage and limited FOV on LOS coverage probability is also studied in Fig. 5.5 and Fig. 5.7 where the coverage probability is averaged over different user directions Ω (or equivalently over ω) at different distances of UE from the centre of the room. For each

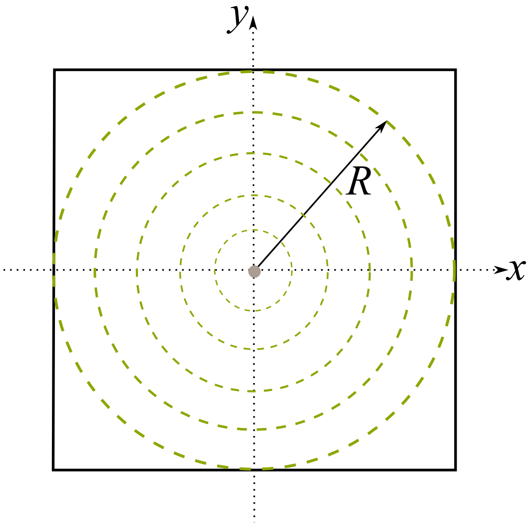

Figure 5.6: *2D illustration of user's location averaged over a ring with radius R from the center of the room*

user location, we first obtain the averaged coverage probability over different user direction Ω, as shown in Fig. 5.7. Afterwards, the average LOS coverage probability over different user locations are calculated in Fig. 5.5 by averaging over multiple user locations on a ring, denoted as $\mathrm{E}[\overline{\mathcal{P}}_{\mathrm{c}}]$ that satisfy $x_{\mathrm{u}}^2 + y_{\mathrm{u}}^2 = R^2$, where R is the radius of the ring from the center of the room as illustrated in Fig. 5.6. From Fig. 5.5, it can be seen that the LOS coverage probability slowly decreases as the UE gets farther away from the center. This is expected as since the source is placed at the center, when the distance between the UE and the source increases, the LOS link between the source and the UE may not be established due to the FOV limitation. This effect becomes much more significant with smaller FOV. Furthermore, the sudden drop of the curve at $R = 0.95$ is due to the impact of body blockage. As mentioned in Section 5.2.1, we know that as long as the distance between the UE and the source is less than the blockage-free zone, there will be no blockage due to the user body and therefore the LOS coverage is only affected by the FOV. Body blockage only happens when the distance between the UE and the source becomes larger than the blockage free zone (i.e., $d_{\mathrm{a}} > z_{\mathrm{b}}$). In this case, based on Eq. (2.24), $z_{\mathrm{b}} = 0.95$. Hence, it can be seen that the LOS coverage probability reduces when the distance is more than $z_{\mathrm{b}} = 0.95$. As shown in Fig. 5.7, with larger FOV (e.g., FOV $= 90°$), it is clear that the minimum average LOS coverage probability is higher than 50% with the locations near the center of the room,

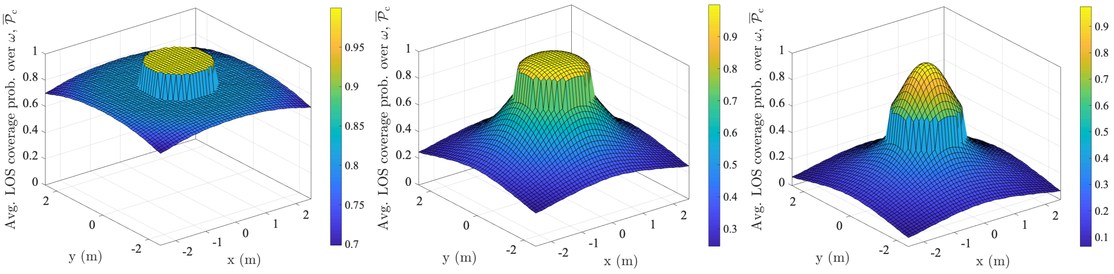

(a) **(b)** **(c)**

Figure 5.7: *The LOS coverage probability distribution over the whole room for a single source scenario when: (a) FOV* $= 90°$*, (b) FOV* $= 60°$*, and (c) FOV* $= 45°$*.*

which are not blocked by the body blockage, has a maximum coverage probability. However, as the size of FOV reduces, it is observed that the area covering the locations that are not blocked by the users body becomes narrower. As seen in Fig. 5.7c the FOV is limited and therefore only the locations that are extremely close to the center has a LOS coverage probability that is near the maximum value. The results shown in this section collectively demonstrate the accuracy of our analytical expressions for the single source scenario's coverage probability, where the analytical results match with the simulation results.

5.3.2 Multiple Sources and RIS

In this section, we analyse the LOS coverage under the presence of random orientation, limited FOV and blockages when multiple optical sources, single optical source with RIS, and multiple optical sources with RIS are considered in the room environment. The different types of source configurations are depicted in Fig. 5.8. In Fig. 5.8a, four light sources are placed on the ceiling following a square grid with $L_{\mathrm{a}} = (\pm 1.25, \pm 1.25, 1.5)$. In the second configuration as shown in

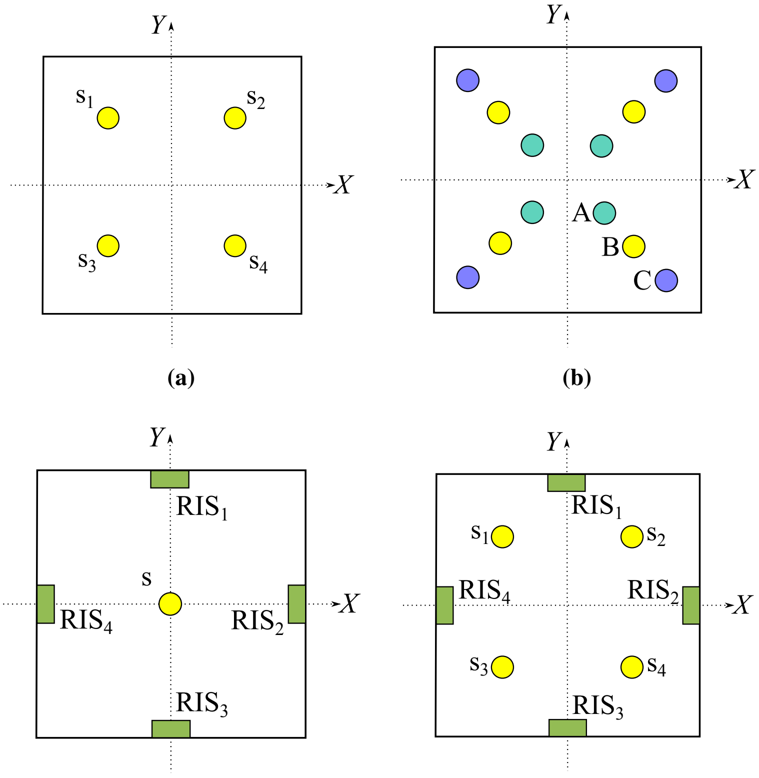

(a) **(b)**

(c) **(d)**

Figure 5.8: *2D room geometry for multiple source scenarios: (a) four sources, (b) four sources with different configurations, (c) one source and four RIS, and (d) four sources and four RIS.*

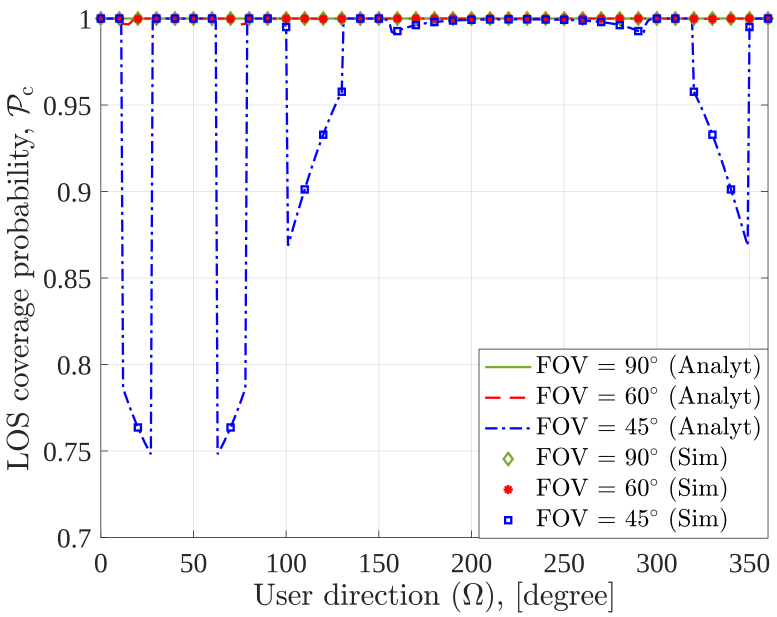

Figure 5.9: *Four source scenario - Effect of body blockage and limited FOV with changing user facing direction for a given location.*

Fig. 5.8b, three different placement of light sources is considered where configuration A is when all of the four sources are located near the center of the room (i.e., $L_{\mathrm{a}} = (\pm 0.5, \pm 0.5, 1.5)$), configuration B is the same positions as in the default set up (i.e., $L_{\mathrm{a}} = (\pm 1.25, \pm 1.25, 1.5)$), and configuration C is when the sources are placed close to the walls (i.e., $L_{\mathrm{a}} = (\pm 2, \pm 2, 1.5)$). Furthermore, we also consider placing RIS on each wall of the room for the one source and four source scenarios as shown in Fig. 5.8c and Fig. 5.8d, respectively. Note that the results presented in this section is based on the LOS coverage probability expressions derived for multiple source scenario in section 5.2.3, since the incorporation of RIS elements can be modelled by additional light sources located at the position of each RIS element.

5.3.2.1 Four Optical Sources

In this scenario, four light sources are placed on the ceiling which follows the configuration as shown in Fig. 5.8a. Note that the numerical results in the rest of section 5.3 are obtained based on the proposed analytical model. Fig. 5.9 presents the comparison between analytical and simulation results of the LOS coverage probability for different FOV and Ω when four sources

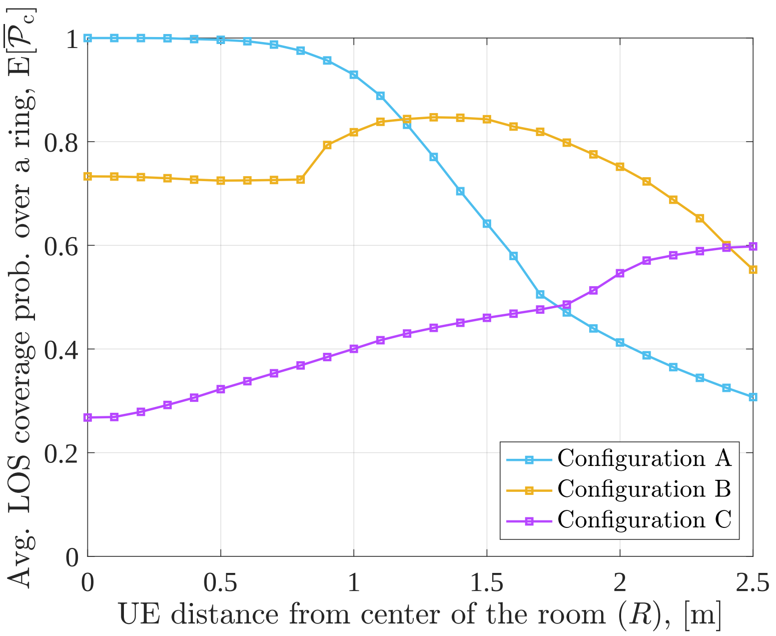

Figure 5.10: *Four source scenario - Effect of various placements of sources when FOV* $= 45°$.

are considered and the UE location is $L_{\mathrm{u}} = (1, 1, z_{\mathrm{u}})$. Comparing to Fig. 5.4, it is obvious that when the number of optical sources are increased, the coverage probability increases significantly with the minimum coverage probability at certain user directions is not less than 75%. This is expected as the UE only needs a direct LOS link with at least one of the sources to be considered not blocked. Fig. 5.9 also shows that for most of the user direction angles, there is LOS coverage for FOVs $90°$ and $60°$. However, for FOV $= 45°$, the highs and lows of the curve is the effect of whether the UE has established a LOS connection with either one of the sources. Initially, the LOS coverage probability reduces since at that certain angle, the UE is starting to face away from sources S_1, S_3 and S_4. However, the coverage probability increases again as the UE starts to face towards S_2. Since the location of the UE is very close to S_2, there is no blockage by the user body at the angles where the UE is facing towards this source.

Fig. 5.10 depicts the effect of three different placement of sources on the LOS coverage probability when FOV $= 45°$. The results in Fig. 5.10 demonstrate that as the UE gets further away from the center of the room, placing the sources using configuration B provides a better coverage probability on average, compared to configurations A and C. In fact, the average LOS coverage probability over the range of R are 72%, 75% and 43% for configurations A, B, and

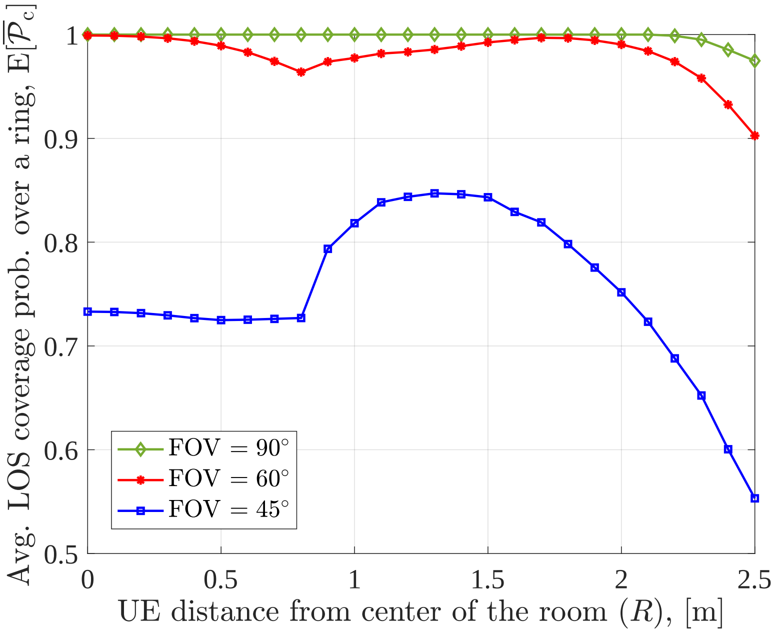

Figure 5.11: *Four source scenario - Effect of body blockage and limited FOV with increasing distance between the UE and the center of the room.*

C, respectively.

Similar to the single source scenario, we obtain the LOS coverage probability for different FOV averaging over different Ω and multiple locations of the UE at different distances of UE from the centre of the room as shown in Fig. 5.11 and Fig. 5.12. We first analyse the performance with increasing distance between the UE and the center of the room and plot the results in Fig. 5.11. By comparing Fig. 5.11 and Fig. 5.5, the LOS coverage probability greatly improves when the number of sources is increased from one source to four sources. Essentially, this figure proves that the use of multiple sources, which are not co-located, helps to eliminate the effect of self-body-blockage and to reduce the loss of LOS due to limited FOV. Again, comparing Fig. 5.11 and Fig. 5.5, there is a noticeable difference in the initial trend of the curves for FOV $= 45°$. This is due to the location of the sources which instead of being at the center of the room (e.g., single source scenario), they are now placed further away from the center. The reduction of the curve that happen when $R = 0.8$ for FOVs of $60°$ and $45°$ is due to the fact that since the UE gets further away from the center, the coverage probability decreases, however after a certain point (i.e., $R = 0.8$), the LOS coverage probability increases as it gets closer to the locations

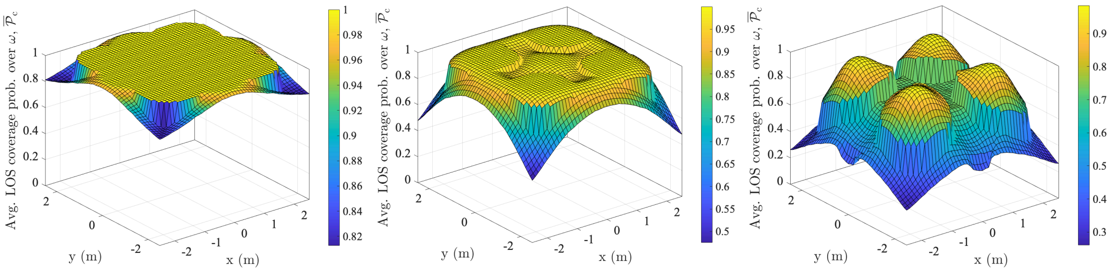

Figure 5.12: *The LOS coverage probability distribution over the whole room for four sources scenario when: (a) FOV* $= 90°$*, (b) FOV* $= 60°$*, and (c) FOV* $= 45°$*.*

of the sources. The coverage probability then reduces again when getting further away from the sources and closer to the walls. Finally, the distribution of the LOS coverage probability averaged over different directions of the user is generated for the whole room as shown in Fig. 5.12 where the coverage probability close to one covers a wider area compared to the single source scenario. It is also seen in Fig. 5.12c that even with limited FOV, increasing the number of sources can reduce the effect of body blockage.

5.3.2.2 One Optical Source with Four RIS

In this subsection, instead of only using optical sources, we now consider a scenario where we implement one optical source placed at the center of the ceiling and four RIS placed at the center of the upper half of each wall. The top view of the positions of the optical source and the RIS is presented in Fig. 5.8c. On each wall, we place one RIS with 4×4 elements with each element having a size of $10\,\text{cm} \times 10\,\text{cm}$. Therefore, the total number of RIS elements on each wall is 16 with a total size of $40\,\text{cm} \times 40\,\text{cm}$. Here, we keep the location of the UE fixed at $L_\text{u} = (1, 1, z_\text{u})$. For a better understanding, we can compare Fig. 5.13 with Fig. 5.4. The main difference between these two figures is that when RIS is included, at certain angles where the body is in between the source and the UE (e.g., Ω is between $11°$ and $79°$) or when the UE is facing away from the optical source, the RIS helps to compensate the blockage that happens

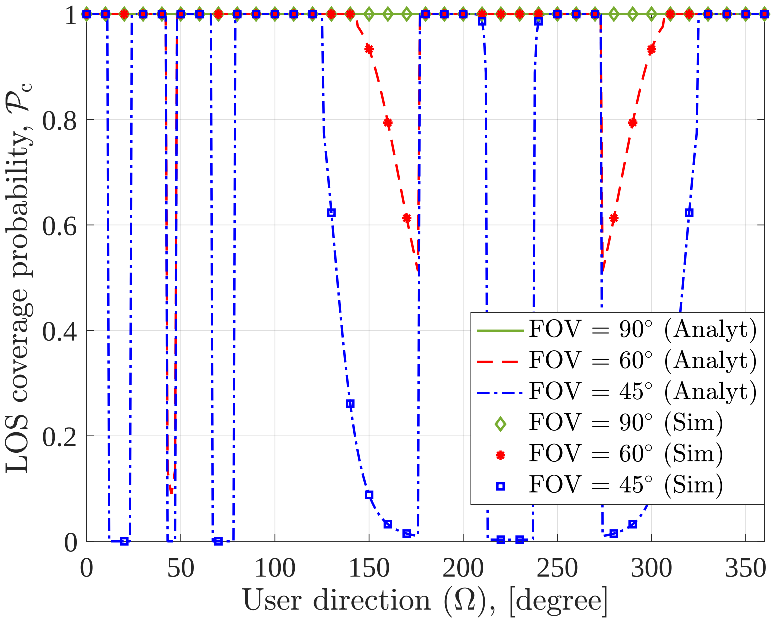

Figure 5.13: *One source and four RIS scenario - Effect of body blockage and limited FOV with changing user facing direction for a given location.*

between the UE and the source. Moreover, for FOVs 90° and 60°, the LOS coverage probability is mostly 1, which means that there is almost no blockage by the body and the limited FOV. We can also see in this figure that when FOV $= 45^\circ$, at the angles where the body is in between the source and the UE (i.e., the source is blocked by the body), the UE still has a LOS link with at least one of the RIS elements which is why the UE is still covered. Meanwhile, when the user direction is between 213° and 237°, the LOS coverage probability decreases to its minimum since the UE is not facing towards the RIS while at the same time there is no LOS between the source and the UE due to the small FOV. Hence it is worth noting that, when the optical source is blocked, as long as one of the RIS elements can provide direct LOS with the UE, then there is no blockage at the UE. Similarly, when all of the RIS elements are blocked by the user body, since the LOS link between the source and the UE is not blocked by the user body, it explains why the coverage probability is one at these angles. Hence, this explains the highs and lows of the LOS coverage probability curves in Fig. 5.13.

Fig. 5.14 and Fig. 5.15 shows the LOS coverage probability for one source and four RIS which is averaged over Ω at different locations. Again, Fig. 5.14 is the coverage probability averaged

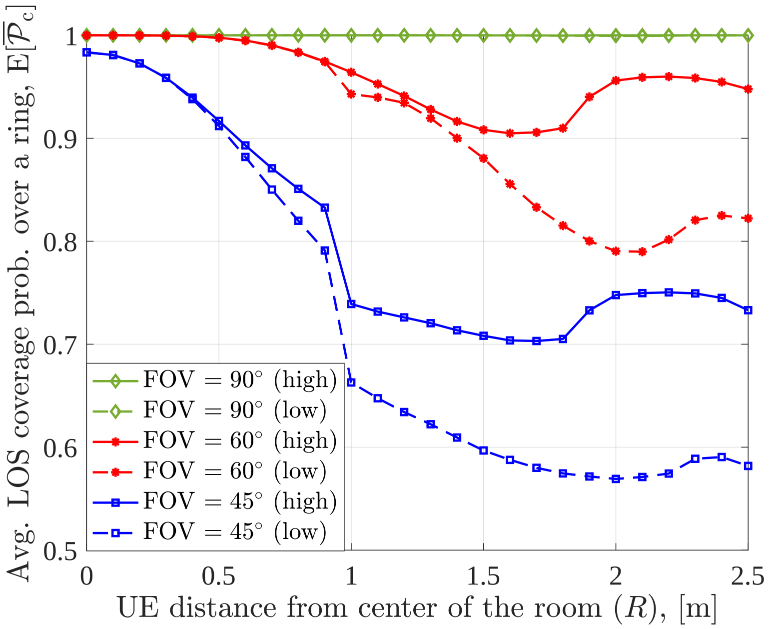

Figure 5.14: *One source and four RIS scenario - Effect of body blockage and limited FOV with increasing distance between the UE and the center of the room and the effect of changing RIS heights.*

over multiple locations with increasing horizontal distance of the UE from the center of the room. The solid lines represents the coverage performance for the current placement of the RIS, which is at the upper half of the wall while the dashed lines is when the height of the RIS is reduced (i.e., RIS is placed at the center of the wall). The behavior of the curves in this figure is similar to the single source scenario. However, when comparing Fig. 5.14 and Fig. 5.5 we can see a significant improvement in the LOS coverage performance where the coverage probability averaged over different locations in the room is more than 70% in the case of RIS placed at higher positions. Hence from this figure, it is clear that distributing the RIS elements on multiple walls can hugely reduce the blockage due to the user body or limited FOV. Furthermore, due to the random orientation of the UE and the size of FOV, the height of the RIS is an important factor to consider. The dashed lines in Fig. 5.14 shows that when the RIS is placed at a lower height, the coverage probability decreases. This effect can further be seen especially when the size of the FOV becomes smaller. This is because when the height difference between the RIS and the UE is small, there is lower chance of having LOS link between them due to the limited FOV. Therefore, it would be more practical to place the RIS higher on the walls. It is worth mentioning that when

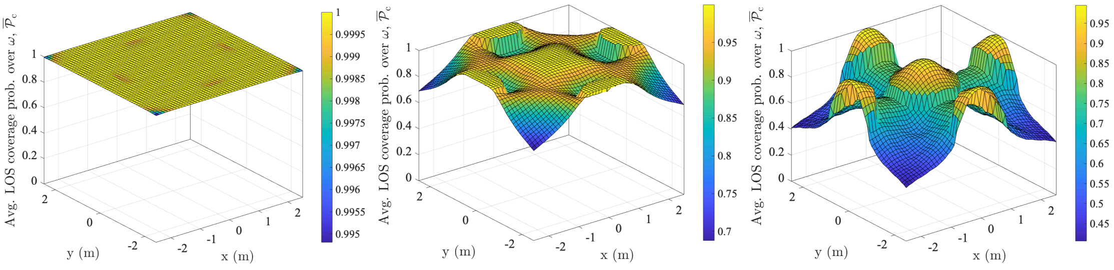

(a) **(b)** **(c)**

Figure 5.15: *The LOS coverage probability distribution over the whole room for one source and four RIS scenario when: (a) FOV* $= 90°$*, (b) FOV* $= 60°$*, and (c) FOV* $= 45°$*.*

investigating the optimal placement of RIS elements on the walls of the room, in order for the RIS to effectively reflect the light at a higher position, the Lambertian light source would need a larger divergence angle, otherwise the light incident on RIS may not be sufficiently strong, especially when the Lambertian optical source is oriented downwards. However, it should be noted that, in this work, we focus on the absence or availability of the LOS link and the full analysis of the strength of the received LOS signal, which would be directly related to the source divergence angle is left for future work. Finally, the distribution of the LOS coverage probability for the whole room with different FOV can be seen in Fig. 5.15. It is interesting to see in Fig. 5.15a that for FOV $= 90°$, the average LOS coverage probability for almost all of the locations in the room is one compared to one source and four source scenarios, meaning there is always LOS coverage. This further shows the effectiveness of evenly distributing the RIS elements on different walls of the room to reduce the blockage effect.

5.3.2.3 Four Optical Sources with Four RIS

In this subsection, we compare the performance of the LOS coverage probability when four optical sources and four RIS are considered. The optical sources are placed on the ceiling, following the same geometry as the four source scenario, while the RIS are implemented on all of the four walls in the room as can be seen in Fig. 5.8d. Fig. 5.16 shows the coverage probability when the location of the UE is assumed to be $L_\mathrm{u} = (1, 1, z_\mathrm{u})$. When changing the azimuth angle of the user, we can see that there is always LOS coverage for FOVs $90°$ and $60°$. Even when the FOV becomes very limited, (e.g., FOV $= 45°$), the LOS coverage probability is

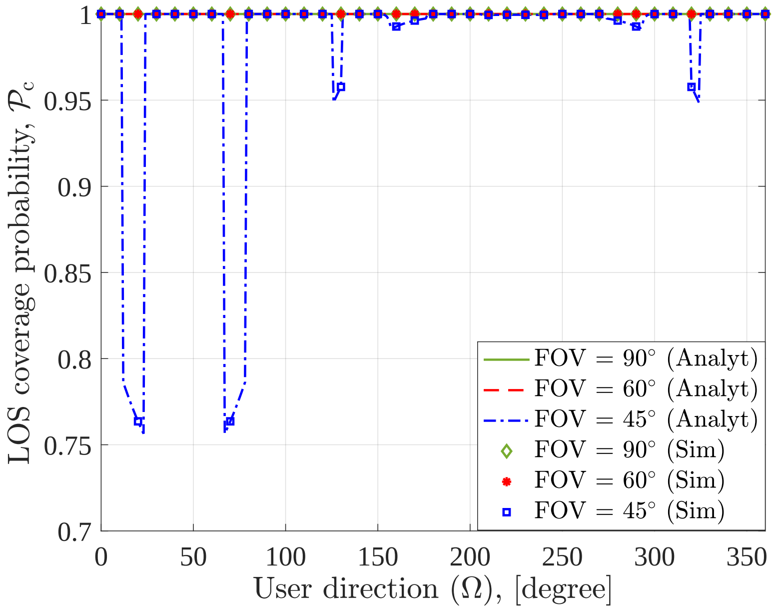

Figure 5.16: *Four source and four RIS scenario - Effect of body blockage and limited FOV with changing user facing direction for a given location.*

still at its maximum for most of Ω. Moreover, the effect of body blockage are also reduced due to the fact that there are now more sources that can establish direct LOS with the UE. It is worth mentioning that in Fig. 5.16 when the user direction is between 200° and 250°, the UE is facing away from the RIS, and from most of the optical sources. However, the UE is facing towards one of the optical source (e.g., S_2) and since the UE is located very close to that source, the user body does not block the UE.

We then compare the LOS coverage probability averaged over the different locations on a ring with radius R in the room and plotted the results with increasing distance between the UE and the center as shown in Fig. 5.17. From this figure, again, we can see similar behaviors with the results shown in the previous scenarios. The coverage probability slowly reduces as the UE gets farther away from the source due to the FOV limitation. We can see that by having an increased number of optical sources and having RIS distributed on all of the four walls, it can further increase the LOS coverage probability especially for FOV $= 45°$. It is also shown in the figure that placing the RIS at a higher position on the walls still provides better performance compared to when putting the RIS at a lower height. The distribution of the LOS coverage probability

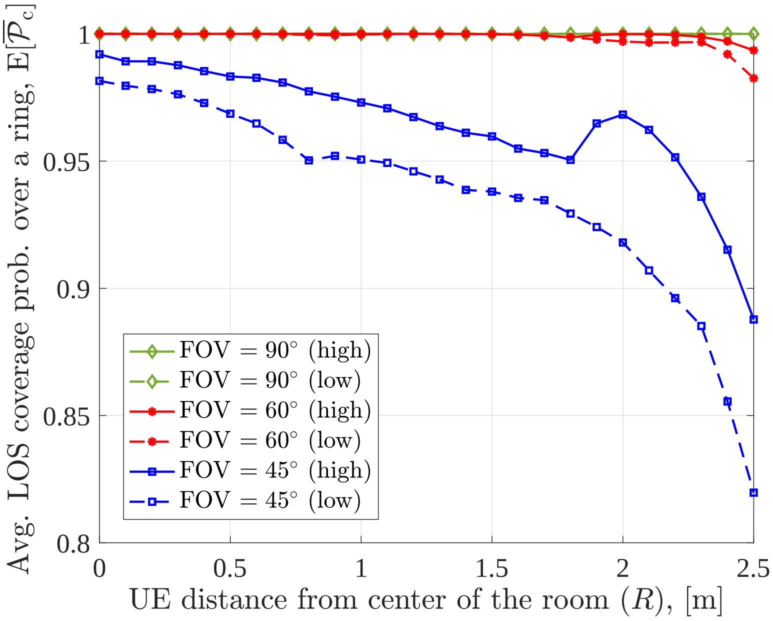

Figure 5.17: *Four source and four RIS scenario - Effect of body blockage and limited FOV with increasing distance between the UE and the center of the room and the effect of changing RIS heights.*

over different locations in the room for different FOVs are illustrated in Fig. 5.18. Based on this figure, it is expected that by having multiple optical sources and RIS, the area of which there are always LOS link availability (i.e., LOS coverage probability is maximum) will definitely increase.

5.4 Summary

In this chapter, an analytical framework for the calculation of LOS coverage probability of indoor optical wireless communication systems were presented considering crucial factors that can highly influence LOS blockage. As a result, some closed-form analytical expressions of the LOS coverage probability for single source and multiple source scenarios and/or RIS were derived while taking into account the effects of limited FOV of the receiver, random orientation of the UE and blockage by the user body and by other external blockers. The LOS link availability was investigated using the derived analytical model by varying the FOV, user direction, source and RIS positions and locations of the receiver. The results obtained based on the analytical

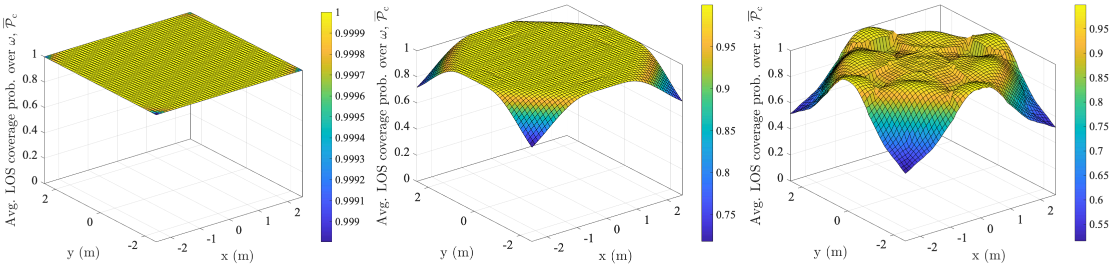

(a) **(b)** **(c)**

Figure 5.18: *The LOS coverage probability distribution over the whole room for four source and four RIS scenario when: (a) FOV* $= 90°$, *(b) FOV* $= 60°$, *and (c) FOV* $= 45°$.

model show perfect match with the simulation-based results. It was shown in the single source scenario (e.g., without RIS), the LOS coverage probability for FOV$= 90°$ is higher than 50% with the maximum coverage probability at the center of the room where the AP is located. As the FOV reduces, it was observed that the area covering the locations that are not blocked by the users body becomes narrower. When the number of APs was increased, the coverage probability at all user locations for FOV$= 90°$ were above 75%. Furthermore, when RIS was implemented, coverage probability of above 50% was achieved for all locations even when the FOV is limited (e.g., FOV$= 45°$). Thus, the deployment of multiple sources and/or RIS was proven to be useful in minimizing the impact of link blockage and therefore improving the LOS coverage in an indoor wireless communication systems.

Chapter 6
Conclusions, Limitations and Future Research

6.1 Summary and Conclusions

In this research thesis, an analysis of the LiFi network under the influence of fixed and random blockers was presented. It was observed that the LiFi channels are relatively deterministic and therefore improvements of the communication metrics such as SNR, BER, user throughput, blockage probability and outage probability can be achieved. By exploiting the CSI of the LiFi networks affected by link blockage and user behaviour, a more detailed analysis can be conducted in order to develop effective solutions for supporting seamless connectivity of LiFi communication and networking schemes. In this thesis, deep learning methods were used to model a realistic LiFi channel. It was shown that the proposed methods offers a simple detection and resource allocation approach particularly when access to real-time CSI is restricted. Moreover, a realistic framework for the performance analysis of LiFi networks in terms of outage probability was demonstrated and different layout designs of RIS that can best alleviate the joint blockage effect caused by the fixed and random blockers was analysed. Finally, a unified framework for link blockage analysis under the presence of random device orientation, limited FOV, self-blockage and blockage by other external blockers was presented for an indoor LiFi communication system and it was shown that RIS provides an effective solution to diminish these effects. In summary, the three main findings of this research thesis are as follow.

- Incorporating the distinct features of realistic indoor environment in the design of LiFi systems using DL techniques. Specifically, two DL-based schemes was proposed to aid in the signal detection and resource allocation problems in LiFi-OFDM system.

- Providing an efficient channel acquisition method for the RIS-assisted indoor OWC system and performance analysis of LiFi in the presence of fixed and random blockers in order to support seamless connectivity in LiFi networks.

- Deriving a novel analytical framework for calculating the blockage probability considering all blockage effects induced by the limited FOV of the receiver, random orientation of the UE, user's self-blockage, and other random and fixed blockers.

In chapter 2, the relevant background related to LiFi channels and networks was presented. A brief introduction and history of VLC and LiFi systes were provided. Then, the LiFi channel model was described, which included the effect of both front-end elements and the effect of indoor LiFi channel. The LOS and NLOS DC gains have been explained and optical OFDM, which is an effective way of combating the ISI in LiFi networks, is described. The basic concept of LiFi attocells are provided and OFDMA as the most common multiuser access techniques in the downlink are described. Afterwards, the user behavior models which include the device orientation and blockage that can affect the system performance are explained. Then, different types of deep learning algorithms for solving non-linear channel estimations are discussed. Finally, RIS which is a method of diminishing the blockage affect are described.

In chapter 3, an indoor LiFi system with realistic channel model was considered by including the specific geometrical configurations and user behavior effects. With these channel models, two learning based approaches were then introduced for improving the performance of signal detection and resource allocation. We compared the performance between the proposed learning methods and the conventional algorithms and demonstrated that the learning based schemes outperform the traditional methods as it has the ability to adapt to the specific changes in the environment and user behavior scenarios. Unlike the conventional techniques, the DL-based method has shown to give good performance even when there are irregularities in the system environment. By considering the channel as a black box, the proposed DL methods were able to indirectly estimate the channel and yield high gains in the performance of signal detection with an SNR gain of approximately 9 dB and 15 dB was obtained for LSTM-based approach compared to MMSE and LS, respectively, and resource allocation especially in the event of having partial CSI and with furniture taken into account. Simulation results showed that our DL models, with limited instantaneous knowledge of the channel, were able to perform almost similar to the optimal traditional techniques with perfect CSI. We also demonstrated the robustness of the learning based schemes in adapting to different user behavior scenarios by implementing user hotspot models. The simulated results confirm our expectation that DL-based schemes are able to operate better than traditional methods when specific indoor scenarios were considered with LSTM achieving SNR penalty of less than 2.5 dB against the optimal ML estimation.

In chapter 4, the effects of LOS optical link blockage on the outage performance of a LiFi network is studied. The performance analysis take into account the crucial blocking factors such as the limited FOV of the user device, random device orientation, user's self blockage, and blockage by other blockers as well as the user's distribution. An efficient channel acquisition method for the RIS-assisted indoor OWC system which offers a much lower computational complexity is proposed. Several RIS attributes such as shape, size, height and distribution were investigated and shown to have significant effect on the network outage probability. Finally, a numerical-based performance analysis for an RIS-aided realistic indoor LiFi network were provided where blockage by other fixed and random blockers were also considered. The proposed RIS-based solutions were shown to be capable of diminishing the blockage effect. The results show that under realistic channel conditions (e.g., effect of furniture, random orientation, FOV, other user blockers, etc.), it is evident that RIS is beneficial in reducing the blockage effect where a gain of almost 20 dB was achieved for the outage probability performance when rectangular shaped RIS is placed on the higher side of the wall and distributed across all four walls of the room.

In chapter 5, an analytical framework for the calculation of LOS coverage probability of indoor optical wireless communication systems were presented considering crucial factors that can highly influence LOS blockage. As a result, some closed-form analytical expressions of the LOS coverage probability for single source and multiple source scenarios with RIS were derived while taking into account the effects of blockage due to the limited FOV of the receiver, random orientation of the UE and blockage by the user body and by other external blockers. The characteristics of link blockage was investigated using the derived analytical model by varying the FOV, user direction, source and RIS positions and locations of the receiver. The results obtained based on the analytical model showed perfect match with the simulation-based results. It was shown in the single source scenario (e.g., without RIS), the LOS coverage probability for FOV$= 90^\circ$ is higher than 50% with the maximum coverage probability at the center of the room where the AP is located. As the FOV reduces, it was observed that the area covering the locations that are not blocked by the users body becomes narrower. When the number of APs was increased, the coverage probability at all user locations for FOV$= 90^\circ$ were above 75%. Furthermore, when RIS was implemented, coverage probability of above 50% was achieved for all locations even when the FOV is limited (e.g., FOV$= 45^\circ$). Thus, the deployment of multiple sources and/or RIS was proven to be useful in minimizing the impact of link blockage and therefore improving the LOS coverage in an indoor wireless communication systems.

6.2 Limitations and Future Research

In Chapter 3, LSTM and DFNN were implemented to improve the performance of signal detection and resource allocation applications, respectively. This was mainly due to the suitability of the neural network architecture for these kind of regression and classification problems. Though, other DL techniques such as CNN which are also commonly used in the literature can also be investigated for future work. Moreover, since it is known that the LiFi channel is quasi-static, it is assumed in this work that the indoor environment remains unchanged. However, as future research direction, it is possible to consider the scenario where the environment changes over time (e.g., in the case where the furniture is moved to a different location) and apply another type of learning method known as transfer learning to update the deep learning network with new data instead of having to train the neural network from scratch. Furthermore, the training and testing data for the neural networks were based on numerical simulations. Hence, real experimental data can be collected to increase the accuracy of the realistic LiFi channels, as well as the generalization ability and training performance of the neural networks which could be considered as a future research study. It is worth mentioning that one of the focus in this chapter is to train the deep learning neural networks through offline training in order to reduce the complexity of the system in real-time. As a future research topic, we can focus on the implementation of online learning approaches such as reinforcement learning to directly update the network with data in real-time. In addition, it is assumed in the signal detection and resource allocation problems that the input data to the neural networks are the detected signal and the channel gain, respectively. However, other metrics may be also considered as the input features for the training of the neural network which may enhance the network learning performance. It is noted that self-blockage and blockage by furniture were considered in this work, thus, blockage by other users can also be the focus for future work. Other than that, multi-user system with multiple cells in the presence of user mobility with random orientation could also be a future research topic.

In terms of implementation challenges for the proposed DL-based networks, it is noted that most of the DL-based algorithms are still in their simulation stages. Thus, researchers still have to improve these algorithms considerably before DL networks can be implemented. More specifically, an authentic set of data from real communication systems in actual physical environments must be made available to train the DL architectures on common measured data. Moreover, evaluating the proposed models in a computer simulation environment may be deceptive since there are many more impairments in real-life scenarios. Given that the current DL networks are mainly trained offline, their generalization capability must be guaranteed. Furthermore, DL tools for hardware, such as field programmable gate array (FPGA), must be developed to deploy the DL methods on hardware and achieve fast realization. Many wireless products have limited memory and CPU capabilities which do not allow for complex algorithms to be programmed into their existing protocols. Since DL has iterative execution nature, it may elongate the system response time and thus DL algorithms should be optimized to reduce the execution time.

In Chapter 4, in order to reduce the complexity of the outage analysis, it was assumed that only first order reflection of the NLOS channel components was considered. Therefore, developing a framework for the derivation of infinite order of the NLOS channel gain which can be combined with the reflection from the RIS elements could be considered as a future research topic. In fact, using the frequency domain analysis as explained in Chapter 2, we can extend this approach to also include reflections from the RIS. Furthermore, as a future research direction, we could also measure the channel gains based on the LOS, NLOS and RIS components through experiments and include them in the performance analysis of a realistic LiFi network. In addition, other performance metrics such as throughput and QoS can also be assessed under the implementation of RIS. On the other hand, multi-user scenario can also be a focus for future research topic where resource allocation problem comes into play which could be improved with the help of RIS.

In Chapter 5, the coverage probability framework was developed based on the LOS channel only. Hence, blockage analysis with the consideration of NLOS channel components may also be considered as the focus for future research. Moreover, in this chapter we have provided the analytical derivations for the LOS coverage probability under the influence of fixed and random blockers. As a future research direction, we could also include numerical simulations considering blockage by other fixed and random blockers such as furniture and other users. Additionally, we can extend the blockage analysis and investigate the performance of RIS for a larger sized room with a more complex geometry. Furthermore, it is assumed in this work that the RIS elements are optimally aligned towards the center of the user equipment. In practical scenarios, there may be some alignment error which could effect the received power at the UE. Thus, this issue can be taken into consideration in the future work as well as the optimization of the RIS configurations such as orientation etc.

Appendix A
List of Publications

The list of published papers are included here.

A.1 Journal Papers

N. A. Amran, M. D. Soltani, M. Yaghoobi, and M. Safari, "Learning Indoor Environment for Effective LiFi Communications: Signal Detection and Resource Allocation," *IEEE Access*, vol. 10, pp. 17 400–17 416, 2022.

A.2 Conference Papers

N. A. Amran, M. Dehghani Soltani, M. Yaghoobi, and M. Safari, "Deep Learning Based Signal Detection for OFDM VLC Systems," *in 2020 IEEE International Conference on Communications Workshops (ICC Workshops)*, 2020, pp. 1–6.

N. A. Amran, M. Dehghani Soltani, and M. Safari, "Link Blockage Analysis for Indoor Optical Wireless Communications," *in 2023 IEEE Global Communications Conference (GLOBECOM): Optical Networks and Systems*, Dec. 2023.

Bibliography

[1] M. Milasevic and M. Hofer, "Digital Living: Who are the Next Billion Internet Users?" [Online] Available: https://www.euromonitor.com/article/digital-living-who-are-the-next-billion-internet-users, 2022.

[2] "Cisco Annual Internet Report (2018-2023) White Paper," Cisco, San Jose, California, USA, White Paper, 2020.

[3] S. Mukherjee, S. Roy, S. Ghosh, and S. Mandal, "3 A comparative study of Li-Fi over Wi-Fi and the application of Li-Fi in the field of augmented reality and virtual reality," *Augmented and Virtual Reality in Social Learning: Technological Impacts and Challenges*, vol. 3, p. 27, 2023.

[4] M. Z. Chowdhury, M. T. Hossan, A. Islam, and Y. M. Jang, "A comparative survey of optical wireless technologies: Architectures and applications," *ieee Access*, vol. 6, pp. 9819–9840, 2018.

[5] C. Ruth, "Internet users are estimated to reach 6 billion in the next 5 years," [Online] Available: https://atlasvpn.com/blog/internet-users-are-estimated-to-reach-6-billion-in-the-next-5-years, Aug. 2023.

[6] M. Calabrese, "Solving the Spectrum Crunch: Dynamic Spectrum Management Systems," *Dynamic Spectrum Alliance (DSA)*, Oct. 2023.

[7] H. Elgala, R. Mesleh, and H. Haas, "Indoor optical wireless communication: potential and state-of-the-art," *IEEE Communications Magazine*, vol. 49, no. 9, pp. 56–62, 2011.

[8] H. Haas *et al.*, "Introduction to indoor networking concepts and challenges in LiFi," *Journal of Optical Communications and Networking*, vol. 12, no. 2, pp. A190–A203, 2020.

[9] H. Haas, L. Yin, Y. Wang, and C. Chen, "What is lifi?" *Journal of lightwave technology*, vol. 34, no. 6, pp. 1533–1544, 2015.

[10] Y.-C. Chi *et al.*, "Phosphorous Diffuser Diverged Blue Laser Diode for Indoor Lighting and Communication," *Scientific Reports*, vol. 5, no. 1, p. 18690, 2015.

[11] D. Tsonev, S. Videv, and H. Haas, "Light fidelity (Li-Fi): towards all-optical networking," in *Proc. SPIE 9007, Broadband Access Communication Technologies VIII*, ser. Proceedings of SPIE, B. Dingel and K. Tsukamoto, Eds. United States: SPIE, 2013, photonics West Conference on Broadband Access Communication Technologies VIII ; Conference date: 04-02-2014 Through 06-02-2014.

[12] M. B. Rahaim, A. M. Vegni, and T. D. C. Little, "A hybrid Radio Frequency and broadcast Visible Light Communication system," in *2011 IEEE GLOBECOM Workshops (GC Wkshps)*, 2011, pp. 792–796.

[13] X. Wu, M. D. Soltani, L. Zhou, M. Safari, and H. Haas, "Hybrid LiFi and WiFi Networks: A Survey," *IEEE Commun. Surv. Tutor.*, vol. 23, no. 2, pp. 1398–1420, 2021.

[14] B. Mitchell, "How Much Power Does a Network Router Use?" [Online] Available: https://www.lifewire.com/power-network-router-consumes-3971320, 2021.

[15] J. Marsh, "How many watts does a light bulb use?" [Online] Available: https://www.energysage.com/electricity/house-watts/how-many-watts-does-a-light-bulb-use, 2023.

[16] S. U. Rehman, S. Ullah, P. H. J. Chong, S. Yongchareon, and D. Komosny, “Visible Light Communication: A System Perspective—Overview and Challenges,” *Sensors*, vol. 19, no. 5, 2019. [Online]. Available: https://www.mdpi.com/1424-8220/19/5/1153

[17] M. D. Soltani, X. Wu, M. Safari, and H. Haas, “Bidirectional User Throughput Maximization Based on Feedback Reduction in LiFi Networks,” *IEEE Trans. Commun.*, vol. 66, no. 7, pp. 3172–3186, July 2018.

[18] J. M. Kahn and J. R. Barry, “Wireless infrared communications,” *Proc. IEEE*, vol. 85, no. 2, pp. 265–298, 1997.

[19] S. Idris, A. M. Aibinu, G. Koyunlu, and J. Sanusi, “A Survey of Modulation Schemes in Visible Light Communications,” in *2019 3rd International Conference on Trends in Electronics and Informatics (ICOEI)*, 2019, pp. 1–7.

[20] F. A. Dahri, S. Ali, and M. M. Jawaid, “A review of modulation schemes for visible light communication,” *Int. J. Comput. Sci. Netw. Secur*, vol. 18, no. 2, p. 117, 2018.

[21] S. D. Dissanayake and J. Armstrong, “Comparison of ACO-OFDM, DCO-OFDM and ADO-OFDM in IM/DD Systems,” *J. Lightw. Technol.*, vol. 31, no. 7, pp. 1063–1072, April 2013.

[22] S. D. Dissanayake, K. Panta, and J. Armstrong, “A novel technique to simultaneously transmit ACO-OFDM and DCO-OFDM in IM/DD systems,” in *2011 IEEE GLOBECOM Workshops (GC Wkshps)*. IEEE, 2011, pp. 782–786.

[23] S. M. Mana, K. G. K. Gabra, S. M. Kouhini, P. Hellwig, J. Hilt, and V. Jungnickel, “An efficient multi-link channel model for LiFi,” in *2021 IEEE 32nd Annual International Symposium on Personal, Indoor and Mobile Radio Communications (PIMRC)*. IEEE, 2021, pp. 1–6.

[24] M. A. Arfaoui, M. D. Soltani, I. Tavakkolnia, A. Ghrayeb, C. M. Assi, M. Safari, and H. Haas, “Invoking Deep Learning for Joint Estimation of Indoor LiFi User Position and Orientation,” *IEEE Journal on Selected Areas in Communications*, vol. 39, no. 9, pp. 2890–2905, 2021.

[25] M. Uysal, F. Miramirkhani, T. Baykas, and K. Qaraqe, “IEEE 802.11 bb reference channel models for indoor environments,” Tech. Rep., 2018.

[26] H. B. Eldeeb, M. Uysal, S. M. Mana, P. Hellwig, J. Hilt, and V. Jungnickel, “Channel Modelling for Light Communications: Validation of Ray Tracing by Measurements,” in *2020 12th International Symposium on Communication Systems, Networks and Digital Signal Processing (CSNDSP)*, 2020, pp. 1–6.

[27] F. Aghaei, H. B. Eldeeb, L. Bariah, S. Muhaidat, and M. Uysal, “Comparative Characterization of Indoor VLC and MMW Communications via Ray Tracing Simulations,” *IEEE Access*, vol. 11, pp. 90 345–90 357, 2023.

[28] S. Vappangi and V. M. Vakamulla, “Channel estimation in ACO-OFDM employing different transforms for VLC,” *AEU - Int. J. Electron. Commun.*, vol. 84, pp. 111 – 122, 2018.

[29] Y. Jiang, M. Safari, and H. Haas, “Joint Frame Detection and Channel Estimation for DCO-OFDM LiFi Systems,” in *Ubiquitous Networking*, E. Sabir, A. García Armada, M. Ghogho, and M. Debbah, Eds. Cham: Springer International Publishing, 2017, pp. 532–541.

[30] Y. S. Hussein and A. C. Annan, “Li-Fi technology: High data transmission securely,” in *Journal of Physics: Conference Series*, vol. 1228, no. 1. IOP Publishing, 2019, p. 012069.

[31] J. C. Estrada-Jiménez, B. G. Guzmán, M. J. Fernández-Getino García, and V. P. G. Jiménez, “Superimposed Training-Based Channel Estimation for MISO Optical-OFDM VLC,” *IEEE Transactions on Vehicular Technology*, vol. 68, no. 6, pp. 6161–6166, 2019.

[32] R. K. Kahlon, G. S. Walia, and A. Sheetal, "Channel estimation techniques in MIMO-OFDM systems–review article," *International Journal of Advanced Research in Computer and Communication Engineering*, vol. 4, no. 5, 2015.

[33] M. B. Sutar and V. S. Patil, "LS and MMSE estimation with different fading channels for OFDM system," in *2017 International conference of Electronics, Communication and Aerospace Technology (ICECA)*, vol. 1, 2017, pp. 740–745.

[34] S. R, J. T, A. B. M, and R. V, "Channel Estimation for OFDM Systems Using MMSE and LS Algorithms," in *2022 6th International Conference on Trends in Electronics and Informatics (ICOEI)*, 2022, pp. 1–5.

[35] L. Sarperi, X. Zhu, and A. K. Nandi, "Blind OFDM Receiver Based on Independent Component Analysis for Multiple-Input Multiple-Output Systems," *IEEE Transactions on Wireless Communications*, vol. 6, no. 11, pp. 4079–4089, 2007.

[36] M. Bhuyan and K. K. Sarma, "MIMO-OFDM channel tracking using a dynamic ANN topology," *International Journal of Electronics and Communication Engineering*, vol. 6, no. 11, pp. 1321–1327, 2012.

[37] Q. Hu, F. Gao, H. Zhang, S. Jin, and G. Y. Li, "Deep learning for channel estimation: Interpretation, performance, and comparison," *IEEE Transactions on Wireless Communications*, vol. 20, no. 4, pp. 2398–2412, 2020.

[38] H. Ye, G. Y. Li, and B. Juang, "Power of Deep Learning for Channel Estimation and Signal Detection in OFDM Systems," *IEEE Wirel. Commun. Lett.*, vol. 7, no. 1, pp. 114–117, Feb 2018.

[39] Y. Wang, M. Liu, J. Yang, and G. Gui, "Data-driven deep learning for automatic modulation recognition in cognitive radios," *IEEE Transactions on Vehicular Technology*, vol. 68, no. 4, pp. 4074–4077, 2019.

[40] F. Alhomayani and M. H. Mahoor, "Deep learning methods for fingerprint-based indoor positioning: A review," *Journal of Location Based Services*, vol. 14, no. 3, pp. 129–200, 2020.

[41] L. Liang, H. Ye, G. Yu, and G. Y. Li, "Deep-learning-based wireless resource allocation with application to vehicular networks," *Proceedings of the IEEE*, vol. 108, no. 2, pp. 341–356, 2019.

[42] T. Girici, C. Zhu, J. R. Agre, and A. Ephremides, "Proportional fair scheduling algorithm in OFDMA-based wireless systems with QoS constraints," *J. Commun. Netw.*, vol. 12, no. 1, pp. 30–42, 2010.

[43] R. Dong, C. She, W. Hardjawana, Y. Li, and B. Vucetic, "Deep learning for radio resource allocation with diverse quality-of-service requirements in 5G," *IEEE Transactions on Wireless Communications*, vol. 20, no. 4, pp. 2309–2324, 2020.

[44] J. Guo and C. Yang, "Predictive resource allocation with deep learning," in *2018 IEEE 88th Vehicular Technology Conference (VTC-Fall)*. IEEE, 2018, pp. 1–7.

[45] M. D. Soltani, A. A. Purwita, Z. Zeng, H. Haas, and M. Safari, "Modeling the Random Orientation of Mobile Devices: Measurement, Analysis and LiFi Use Case," *IEEE Transactions on Communications*, vol. 67, no. 3, pp. 2157–2172, 2019.

[46] V. Rodoplu, K. Hocaoğlu, A. Adar, R. O. Çikmazel, and A. Saylam, "Characterization of Line-of-Sight Link Availability in Indoor Visible Light Communication Networks Based on the Behavior of Human Users," *IEEE Access*, vol. 8, pp. 39 336–39 348, 2020.

[47] S. Tripathi, N. V. Sabu, A. K. Gupta, and H. S. Dhillon, *Millimeter-Wave and Terahertz Spectrum for 6G Wireless*. Cham: Springer International Publishing, 2021, pp. 83–121. [Online]. Available: https://doi.org/10.1007/978-3-030-72777-2_6

[48] C. Chaccour, M. N. Soorki, W. Saad, M. Bennis, and P. Popovski, "Can Terahertz Provide High-Rate Reliable Low Latency Communications for Wireless VR?" *IEEE Internet of Things Journal*, pp. 1–1, 2022.

[49] H. Abumarshoud, L. Mohjazi, O. A. Dobre, M. Di Renzo, M. A. Imran, and H. Haas, "LiFi through Reconfigurable Intelligent Surfaces: A New Frontier for 6G?" *IEEE Vehicular Technology Magazine*, vol. 17, no. 1, pp. 37–46, 2022.

[50] T. Bai, C. Pan, Y. Deng, M. Elkashlan, A. Nallanathan, and L. Hanzo, "Latency minimization for intelligent reflecting surface aided mobile edge computing," *IEEE Journal on Selected Areas in Communications*, vol. 38, no. 11, pp. 2666–2682, 2020.

[51] H. Wang, Z. Zhang, B. Zhu, J. Dang, L. Wu, L. Wang, K. Zhang, and Y. Zhang, "Performance of wireless optical communication with reconfigurable intelligent surfaces and random obstacles," *arXiv preprint arXiv:2001.05715*, 2020.

[52] Y. Cao and T. Lv, "Intelligent reflecting surface enhanced resilient design for MEC offloading over millimeter wave links," *arXiv preprint arXiv:1912.06361*, 2019.

[53] Y. Cao, T. Lv, W. Ni, and Z. Lin, "Sum-rate maximization for multi-reconfigurable intelligent surface-assisted device-to-device communications," *IEEE Transactions on Communications*, vol. 69, no. 11, pp. 7283–7296, 2021.

[54] L. Yang, J. Yang, W. Xie, M. O. Hasna, T. Tsiftsis, and M. Di Renzo, "Secrecy performance analysis of RIS-aided wireless communication systems," *IEEE Transactions on Vehicular Technology*, vol. 69, no. 10, pp. 12 296–12 300, 2020.

[55] N. A. Amran, M. Dehghani Soltani, M. Yaghoobi, and M. Safari, "Deep Learning Based Signal Detection for OFDM VLC Systems," in *2020 IEEE International Conference on Communications Workshops (ICC Workshops)*, 2020, pp. 1–6.

[56] N. A. Amran, M. D. Soltani, M. Yaghoobi, and M. Safari, "Learning Indoor Environment for Effective LiFi Communications: Signal Detection and Resource Allocation," *IEEE Access*, vol. 10, pp. 17 400–17 416, 2022.

[57] N. A. Amran, M. Dehghani Soltani, and M. Safari, "Link Blockage Analysis for Indoor Optical Wireless Communications," in *2023 IEEE Global Communications Conference (GLOBECOM): Optical Networks and Systems*, Dec. 2023.

[58] M. Garlińska, A. Pregowska, K. Masztalerz, and M. Osial, "From Mirrors to Free-Space Optical Communication-Historical Aspects in Data Transmission," *Future Internet*, vol. 10, pp. 1–17, 10 2020.

[59] A. G. Bell, "Selenium and the Photophone," *Nature*, vol. 22, no. 569, pp. 500–503, Sep. 1880.

[60] P. H. Pathak, X. Feng, P. Hu, and P. Mohapatra, "Visible Light Communication, Networking, and Sensing: A Survey, Potential and Challenges," *IEEE Communications Surveys and Tutorials*, vol. 17, no. 4, pp. 2047–2077, 2015.

[61] C. Elliott, M. Yamada, J. Penning, S. Schober, and K. Lee, "Energy savings forecast of solid-state lighting in general illumination applications," Navigant Consulting, Inc., Washington, DC (United States), Tech. Rep., 2019.

[62] B. Béchadergue and B. Azoulay, “An Industrial View on LiFi Challenges and Future,” in *2020 12th International Symposium on Communication Systems, Networks and Digital Signal Processing (CSNDSP)*, 2020, pp. 1–6.

[63] L. U. Khan, “Visible light communication: Applications, architecture, standardization and research challenges,” *Digital Communications and Networks*, vol. 3, no. 2, pp. 78–88, 2017. [Online]. Available: https://www.sciencedirect.com/science/article/pii/S2352864816300335

[64] M. Uysal, “Visible Light Communications: From Theory to Industrial Standardization,” in *2019 Optical Fiber Communications Conference and Exhibition (OFC)*, 2019, pp. 1–3.

[65] H. Burchardt, N. Serafimovski, D. Tsonev, S. Videv, and H. Haas, “VLC: Beyond point-to-point communication,” *IEEE Communications Magazine*, vol. 52, no. 7, pp. 98–105, 2014.

[66] A. M. Khalid, J. Linnartz, P. van Voorthuisen, X. Deng, and S. Mardanikorani, “Productization Experiences of G. vlc (ITU) based LiFi System for high Speed Indoor Wireless Access,” in *1st Optical Wireless Communication Conference (OWCC 2020)*, 2020.

[67] M. Dehghani Soltani, “Analysis of random orientation and user mobility in LiFi networks,” 2019.

[68] O. Alsulami, A. T. Hussein, M. T. Alresheedi, and J. M. Elmirghani, “Optical wireless communication systems, a survey,” *arXiv preprint arXiv:1812.11544*, 2018.

[69] K. H. Lee and S. R. Lee, “Process development for yellow phosphor coating on blue light emitting diodes (LEDs) for white light illumination,” in *2006 8th Electronics Packaging Technology Conference*, 2006, pp. 379–384.

[70] D. Tsonev, H. Chun, S. Rajbhandari, J. J. D. McKendry, S. Videv, E. Gu, M. Haji, S. Watson, A. E. Kelly, G. Faulkner, M. D. Dawson, H. Haas, and D. O’Brien, “A 3-Gb/s Single-LED OFDM-Based Wireless VLC Link Using a Gallium Nitride μLED,” *IEEE Photonics Technology Letters*, vol. 26, no. 7, pp. 637–640, 2014.

[71] N. Bamiedakis, X. Li, J. J. D. McKendry, E. Xie, R. Ferreira, E. Gu, M. D. Dawson, R. V. Penty, and I. H. White, “Micro-LED-based guided-wave optical links for visible light communications,” in *2015 17th International Conference on Transparent Optical Networks (ICTON)*, 2015, pp. 1–4.

[72] A. R. Anwar, M. T. Sajjad, M. A. Johar, C. A. Hernández-Gutiérrez, M. Usman, and S. Łepkowski, “Recent progress in micro-LED-based display technologies,” *Laser & Photonics Reviews*, vol. 16, no. 6, p. 2100427, 2022.

[73] J. Liu, W. Noonpakdee, H. Takano, and S. Shimamoto, “Foundational analysis of spatial optical wireless communication utilizing image sensor,” in *2011 IEEE International Conference on Imaging Systems and Techniques*, 2011, pp. 205–209.

[74] P. Djahani and J. Kahn, “Analysis of infrared wireless links employing multibeam transmitters and imaging diversity receivers,” *IEEE Transactions on Communications*, vol. 48, no. 12, pp. 2077–2088, 2000.

[75] Z. Wang, D. Tsonev, S. Videv, and H. Haas, “On the Design of a Solar-Panel Receiver for Optical Wireless Communications With Simultaneous Energy Harvesting,” *IEEE Journal on Selected Areas in Communications*, vol. 33, no. 8, pp. 1612–1623, 2015.

[76] S. Schmid, G. Corbellini, S. Mangold, and T. R. Gross, “An LED-to-LED Visible Light Communication system with software-based synchronization,” in *2012 IEEE Globecom Workshops*, 2012, pp. 1264–1268.

[77] H. Le Minh, D. O'Brien, G. Faulkner, L. Zeng, K. Lee, D. Jung, Y. Oh, and E. T. Won, "100-Mb/s NRZ Visible Light Communications Using a Postequalized White LED," *IEEE Photonics Technology Letters*, vol. 21, no. 15, pp. 1063–1065, 2009.

[78] A. M. Khalid, G. Cossu, R. Corsini, P. Choudhury, and E. Ciaramella, "1-Gb/s Transmission Over a Phosphorescent White LED by Using Rate-Adaptive Discrete Multitone Modulation," *IEEE Photonics Journal*, vol. 4, no. 5, pp. 1465–1473, 2012.

[79] H. Schulze, "Frequency-Domain Simulation of the Indoor Wireless Optical Communication Channel," *IEEE Transactions on Communications*, vol. 64, no. 6, pp. 2551–2562, 2016.

[80] C. Chen, D. A. Basnayaka, and H. Haas, "Downlink Performance of Optical Attocell Networks," *Journal of Lightwave Technology*, vol. 34, no. 1, pp. 137–156, 2016.

[81] S. Alfattani, "Review of LiFi technology and its future applications," *Journal of Optical Communications*, vol. 42, no. 1, pp. 121–132, 2021.

[82] M. S. Islim and H. Haas, "Modulation techniques for li-fi," *ZTE Commun*, vol. 14, no. 2, pp. 29–40, 2016.

[83] S. Dimitrov and H. Haas, "Optimum Signal Shaping in OFDM-Based Optical Wireless Communication Systems," in *2012 IEEE Vehicular Technology Conference (VTC Fall)*, 2012, pp. 1–5.

[84] J. Armstrong, "OFDM for Optical Communications," *Journal of Lightwave Technology*, vol. 27, no. 3, pp. 189–204, 2009.

[85] J. Armstrong and B. J. Schmidt, "Comparison of Asymmetrically Clipped Optical OFDM and DC-Biased Optical OFDM in AWGN," *IEEE Communications Letters*, vol. 12, no. 5, pp. 343–345, 2008.

[86] H. Chun, A. Gomez, C. Quintana, W. Zhang, G. Faulkner, and D. O'Brien, "A wide-area coverage 35 Gb/s visible light communications link for indoor wireless applications," *Scientific reports*, vol. 9, no. 1, p. 4952, 2019.

[87] X. Xiao, X. Tao, and J. Lu, "Energy-efficient resource allocation in LTE-based MIMO-OFDMA systems with user rate constraints," *IEEE Transactions on Vehicular Technology*, vol. 64, no. 1, pp. 185–197, 2014.

[88] M. A. Arfaoui, M. D. Soltani, I. Tavakkolnia, A. Ghrayeb, C. M. Assi, M. Safari, and H. Haas, "Measurements-Based Channel Models for Indoor LiFi Systems," *IEEE Transactions on Wireless Communications*, vol. 20, no. 2, pp. 827–842, 2021.

[89] M. Dehghani Soltani, A. A. Purwita, I. Tavakkolnia, H. Haas, and M. Safari, "Impact of Device Orientation on Error Performance of LiFi Systems," *IEEE Access*, vol. 7, pp. 41 690–41 701, 2019.

[90] Z. N. Chaleshtori, S. Zvanovec, Z. Ghassemlooy, O. Haddad, and M.-A. Khalighi, "Impact of Receiver Orientation on OLED-based Visible-Light D2D Communications," in *2021 17th International Symposium on Wireless Communication Systems (ISWCS)*, 2021, pp. 1–6.

[91] Y. S. Eroğlu, Y. Yapıcı, and I. Güvenç, "Impact of Random Receiver Orientation on Visible Light Communications Channel," *IEEE Transactions on Communications*, vol. 67, no. 2, pp. 1313–1325, 2019.

[92] F. Firyaguna, J. Kibilda, C. Galiotto, and N. Marchetti, "Performance Analysis of Indoor mmWave Networks With Ceiling-Mounted Access Points," *IEEE Transactions on Mobile Computing*, vol. 20, no. 5, pp. 1940–1950, 2021.

[93] A. Shrestha and A. Mahmood, “Review of deep learning algorithms and architectures,” *IEEE access*, vol. 7, pp. 53 040–53 065, 2019.

[94] C. Tan, F. Sun, T. Kong, W. Zhang, C. Yang, and C. Liu, “A survey on deep transfer learning,” in *Artificial Neural Networks and Machine Learning–ICANN 2018: 27th International Conference on Artificial Neural Networks, Rhodes, Greece, October 4-7, 2018, Proceedings, Part III 27*. Springer, 2018, pp. 270–279.

[95] J. Schmidhuber, “Deep learning in neural networks: An overview,” *Neural networks*, vol. 61, pp. 85–117, 2015.

[96] S. H. Haji and A. M. Abdulazeez, “Comparison of optimization techniques based on gradient descent algorithm: A review,” *PalArch’s Journal of Archaeology of Egypt/Egyptology*, vol. 18, no. 4, pp. 2715–2743, 2021.

[97] A. F. Agarap, “Deep learning using rectified linear units (relu),” *arXiv preprint arXiv:1803.08375*, 2018.

[98] V. Sze, Y.-H. Chen, T.-J. Yang, and J. S. Emer, “Efficient processing of deep neural networks: A tutorial and survey,” *Proceedings of the IEEE*, vol. 105, no. 12, pp. 2295–2329, 2017.

[99] A. Shewalkar, D. Nyavanandi, and S. A. Ludwig, “Performance evaluation of deep neural networks applied to speech recognition: RNN, LSTM and GRU,” *Journal of Artificial Intelligence and Soft Computing Research*, vol. 9, no. 4, pp. 235–245, 2019.

[100] S. Hochreiter and J. Schmidhuber, “Long Short-term Memory,” *Neural computation*, vol. 9, pp. 1735–80, 12 1997.

[101] Y. Hua, Z. Zhao, R. Li, X. Chen, Z. Liu, and H. Zhang, “Deep Learning with Long Short-Term Memory for Time Series Prediction,” *IEEE Commun. Mag.*, vol. 57, no. 6, pp. 114–119, June 2019.

[102] E. Tsironi, P. Barros, C. Weber, and S. Wermter, “An analysis of Convolutional Long Short-Term Memory Recurrent Neural Networks for gesture recognition,” *Neurocomputing*, vol. 268, pp. 76 – 86, 2017.

[103] J. Chung, C. Gulcehre, K. Cho, and Y. Bengio, “Empirical Evaluation of Gated Recurrent Neural Networks on Sequence Modeling,” 2014.

[104] D. Bahdanau, K. Cho, and Y. Bengio, “Neural Machine Translation by Jointly Learning to Align and Translate,” 2016.

[105] J. Qiao and M.-S. Alouini, “Secure Transmission for Intelligent Reflecting Surface-Assisted mmWave and Terahertz Systems,” *IEEE Wireless Communications Letters*, vol. 9, no. 10, pp. 1743–1747, 2020.

[106] M. A. Arfaoui, A. Ghrayeb, and C. Assi, “Integration of IRS in Indoor VLC Systems: Challenges, Potential and Promising Solutions,” 2021. [Online]. Available: https://arxiv.org/abs/2101.05927

[107] X. Ma, Z. Chen, W. Chen, Z. Li, Y. Chi, C. Han, and S. Li, “Joint Channel Estimation and Data Rate Maximization for Intelligent Reflecting Surface Assisted Terahertz MIMO Communication Systems,” *IEEE Access*, vol. 8, pp. 99 565–99 581, 2020.

[108] S. Sun, F. Yang, J. Song, and Z. Han, “Joint Resource Management for Intelligent Reflecting Surface–Aided Visible Light Communications,” *IEEE Transactions on Wireless Communications*, vol. 21, no. 8, pp. 6508–6522, 2022.

[109] P. G. Pachpande, M. H. Khadr, A. F. Hussein, and H. Elgala, “Visible Light Communication Using Deep Learning Techniques,” in *2018 IEEE 39th Sarnoff Symp.*, Sep. 2018, pp. 1–6.

[110] H. Lee, I. Lee, and S. Lee, “Deep learning based transceiver design for multi-colored VLC systems,” *Opt. Express*, vol. 26, p. 6222, 03 2018.

[111] O. Şayli, H. Doğan, and E. Panayirci, “On channel estimation in DC Biased optical OFDM systems over VLC channels,” in *2016 Int. Conf. Adv. Tech. Commun. (ATC)*, 2016, pp. 147–151.

[112] X. Shi, S.-H. Leung, and J. Min, “Adaptive least squares channel estimation for visible light communications based on tap detection,” *Opt. Commun.*, vol. 467, p. 125712, 2020.

[113] X. Wu, Z. Huang, and Y. Ji, “Deep neural network method for channel estimation in visible light communication,” *Opt. Commun.*, vol. 462, p. 125272, 2020.

[114] A. Özmen and H. Senol, “Channel Estimation for Realistic Indoor Optical Wireless Communication in ACO-OFDM Systems,” *Wirel. Pers. Commun.*, vol. 102, 05 2018.

[115] A. Yesilkaya, O. Karatalay, A. S. Ogrenci, and E. Panayirci, “Channel estimation for visible light communications using neural networks,” in *2016 Int. Joint Conf. Neural Netw. (IJCNN)*, 2016, pp. 320–325.

[116] M. Zhang, Y. Zeng, Z. Han, and Y. Gong, “Automatic Modulation Recognition Using Deep Learning Architectures,” in *2018 IEEE 19th Int. Workshop Signal Process. Adv. Wirel. Commun. (SPAWC)*, June 2018, pp. 1–5.

[117] Z. Zhang, Y. Zhu, W. Zhu, H. Chen, X. Hong, and J. Chen, “Iterative point-wise reinforcement learning for highly accurate indoor visible light positioning,” *Opt. Express*, vol. 27, no. 16, p. 22161, Aug 2019.

[118] Y. Wang, M. Chen, Z. Yang, W. Saad, T. luo, S. Cui, and H. V. Poor, “Meta-Reinforcement Learning for Reliable Communication in THz/VLC Wireless VR Networks,” [Online] Available: https://arxiv.org/abs/2102.12277, 2021.

[119] N. Farsad and A. J. Goldsmith, “Detection Algorithms for Communication Systems Using Deep Learning,” *CoRR*, vol. abs/1705.08044, 2017. [Online]. Available: http://arxiv.org/abs/1705.08044

[120] M. Ozturk *et al.*, “A novel deep learning driven, low-cost mobility prediction approach for 5G cellular networks: The case of the Control/Data Separation Architecture (CDSA),” *Neurocomputing*, vol. 358, pp. 479 – 489, 2019.

[121] Y. Tao, X. Liang, J. Wang, and C. Zhao, “Scheduling for indoor visible light communication based on graph theory,” *Opt. Express*, vol. 23, no. 3, pp. 2737–2752, Feb 2015.

[122] Y. Wang, X. Wu, and H. Haas, “Resource Allocation in LiFi OFDMA Systems,” in *GLOBECOM 2017 - 2017 IEEE Global Commun. Conf.*, 2017, pp. 1–6.

[123] Y. Wang, M. Chen, Z. Yang, T. Luo, and W. Saad, “Deep Learning for Optimal Deployment of UAVs With Visible Light Communications,” *IEEE Trans. Wirel. Commun.*, vol. 19, no. 11, pp. 7049–7063, 2020.

[124] S. Shrivastava, B. Chen, C. Chen, H. Wang, and M. Dai, “Deep Q-Network Learning Based Downlink Resource Allocation for Hybrid RF/VLC Systems,” *IEEE Access*, vol. 8, pp. 149 412–149 434, 2020.

[125] H. Yang *et al.*, “Learning-Based Energy-Efficient Resource Management by Heterogeneous RF/VLC for Ultra-Reliable Low-Latency Industrial IoT Networks,” *IEEE Trans. Industr. Inform.*, vol. 16, no. 8, pp. 5565–5576, 2020.

[126] M. D. Soltani, A. A. Purwita, Z. Zeng, H. Haas, and M. Safari, “Modeling the Random Orientation of Mobile Devices: Measurement, Analysis and LiFi Use Case,” *IEEE Trans. Commun.*, vol. 67, no. 3, pp. 2157–2172, March 2019.

[127] A. A. Purwita, M. D. Soltani, M. Safari, and H. Haas, “Terminal Orientation in OFDM-Based LiFi Systems,” *IEEE Trans. on Wirel. Commun.*, vol. 18, no. 8, pp. 4003–4016, 2019.

[128] P. Chen and H. Kobayashi, “Maximum likelihood channel estimation and signal detection for OFDM systems,” in *2002 IEEE Int. Conf. on Commun. Conference Proceedings. ICC 2002 (Cat. No.02CH37333)*, vol. 3, 2002, pp. 1640–1645 vol.3.

[129] H. Vikalo, B. Hassibi, and P. Stoica, “Efficient joint maximum-likelihood channel estimation and signal detection,” *IEEE Trans. on Wirel. Commun.*, vol. 5, no. 7, pp. 1838–1845, 2006.

[130] Y. S. Hussein, M. Y. Alias, and A. A. Abdulkafi, “On performance analysis of LS and MMSE for channel estimation in VLC systems,” in *2016 IEEE 12th Int. Colloq. Signal Process. Appl. (CSPA)*, 2016, pp. 204–209.

[131] F. Chang, K. Onohara, and T. Mizuochi, “Forward error correction for 100 G transport networks,” *IEEE Commun. Mag.*, vol. 48, no. 3, pp. S48–S55, 2010.

[132] J.-B. Wang, X.-X. Xie, Y. Jiao, and M. Chen, “Training sequence based frequency-domain channel estimation for indoor diffuse wireless optical communications,” *EURASIP J. Wirel. Commun. and Netw.*, vol. 2012, 10 2012.

[133] Kuenyoung Kim, Hoon Kim, and Youngnam Han, “A proportionally fair scheduling algorithm with QoS and priority in 1xEV-DO,” in *The 13th IEEE Int. Symp. Personal, Indoor and Mobile Radio Commun.*, vol. 5, 2002, pp. 2239–2243 vol.5.

[134] J. Beysens, Q. Wang, and S. Pollin, “Exploiting Blockage in VLC Networks Through User Rotations,” *IEEE Open Journal of the Communications Society*, vol. 1, pp. 1084–1099, 2020.

[135] Y. Wu, J. Kokkoniemi, C. Han, and M. Juntti, “Interference and Coverage Analysis for Terahertz Networks With Indoor Blockage Effects and Line-of-Sight Access Point Association,” *IEEE Transactions on Wireless Communications*, vol. 20, no. 3, pp. 1472–1486, 2021.

[136] I. Abdalla, M. B. Rahaim, and T. D. C. Little, “Interference Mitigation Through User Association and Receiver Field of View Optimization in a Multi-User Indoor Hybrid RF/VLC Illuminance-Constrained Network,” *IEEE Access*, vol. 8, pp. 228 779–228 797, 2020.

[137] J. Beysens, Q. Wang, and S. Pollin, “Improving Blockage Robustness in VLC Networks,” in *2019 11th International Conference on Communication Systems Networks (COMSNETS)*, 2019, pp. 164–171.

[138] C. Chen and H. Haas, “Performance Evaluation of Downlink Cooperative Multipoint Joint Transmission in LiFi Systems,” in *2017 IEEE Globecom Workshops (GC Wkshps)*, 2017, pp. 1–6.

[139] C. Chen, D. A. Basnayaka, A. A. Purwita, X. Wu, and H. Haas, “Wireless Infrared-Based LiFi Uplink Transmission With Link Blockage and Random Device Orientation,” *IEEE Transactions on Communications*, vol. 69, no. 2, pp. 1175–1188, 2021.

[140] A. Singh, G. Ghatak, A. Srivastava, V. A. Bohara, and A. K. Jagadeesan, “Performance Analysis of Indoor Communication System Using Off-the-Shelf LEDs With Human Blockages,” *IEEE Open Journal of the Communications Society*, vol. 2, pp. 187–198, 2021.

[141] A. Singh, A. Srivastava, and V. A. Bohara, “Optimum LED semiangle and the receiver FOV selection for Indoor VLC System with Human Blockages,” in *2022 IEEE 95th Vehicular Technology Conference: (VTC2022-Spring)*, 2022, pp. 1–7.

[142] S. Sun, F. Yang, and J. Song, “Sum Rate Maximization for Intelligent Reflecting Surface-Aided Visible Light Communications,” *IEEE Communications Letters*, vol. 25, no. 11, pp. 3619–3623, 2021.

[143] B. Cao, M. Chen, Z. Yang, M. Zhang, J. Zhao, and M. Chen, “Reflecting the Light: Energy Efficient Visible Light Communication with Reconfigurable Intelligent Surface,” in *2020 IEEE 92nd Vehicular Technology Conference (VTC2020-Fall)*, 2020, pp. 1–5.

[144] L. Qian, X. Chi, L. Zhao, and A. Chaaban, “Secure visible light communications via intelligent reflecting surfaces,” in *ICC 2021-IEEE International Conference on Communications*. IEEE, 2021, pp. 1–6.

[145] S. Aboagye, T. M. N. Ngatched, O. A. Dobre, and A. R. Ndjiongue, “Intelligent Reflecting Surface-Aided Indoor Visible Light Communication Systems,” *IEEE Communications Letters*, vol. 25, no. 12, pp. 3913–3917, 2021.

[146] Z. Yang, M. Chen, W. Saad, W. Xu, M. Shikh-Bahaei, H. V. Poor, and S. Cui, “Energy-efficient wireless communications with distributed reconfigurable intelligent surfaces,” *IEEE Transactions on Wireless Communications*, vol. 21, no. 1, pp. 665–679, 2021.

[147] Y. Liu, X. Liu, X. Mu, T. Hou, J. Xu, M. Di Renzo, and N. Al-Dhahir, “Reconfigurable intelligent surfaces: Principles and opportunities,” *IEEE communications surveys & tutorials*, vol. 23, no. 3, pp. 1546–1577, 2021.

[148] J. Zhang, J. Liu, S. Ma, C.-K. Wen, and S. Jin, “Large system achievable rate analysis of RIS-assisted MIMO wireless communication with statistical CSIT,” *IEEE Transactions on Wireless Communications*, vol. 20, no. 9, pp. 5572–5585, 2021.

[149] L. You, J. Xiong, D. W. K. Ng, C. Yuen, W. Wang, and X. Gao, “Energy efficiency and spectral efficiency tradeoff in RIS-aided multiuser MIMO uplink transmission,” *IEEE Transactions on Signal Processing*, vol. 69, pp. 1407–1421, 2020.

[150] H. Chongwen, G. Alexandropoulos, C. Yuen, and m. Debbah, “Indoor Signal Focusing with Deep Learning Designed Reconfigurable Intelligent Surfaces,” 07 2019, pp. 1–5.

[151] Q. Wu and R. Zhang, “Beamforming Optimization for Intelligent Reflecting Surface with Discrete Phase Shifts,” in *ICASSP 2019 - 2019 IEEE International Conference on Acoustics, Speech and Signal Processing (ICASSP)*, 2019, pp. 7830–7833.

[152] C. You, B. Zheng, W. Mei, and R. Zhang, “How to Deploy Intelligent Reflecting Surfaces in Wireless Network: BS-Side, User-Side, or Both Sides?” *Journal of Communications and Information Networks*, vol. 7, no. 1, pp. 1–10, 2022.

[153] E. Björnson, Ö. Özdogan, and E. G. Larsson, “Reconfigurable intelligent surfaces: Three myths and two critical questions,” *CoRR*, vol. abs/2006.03377, 2020. [Online]. Available: https://arxiv.org/abs/2006.03377

[154] S. Aboagye, T. M. Ngatched, O. A. Dobre, and A. R. Ndjiongue, “Intelligent reflecting surface-aided indoor visible light communication systems,” *IEEE Communications Letters*, vol. 25, no. 12, pp. 3913–3917, 2021.

[155] S. Niknam, B. Natarajan, and R. Barazideh, “Interference Analysis for Finite-Area 5G mmWave Networks Considering Blockage Effect,” *IEEE Access*, vol. 6, pp. 23 470–23 479, 2018.

[156] T. Bai and R. W. Heath, “Analysis of self-body blocking effects in millimeter wave cellular networks,” in *2014 48th Asilomar Conference on Signals, Systems and Computers*, 2014, pp. 1921–1925.

[157] D. Ke, X. Liao, and S. Zhu, "Link blockage analysis for indoor 60ghz radio systems," *Electronics Letters*, vol. 48, pp. 1506–1508, 2012.

[158] T. Tang, T. Shang, and Q. Li, "Impact of Multiple Shadows on Visible Light Communication Channel," *IEEE Communications Letters*, vol. 25, no. 2, pp. 513–517, 2021.

[159] M. M. Céspedes, B. G. Guzmán, and V. P. G. Jiménez, "Lights and Shadows: A Comprehensive Survey on Cooperative and Precoding Schemes to Overcome LOS Blockage and Interference in Indoor VLC," *Sensors*, vol. 21, no. 3, 2021. [Online]. Available: https://www.mdpi.com/1424-8220/21/3/861

[160] H. Abumarshoud, B. Selim, M. Tatipamula, and H. Haas, "Intelligent Reflecting Surfaces for Enhanced NOMA-based Visible Light Communications," *CoRR*, vol. abs/2111.04646, 2021. [Online]. Available: https://arxiv.org/abs/2111.04646

[161] X. Wu and H. Haas, "Access point assignment in hybrid LiFi and WiFi networks in consideration of LiFi channel blockage," in *2017 IEEE 18th International Workshop on Signal Processing Advances in Wireless Communications (SPAWC)*, 2017, pp. 1–5.

[162] X. Wu, C. Chen, and H. Haas, "Mobility Management for Hybrid LiFi and WiFi Networks in the Presence of Light-Path Blockage," in *2018 IEEE 88th Vehicular Technology Conference (VTC-Fall)*, 2018, pp. 1–5.

[163] M. D. Soltani *et al.*, "Bidirectional Optical Spatial Modulation for Mobile Users: Toward a Practical Design for LiFi Systems," *IEEE Journal on Selected Areas in Communications*, vol. 37, no. 9, pp. 2069–2086, 2019.

[164] S. Aboagye, T. M. N. Ngatched, O. A. Dobre, and A. G. Armada, "Energy Efficient Subchannel and Power Allocation in Cooperative VLC Systems," *IEEE Communications Letters*, vol. 25, no. 6, pp. 1935–1939, 2021.

[165] C. Chen, D. Tsonev, and H. Haas, "Joint transmission in indoor visible light communication downlink cellular networks," in *2013 IEEE Globecom Workshops (GC Wkshps)*, 2013, pp. 1127–1132.

[166] V. Dixit and A. Kumar, "Performance Analysis of Indoor Visible Light Communication System with Angle Diversity Transmitter," in *2020 IEEE 4th Conference on Information and Communication Technology (CICT)*, 2020, pp. 1–5.

[167] Z. Chen, D. A. Basnayaka, and H. Haas, "Space Division Multiple Access for Optical Attocell Network Using Angle Diversity Transmitters," *Journal of Lightwave Technology*, vol. 35, no. 11, pp. 2118–2131, 2017.

[168] O. Z. Aletri, M. T. Alresheedi, and J. M. H. Elmirghani, "Transmitter Diversity with Beam Steering," in *2019 21st International Conference on Transparent Optical Networks (ICTON)*, 2019, pp. 1–5.

[169] L. Yin, X. Wu, and H. Haas, "Indoor Visible Light Positioning with Angle Diversity Transmitter," in *2015 IEEE 82nd Vehicular Technology Conference (VTC2015-Fall)*, 2015, pp. 1–5.

[170] Z. Zeng, M. D. Soltani, M. Safari, and H. Haas, "Angle Diversity Receiver in LiFi Cellular Networks," in *ICC 2019 - 2019 IEEE International Conference on Communications (ICC)*, 2019, pp. 1–6.